A STUDY OF ENGINEERING THE CATHODE STRUCTURES FOR IMPROVED PERFORMANCE IN LITHIUM BATTERIES

A Dissertation

Presented to the Faculty of the Graduate School

of Cornell University

in Partial Fulfillment of the Requirements for the Degree of

Doctor of Philosophy

by

Jangwoo Kim

May 2017

A STUDY OF ENGINEERING THE CATHODE STRUCTURES FOR IMPROVED PERFORMANCE IN LITHIUM BATTERIES

Jangwoo Kim, Ph. D.

Cornell University 2017

Lithium batteries are receiving a worldwide attention for applications such as electric vehicles, renewable energy grids for their extraordinarily high energy density. Despite high energy density of lithium-air or lithium-sulfur batteries, there are still a number of technical difficulties that need to be overcome to compete with the state-of-art lithium-ion batteries. Challenges can be narrowed down to the following; poor rechargeability at high areal capacity (> 1mAh/cm^2), low areal power density, low energy efficiency, and lithium dendrite formation intimidating both capacity retention and fire safety. The poor electrochemical performance in lithium-air battery is attributed to: 1. diffusion limitation of oxygen, 2. proportions of non-oxygen gases in air, 3. insulating discharge reaction products, 4. parasitic reactions caused by superoxide radical attacks which lead to electrolyte decomposition and carbon surface oxidation, and finally, 5. structural disorder in cathode during the cell operation cycles. Lithium-sulfur battery has its own problems of: 1. intermediate polysulfide dissolution, and 2. structural disorder in cathode due to the volumetric expansion of lithiated sulfur molecules. In this study, we demonstrate that the change

in the physical configuration of carbon-based cathode substrates in both lithium-air and lithium-sulfur battery cathodes can offer an effective approach to resolve their major issue of poor rechargeability., and. elucidate the mechanisms that alleviate the rapid loss of capacities over cycles.

BIOGRAPHICAL SKETCH

Jangwoo Kim joined Joo Group at Cornell University in October, 2012 after receiving his B.S. degree in Chemical Engineering at Yonsei University in South Korea. Before he joined Cornell University, he also worked in the Advanced Automotive Battery Division at LG Chem., which provided him a great exposure to the field of rechargeable batteries. Since he started his Ph.D. degree in Cornell University, Jangwoo Kim has been investigating the interplay between cathode structure and cell performance in both rechargeable lithium-air and lithium-sulfur batteries. Lithium-air or lithium-sulfur batteries have recaptured worldwide interest because of the increasing demand for advanced battery technology for vehicle applications and because we have found no other alternative technology with higher potential to replace the state-of-art lithium-ion batteries. The major challenges for the practically-viable rechargeable lithium-air or lithium-sulfur battery include low energy efficiency due to high overpotential and the difficulty of achieving an optimal balance between the discharge capacity and the capacity retention. Jangwoo Kim has been addressing these problems focusing on the structural instability of the lithium-air and lithium-sulfur battery cathodes in this PhD thesis.

ACKNOWLEDGMENTS

I express my sincere gratitude to my advisor, Professor Yong Lak Joo for the continuous support of my Ph.D. study and related research, for his patience, knowledge, and motivation. His guidance helped me in all the time of research and writing of this dissertation. I would like to thank the rest of my special committee members: Professor Lynden Archer and Professor Jin Suntivich, for their insightful comments and encouragement, but also for the hard question, which inspired me to widen my research from various perspectives. I acknowledge Cornell Center for Materials Research (CCMR) and the Nanobiotechnology Center (NBTC) for Shared Research Facilities, and Axium Nano, Dongjin Semichem., EMD Performance Materials Corp., STX Corp. for funding my projects. My sincere thanks also go to Dr. Jun Yin, who designed the initial model for lithium-air battery cell and provided me an opportunity to work on the related projects, and to my lab mates, Dr. Brian Williams, Dr. Soshana Smith, Dr. Ling Fei, Joseph Carlin, Andrew Shah, Rachel Villamayor, George Shebert, and Shubham Pinge who went through all the struggles and discussions with me on an everyday basis and for all the fun we have had in the last four and a half years. Without their precious support it would have not been possible to conduct this research. Last but not the least, I would like to thank my family: my parents and to my sister, and my lover for supporting me spiritually throughout my Ph.D. study and my life in general.

TABLE OF CONTENTS

LIST OF FIGURES

LIST OF ABBREVIATIONS

AC	Activated Carbons
BJH	Barret Joyner Halendar
BET	Brunauer Emmett Teller
CFP	Capillary Flow Porometer
CNF	carbon nanofibers
CNT	Carbon Nanotubes
CV	Cyclic Voltammetry
DIB	Diisopropenylbenzene
DME	Dimethoxyethane
DMA	Dimethylacetamide
DMF	Dimethylformamide
DMSO	Dimethylsulfoxide
DOL	Dioxolane
EV	Electric Vehicles
EIS	Electrochemical Impedance Spectroscopy
EDS	Energy Dispersive X-ray Spectroscopy
FE-SEM	Field Emission Scanning Electron Microscope
F-CNF	Freestanding carbon nanofiber
GDL	Gas Diffusion Layer
GNR	Graphene Nanoribbons
GONR	Graphene Oxide Nanoribbons
GS	Graphene Sheets
IUPAC	International Union of Pure and Applied Chemistry

KB	Ketjen Black
LiTFSI	Lithium Bis(trifluoromethylsulphonyl)imide
Li_2CO_3	Lithium Carbonates
LiI	Lithium Iodide
$LiNO_3$	Lithium Nitrate
Li_2O_2	Lithium Peroxides
Li_2S	Lithium Sulfide
$LiCF_3SO_3$	Lithium Trifluoromethanesulfonate, Lithium Ttriflate, LiTf
OER	Oxygen Evolution Reaction
ORR	Oxygen Reduction Reaction
PEO	Poly (Ethylene Oxide)
PAN	Polyacrylonitrile
PTFE	Polytetrafluoroethylene
RGO	Reduced Graphene Oxide
SEI	Solid Electrolyte Interface
TSA	Temperature Swing Adsorption
TSR	Thermal Swing Restacking
TMS	Thermo Mechanical Stabilization
TEM	Transmission Electron Microscopy
XPS	X-ray Photoelectron Spectroscopy

INTRODUCTION

Lithium-air and lithium-sulfur batteries have been known as the next candidate for energy storage applications such as extended-range electric vehicles, renewable energy grids for their exceptionally high theoretical specific energy and energy density much greater than those of conventional lithium-ion batteries. [1-5]

Lithium-air batteries, as described in its name, use the oxidation of lithium at anode and reduction of oxygen at cathode, creating reaction products namely lithium peroxides (Li_2O_2), originated from the net electrochemical reaction, $2(Li^+ + e^-) + O_2 \leftrightarrow Li_2O_2$ (U_0 = 2.96 V versus Li/Li^+) [4-6] along the three phase interface of the cathode substrate, where gaseous oxygen, liquid electrolyte, and solid carbon encounter. [7] Due to the intrinsic property of its reaction site, the discharge process does not always utilize the entire carbon surface especially when it comes to a high loading of active carbon materials. [8] Other major challenges in current lithium-air battery technology can be narrowed down to the following; i) poor rechargeability, ii) low areal power density, iii) low energy efficiency and iv) the safety associated with dendritic growth on the lithium-metal anode. None of the challenges listed is trivial and scientists are working in depth trying to find solutions within the next few decades. Liu, *et al.* [9] proposed a system with reduced graphene oxide (RGO) as cathode material and lithium iodide (LiI) and water as electrolyte additives that runs over 100 cycles with 8,000 mAh/g of discharge specific capacity at a current density of 1 A/g. However, when you convert the limited capacity to an industrial unit, it becomes less than 0.2 mAh/cm^2 operating at 0.02 mA/cm^2 which is far lower than that of the

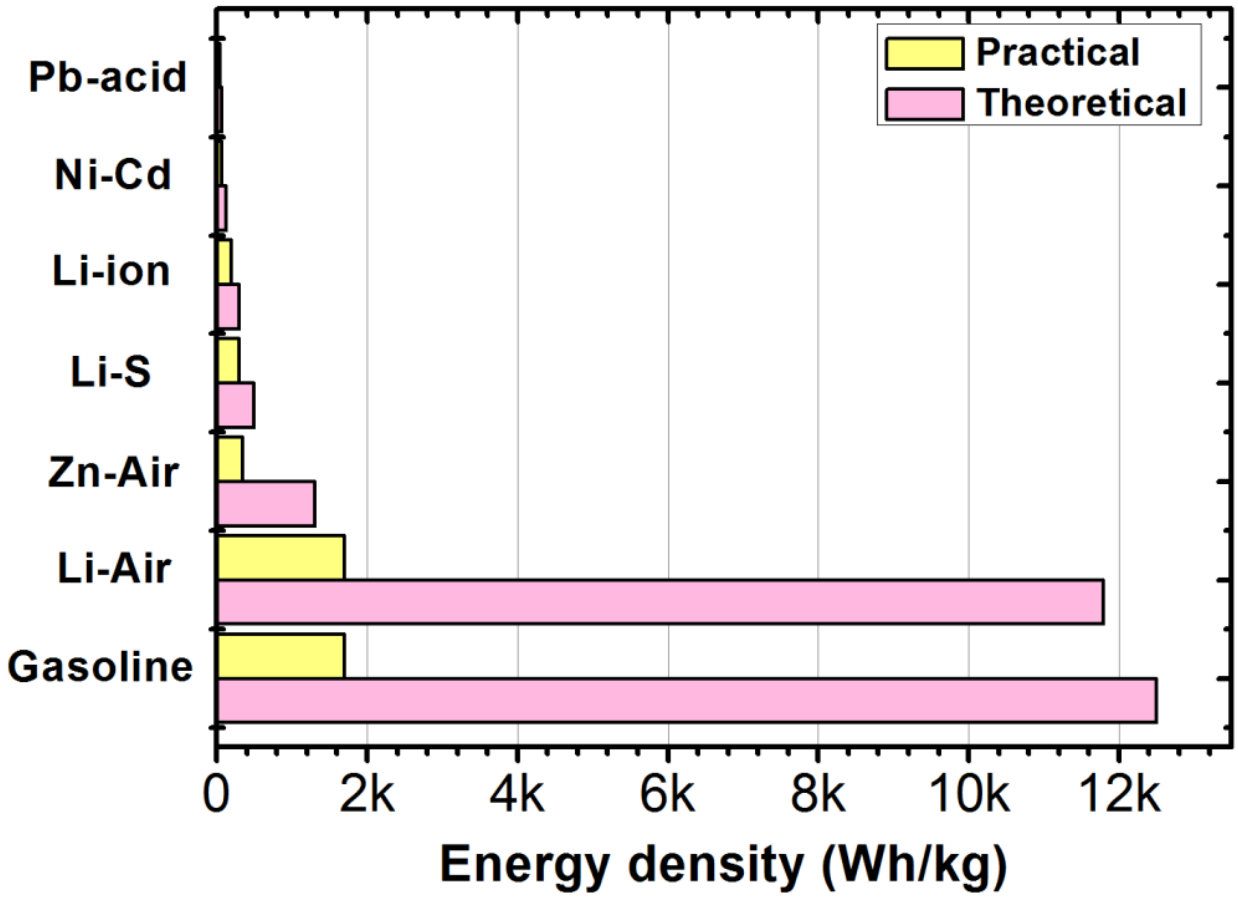

Figure 0-1. Energy density versus various battery systems including lithium-air and lithium-sulfur batteries

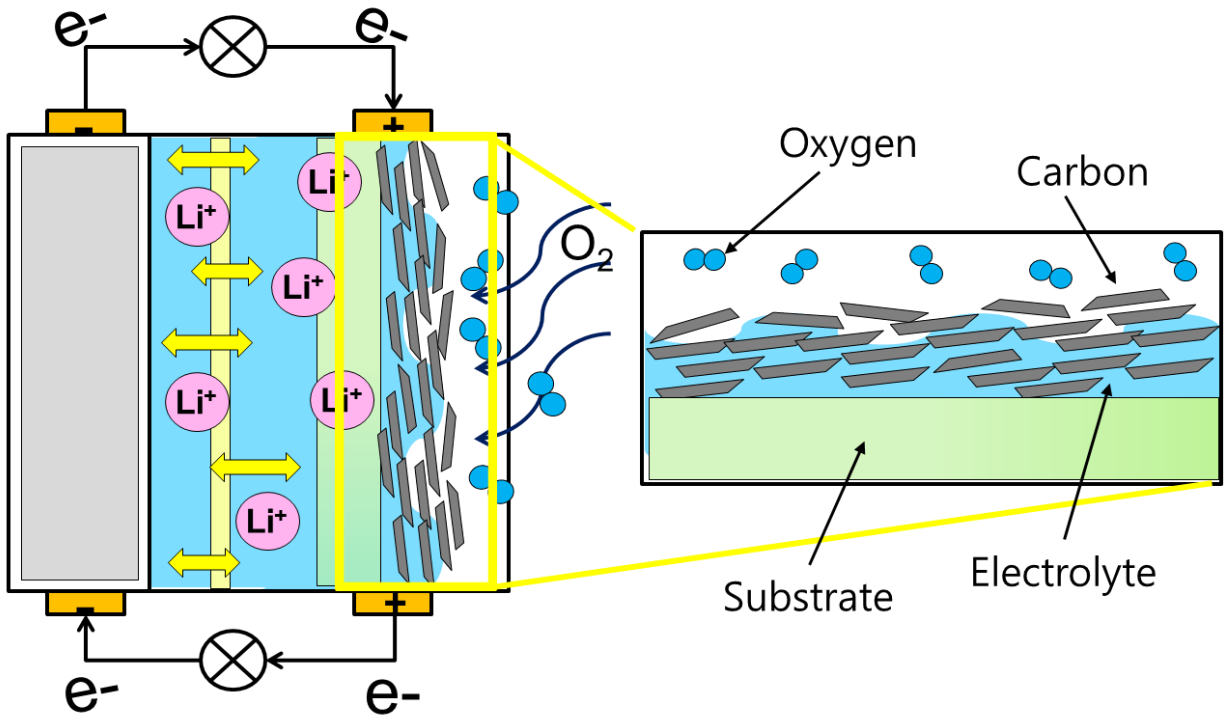

- **Discharge:**

$2Li^+ + 2e^- + 2O_2 \rightarrow 2LiO_2$

$2LiO_2 \rightarrow Li_2O_2 + O_2$,

$LiO_2 + Li^+ + e^- \rightarrow Li_2O_2$

- **Charge:**

$2\ Li^+ + 2e^- + O_2 \leftarrow Li_2O_2$

Figure 0-2. Schematic illustration of a lithium-air battery and its principles

conventional lithium-ion batteries. (~ 1.5 mAh/cm^2). Xiao, *et al.* [10] on the other hand, worked on the highly loaded cathode system, and achieved 13 mAh/cm^2 with 15 mg/cm^2 loading of carbon at a current density of 0.05 mA/cm^2. However, they were not able to demonstrate any of the cycle performance data with such high areal capacity. Walker, *et al.* [11] found a unique combination of electrolyte solvent (dimethylacetamide, DMA) and salt (lithium nitrate, $LiNO_3$) and applied it to lithium-air system, and achieved over 80 cycles with 1 mAh/cm^2 at 0.1 mA/cm^2. This result from Liox Power, Inc. is by far showing the best performance in the industrial units, and yet, it is far below what the industry requires.

Many compounded phenomena which include i) diffusion limitation with respect to oxygen, [12-15] ii) presence of non-oxygen gases (H_2O, CO_2, N_2) in the air, [16-18] iii) insulating discharge reaction products (Li_2O_2, Li_2O), [16-18] iv) parasitic reaction byproducts caused by superoxide radical attacks which lead to electrolyte decomposition and carbon surface oxidation, [22-28], and v) instability of solid electrolyte interface (SEI) of lithium metal anode and its growth of dendrites [29-34] are known to be responsible for the low cycle life of lithium-air batteries. Even though the surest way to resolve this issue of poor rechargeability is to prevent the undesirable products from forming from the beginning, only a few attempts succeeded to limit or delay the formation, and no one hitherto has found a way to completely eliminate the possibility of their emergence, while conducting a number of discharge-charge cycles. Interestingly, due to the seemingly unavoidable cell degradation, an attempt to revive the cell by washing away the remaining byproducts on the carbon surface of the air cathode by sulfuric acid was reported. [35] However, the cycle performance of the acid-treated cell was reduced to almost one half of that of the initial cell and the risk of having acids contaminating the active surface area should be considered along with environmental and safety aspects. Changing the chemistry of electrolyte is

another way to resolve so that it could withstand the consequence of superoxide radical attacks and avoid the parasitic reactions from electrolyte decomposition. [36-38] Lightweight, highly conductive, highly porous cathode materials such as carbon nanotubes (CNT), [39-41] graphene sheets (GS), [12, 42-44] graphene nanoribbons (GNR), [45-47] activated carbons (AC), [48-50] carbon nanofibers (CNF) [51-54] are also being used to study the effects on the performance to work out the shortfalls. Moreover, studies on the effect of the amount of cathode materials [55, 56] and water as an additive [9, 22, 57] have been reported to find a way to expand the system threshold that keeps the lithium-air batteries from its theoretical specific energy. However, only a few discussed the structural characteristics of lithium-air battery cathodes and the effect of the amount of carbon loadings using different types of carbon at the same time. [58]

Our study in the first part of this paper addresses new findings that the accumulation and subsequent removal of reaction products during discharge-charge cycles in lithium-air batteries can lead to a significant change in the physical configuration of the cathode structure especially when the carbon substrate is fully utilized, and demonstrates that rearranging the active carbon materials and realigning the three phase interface of the used cathodes via mild heat treatment results in the enhanced cycle performance and reduces the discharge overpotential at the same time. We present a new way of renewing the used cathodes, not by eliminating the unavoidable reaction products, but by restoring the carbon structure altered during discharge-charge cycles to its original state via mild heat treatment. Once the cathodes are used and become ineffective, we bring them back to life by rearranging the carbon structure and refilling the carbon pores with additional amount of electrolyte regardless of the presence of the remaining reaction products. This so-called thermal swing restacking (TSR) process enables the complete utilization of carbon surface in the air cathode and brings substantial improvements on the cycle performance of

lithium-air batteries. Confirmed by the experimental and simulation results, the hindrance to the rechargeability was not only due to the insulating and irreversible reaction products but also to the significant structural damage to the carbon structure from discharge-charge cycles. The results stress the importance of maintaining the physical structure of lithium-air battery cathode during the cell operation, and provide a new insight towards pulling out capacity retention of the system by better utilization of the available carbon surface in the air cathode.

The system selection for carbon source and carbon loading for air cathodes is being rigorously discussed sincethese factors significantly affect the diffusion process of oxygen and determine the practical capacity of the lithium-air batteries which is still distant from its theoretical capacity. Layered cathodes fabricated by successively stacking two different carbons selected among the pairs of RGO-CNT, RGO-GNR, or RGO-graphene oxide nanoribbons (GONR) are introduced in the second part of this thesis. Out of all carbon materials, they were chosen as pairs because the two different carbons possess two distinct morphologies enabling the immiscible stacking in layered structures. The structural variance of the cathodes controlled by different carbons with different morphologies demonstrated a clear synergic effect in terms of improving the overall electrochemical performance of lithium-air batteries. With a constant amount of total active carbon materials, but with a different number of layers, the layered cathodes demonstrated a significant increase in specific capacity and decrease in overpotential. Moreover, regardless of the amount of carbon loading, the sandwich-stacked cathodes produced the highest value of all capacities in comparison with single layer or a simple mix-type cathodes, and the humid environment led to the higher specific capacities in the open air system. This study using different number of alternating graphene layers introduces a way of controlling the macropore

structure of cathodes, and therefore, facilitating the diffusion process of oxygen, and suggests a promising and facile strategy in designing oxygen diffusion pathways of cathodes.

Freestanding carbon nanofiber (F-CNF) fabricated by electrospinning polyacrylonitrile (PAN) dissolved in dimethylformamide (DMF), followed by carbonization was used and characterized as a lithium-air battery cathode in the third part of this paper. F-CNF cathode was chosen for its superior porosity from what we have learned in the previous studies accommodating the volume expansion and structural damage during cycling that we have discovered in part one and facilitating the diffusion process of oxygen that we demonstrated in part two. Moreover, no polymeric binder is used in fabricating F-CNF cathode, which enhances the interconnectivity for electron transport pathways. Four F-CNF samples with different average fiber diameters and different average interfiber distances were spun by using different electrospinning parameters such as applied voltage or polymer concentration, and were chosen for comparison in terms of full discharge specific capacity and oxygen reduction reaction (ORR) kinetics. Although the results were commensurate with our numerical analysis, four samples presented very similar capacity retention over a number of discharge-charge cycles. Controlling the structural parameter such as average pore size or specific surface area by changing the electrospinning condition was confirmed to be less conducive in enhancing the cycle life, while directly related to the change in gravimetric specific discharge capacities. On the other hand, the thermo-mechanical stabilization of F-CNF fabrication process and higher ramping rate of the pre-oxidizing temperature have caused the fusion of fibers and shown that the continuous cycle of accumulation and removal of the reaction products did not affect or alter the cathode structure and demonstrated significant improvement in the capacity retention. This method of fabrication brings a significant synergistic

effect when combined with sandwich stacking of other types of carbon additives such as Super P or RGO, serving as a promising solution of the lithium-air battery cathode and performs the best of all presented in this study in terms of capacity retention presented in this paper.

Meanwhile, lithium-sulfur battery has exceptionally high theoretical specific capacity of 1,675 mAh/g and the low cost and abundance of sulfur are attracting various people in the industry. [59-62] The chemistry in the lithium-sulfur battery brings each sulfur atom to host two lithium ions to form lithium sulfide (Li_2S) whereas conventional lithium-ion batteries accommodate only 0.5 lithium ions per carbon atom. The discharge reaction follows a sequence of following: $S_8 \rightarrow Li_2S_8 \rightarrow Li_2S_6 \rightarrow Li_2S_4 \rightarrow Li_2S_3 \rightarrow Li_2S$, and the reverse of it during charge. [63-65] Sulfur has conductivity of 5×10^{-30} S/cm at 25 ℃, which requires a carbon coating to provide an effective electron pathway and structural stability. [66-68] A few but critical obstacles still left to overcome to find a breakthrough in the industry, such as rapid capacity loss due to intermediate polysulfide (Li_2S_8, Li_2S_6, Li_2S_4, Li_2S_3) dissolution into liquid electrolyte [69-79] and volume expansion of sulfur during lithiation process (nearly 80% of the original volume of sulfur). [80-88] The intermediate polysulfides formed during discharge lithiation process dissolve and react to form insoluble lithium sulfides on the surface of lithium metal at the anode during charge, and this so-called shuttle effect slowly removes the active sulfur in the cathode and causes rapid degradation of the cell. Moreover, the volume expansion of sulfur gives stress on the cathode and reduces the contact between the carbon coating and the sulfur and hinders the diffusion of lithium ions on the carbon surface. The uses of many different types of protective layers on the lithium metal anode are reported to alleviate the cell degradation by preventing the reaction and precipitation of the intermediate polysulfides on the surface of the anode. [89-93] Seh, *et al.* [82]

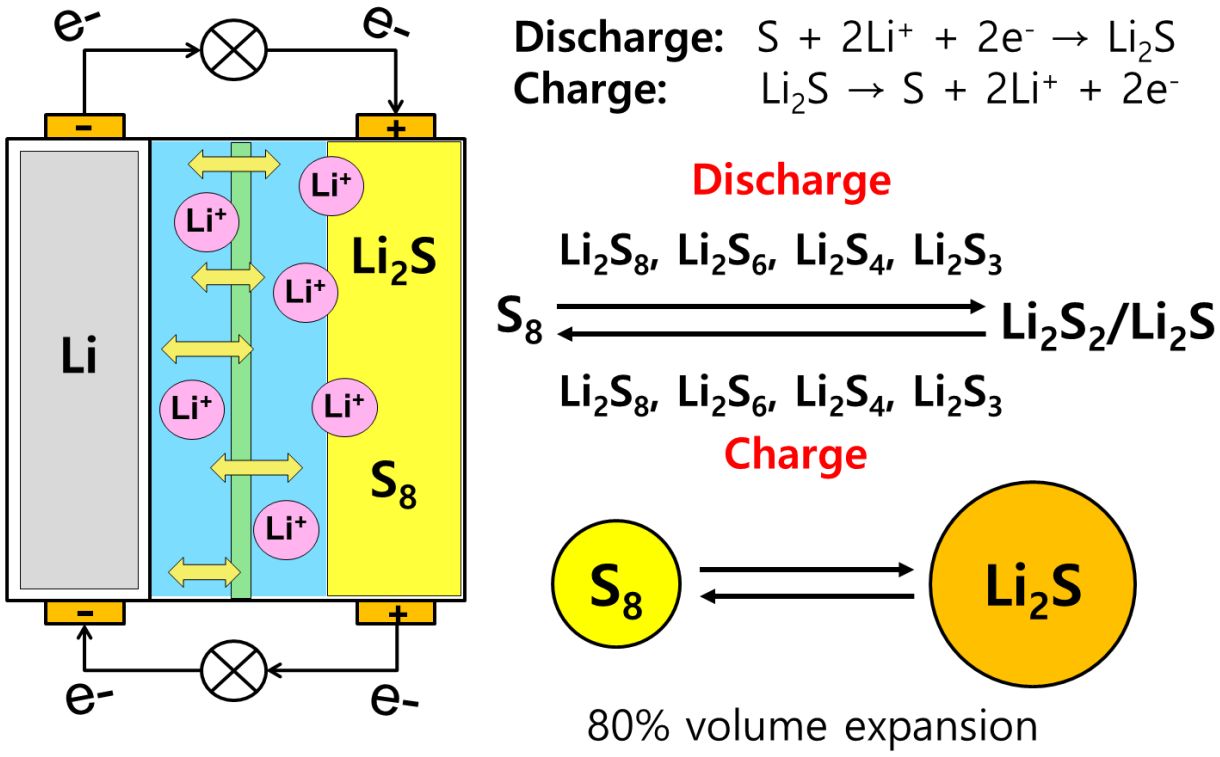

Figure 0-3. Schematic illustration of a lithium-sulfur battery and its working principles

invented and proposed sulfur-TiO_2 yolk-shell type nanoparticles with internal void spaces to mitigate the effect of volume expansion of sulfur and to minimize the dissolution of intermediate polysulfides and applied successfully to lithium-sulfur battery cathodes with significant improvement in the capacity retention. However, the use of heavy weight ceramic instead of carbon lowers the specific gravimetric capacity and the process of nanoparticle synthesis is not trivial to reduce the cost of materials as compared to conventional lithium-ion batteries. Interestingly, Xin, *et al.* [94] implies that the cyclic octatomic molecules of sulfur will not be able to completely avoid its loss within the cathode structure and will cause the rapid fading of capacity. They show and claim that the metastable small sulfur molecules of S_{2-4} instead of S_8 completely avoid the unfavorable transition to soluble intermediate polysulfides. The synthesis of smaller sulfur molecules requires the stress of confinement within conductive carbon matrix. Here, in the last part of this study, we propose a facile fabrication of nanostructured cathode using electrospun sulfur-containing copolymer, poly(sulfur-random-(1,3-diisopropenylbenzene)) or poly(S-r-DIB), nanofiber with interfiber void space to accommodate the volume expansion of lithiated sulfur. The unique stretched-out chain structure of sulfur copolymer converted from the original cyclic octatomic sulfur molecules and confined within the polymer matrix is proven to be conducive to minimizing the polysulfide dissolution, [95] which results in the improvement of the capacity retention over cycles. Due to the ductile and sticky nature of poly(S-r-DIB), this cathode system offers a direct deposit of sulfur/conductive carbon materials on the current collector which can potentially be used in a flexible Li-S battery system.

Overall, it is hypothesized in this study that the change in the physical configuration of lithium-air or lithium-sulfur battery cathodes brings a new approach to resolve the major issue of poor

rechargeability. All parts of this study aim to investigate the physical configuration of cathodes and it is expected for readers to see how far we can improve the electrochemical performance by controlling the physical structural parameters of the cathode.

CHAPTER I

LiTHIUM-AIR BATTERY CATHODE STRUCTURE: THERMAL RESTACKING

INTRODUCTION

Lithium-air batteries or lithium-oxygen batteries apply the oxidation of lithium and reduction of oxygen on the three phase interface of the cathode substrate, where gaseous oxygen, liquid electrolyte, and solid carbon encounter. [4-7] Because the reaction products only accumulate on the three phase interface the usage of the carbon surface is innately limited largely proportional to the amount of carbon loading in the cathode system. [8] Poor rechargeability of lithium-air batteries is reportedly attributed to the diffusion limitation with respect to oxygen, [12-15] insulating nature of reaction products (Li_2O_2, Li_2O), [16-18] parasitic byproducts caused by electrolyte and carbon surface oxidation [16-18] and the presence of non-oxygen gases (H_2O, CO_2, N_2) in the air. [22-28] Changing the chemistry of electrolyte is one way to resolve the issue of the low cycle life. [36-38] Utilizing lightweight, highly conductive, highly porous cathode materials is another way to work out the physical limitations. [39-54] Adding water in the electrolyte [9, 22, 57] may have shown a breakthrough to expand the system threshold that keeps the lithium-air batteries from its theoretical specific energy. However, no one hitherto studied in depth on the structural characteristics of the air cathode and its effect on the improvement of the cycle performance.

Here, we demonstrate that rearranging the carbon materials and realigning the three phase interface of the used cathodes via mild heat treatment and electrolyte replacement enhance the cycle performance of the lithium-air batteries and address our findings that the accumulation and subsequent removal of reaction products can lead to a significant change in the cathode structure. We present a way of repairing the used cathodes, not by eliminating the unavoidable byproducts, [35] but by restoring the carbon structure having altered during discharge and charge process to its pristine state via heat treatment. Once the cathodes are used and become ineffective, we bring them back to life by rearranging the carbon structure and refilling the carbon pores with additional amount of electrolyte regardless of the presence of the remaining reaction products. This so-called thermal swing restacking (TSR) process enables the complete utilization of carbon surface in the air cathode and brings substantial improvements on the cycle performance of lithium-air batteries. Confirmed by the experimental and simulation results, the hindrance to the rechargeability was not only due to the insulating and irreversible reaction products but also to the significant structural damage to the carbon structure from discharge-charge cycles. The results stress the importance of maintaining the physical structure of lithium-air battery cathode during the cell operation, and provide a new insight towards pulling out capacity retention of the system by better utilization of the available carbon surface in the air cathode.

EXPERIMENTAL METHODS

i) CATHODE FABRICATION

Pure lithium metal foil was purchased from MTI Corporation and was used as an anode. Anhydrous DME and $LiCF_3SO_3$ salts were procured from Sigma-Aldrich, purified extensively by molecular sieve, and kept in an argon filled glove box (< 0.1 ppm. O_2 and H_2O). The electrolyte, 1 M $LiCF_3SO_3$ in DME, was prepared in the glove box and was impregnated into the glass fiber separator (GF/D, Whatman) which was dried under vacuum at 100 ℃ for 24 hours before use. The RGO was kindly donated by Dongjin Semichem Corporation. The slurry solution was made by dispersing, in isopropyl alcohol (Sigma-Aldrich), the RGO used as an active material and Nafion perfluorinated resin (Ion Power, Inc.) as a binder in a weight ratio of 80:20 and was subsequently casted onto a carbon paper substrate (Toray, TGP-H-030). The fabricated cathodes were dried overnight at 95 ℃ in a drying oven and transferred to the glove box for cell assembly. The amount of RGO loaded on the carbon paper substrate is 0.1 ± 0.02 mg/cm^2. In the case of ultrahigh loading cathode, the active material, CNF is made by carbonizing electrospun PAN nanofiber mats at 900 ℃ for 3 hours. The amount of CNF loaded per each cathode is 7.0 ± 0.5 mg/cm^2, and the thickness of this CNF cathode is 0.012 ± 0.003 cm.

ii) LITHIUM-AIR CELL ASSEMBLY

The cell assembly begins with placing 15 mm diameter and 0.25 mm thick lithium disc foil on top of the stainless steel disc. A dried glass fiber was then placed on top of the lithium foil. The electrolyte solution (330 µl) was injected into the glass fiber followed by immediately placing a pristine RGO cathode and a stainless steel mesh which works as a current collector. A Teflon tube with O-rings centering on both sides was then placed surrounding all the cell components

sideways followed by placing a load string connected to the other half of the stainless steel disc. All of the assembly process was done in the argon filled glove box. (< 0.1 ppm. O_2 and H_2O) The chamber was then taken out from the glove box and purged with ultrahigh purity oxygen gas for 5 min to replace the argon gas inside the chamber.

iii) ELECTROCHEMICAL METHODS

The EIS of the cell was evaluated using a PARSTAT 4000 electrochemical workstation (Princeton Applied Research) within a frequency range of 10^5 to 10^{-2} Hz using 5 mV (RMS) input voltage amplitude. The galvanostatic tests of the Li-O_2 cells were performed under a cut-off voltage window from 2.0 V to 4.8 V versus Li/Li+ in the voltage limit profile by using BST8-MA (MTI Corporation) multi-channel battery testing system. The discharge-charge performance was controlled by Neware BTS system and evaluated at a constant current density of 1 A/g for the voltage limit profiles and 500 mA/g for capacity limit profiles (1,000 mAh/g). All tests were carried out under the oxygen pressure of 1 atm. The observed capacity and applied current densities were normalized by the weight of the RGO.

iv) THERMAL RESTACKING PROCESS

The lithium-air battery chamber was disassembled in the argon filled glove box after running a number of cycles. The used cathode and the stainless steel current collector were taken out from the chamber, and the remaining parts (glass fiber separator, lithium foil anode) were sealed back inside immediately. The time of the remaining parts being exposed to the outside atmosphere is less than 5 sec. The used cathode was then heated at 120 ℃ for 1 hour under argon atmosphere in an effort to eliminate the entire electrolyte solvent remaining inside the porous cathode. After cooling down the cathode for another hour, the chamber was re-opened and added with

additional 110 µl of the electrolyte to the used glass fiber separator followed by placing the thermally rearranged cathode and current collector.

v) INSTRUMENTATION

The morphologies of the RGO coated air cathode at each different state were observed by FE-SEM equipped with EDS (Tescan Mira3). The cathodes were taken out in the argon filled glove box, stored and carried in a vial wrapped with a parafilm to prevent the air flowing inside and were transferred to the SEM anti-chamber which was then evacuated immediately. Water contact angle measurements were performed on a contact angle goniometer (Rame-Hart 500) with automated dispensing system which can be controlled by the computer. One drop of water requires an amount of 100 µl. The surface property of the air cathodes was further investigated by XPS spectroscopy (Surface Science Instruments, SSX-100) and Raman scattering spectroscopy (Renishaw InVia Confocal Raman microscope). The XPS operating pressure was ~ 2×10^{-9} Torr, and monochromatic Al K-alpha X-rays (1486.6 eV) were used with beam diameter of 1mm. Photoelectrons were collected at a 55 degree emission angle. A hemispherical analyzer determined electron kinetic energy, using pass energy of 150 V for wide/survey scans, and 50 V for high resolution scans. The Raman spectrum was collected with the probe light from a nearly polarized 488 nm laser, and the focused light spot was ~1 µm in diameter. N_2 isotherms and pore size distribution were obtained from a Micromeritics Gemini VII 2390 surface area analyzer. Specific surface areas were calculated by BET method. Pore volumes and areas were estimated from the adsorption isotherms using the BJH method. Pore size distribution in large scale was measured by the capillary flow porometer (CFP-1100-AEHXL, Porous Materials, Inc.). Silwick with surface tension of 20.1 dynes/cm was chosen as the wetting liquid.

RESULTS AND DISCUSSION

i) THERMAL RESTACKING OF RGO SYSTEM

The first deep specific discharge capacity of the lithium-air cell using RGO coated carbon paper substrate as the air cathode was over 30,000 mAh/g at a current density of 1 A/g. The exceptionally high specific capacity is not only due to the use of RGO with high electrical conductivity (> 1 S/cm) and high specific pore surface area (> 500 m^2/g) but also to the high oxygen solubility and diffusivity of the 1, 2-dimethoxyethane (DME) electrolyte and extended catalytic activity of RGO with oxygenated functional groups on the surface. The defects and functional groups on the RGO produce more electrochemically irreversible compounds such as lithium carbonates (Li_2CO_3) [96, 97] but also favour the formation of reversible lithium peroxides (Li_2O_2) [12] in a way that they do not aggregate but spread around the proximity of those defective sites. The C: O ratio of RGO used as an active material measured from X-ray photoelectron spectroscopy (XPS) was 8:1. In spite of the exceptionally high discharge capacity in the first cycle, the capacity in the next cycle was reduced to one fourth, and the third cycle capacity was almost one tenth of the first cycle.

Surprisingly, by heat treating the used RGO cathode after 3rd discharge-charge cycle at 120 ℃ for 1 hour under the argon atmosphere and putting it back into the system with the same lithium anode and separator that were used in the previous cycles and with additional amount of fresh electrolyte on top of the separator, the specific capacity increased in the next cycle from 3,800 mAh/g to 21,000 mAh/g. (Figure 1-1 and Figure 1-2a) Applying this TSR scheme after each discharge-charge cycle, the specific capacity remained at around 20,000 mAh/g up to the 3rd cycle (Figure 1-2b). When operating the cell with limited capacity at 1,000 mAh/g, 101 cycles

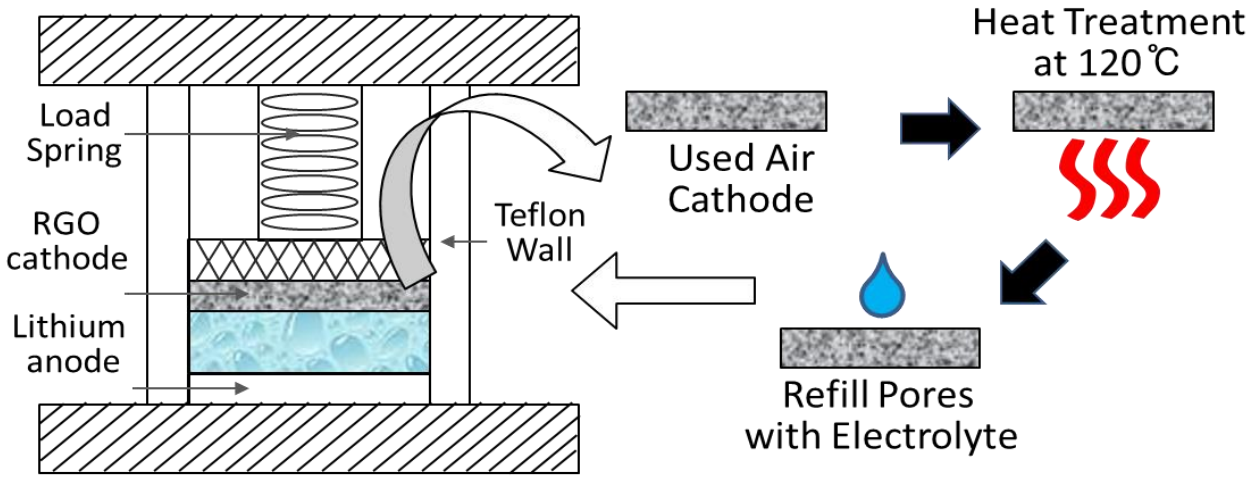

Figure 1-1. Schematic illustration of TSR process

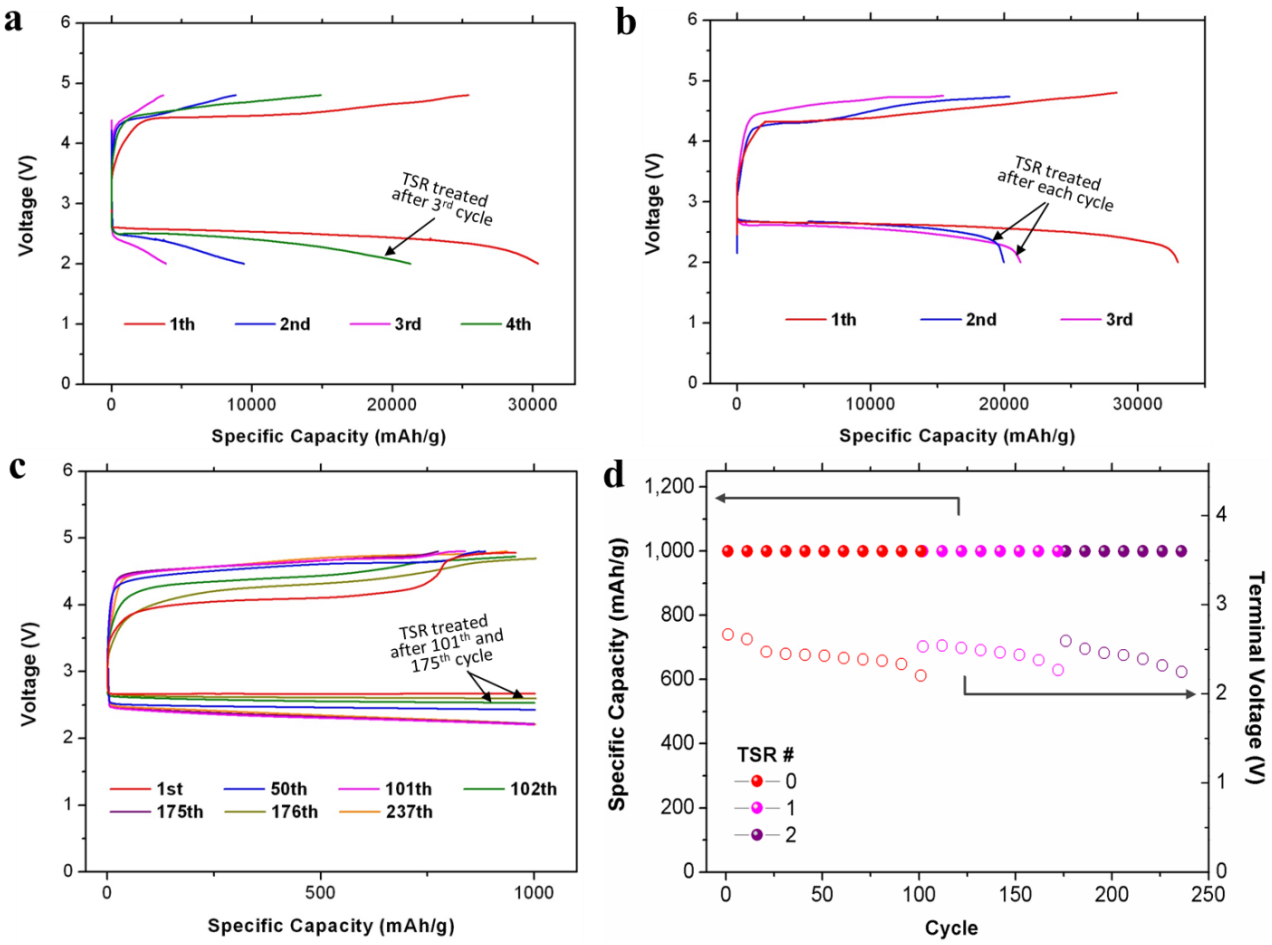

Figure 1-2. Cycle performance profiles with limited voltage range (2.0 V ~ 4.8 V) at a current density of 1,000 mA/g, where (a) the air cathode was thermally rearranged after the 3rd discharge-charge cycle, and (b) after each cycle. (c) Capacity limit profile at 1,000 mAh/g and at a current density of 500 mA/g, where the air cathode was thermally rearranged after the 101st and 175th cycle. (d) Variation of specific capacity and terminal voltage at discharge of each cycle.

were gained originally, and 136 cycles were added after the process of TSR (74 cycles after the 1st TSR, and 62 cycles after the 2nd TSR), achieving a total of 237 stable cycles. (Figure 1-2c and 1-2d) It is approximately 230% improvement of the cycle performance compared with the one without using TSR. Moreover, discharge overpotential was reduced from 0.76 V at 101st cycle to 0.43 V at 102th cycle after the 1st TSR and then again from 0.75 V at 175th cycle to 0.37 V at 176th cycle after the 2nd TSR. This result clearly indicates that the charge-transfer resistance in the lithium-air battery cell was lowered by the change made during the process of TSR. As for the next step, having fresh electrolyte added without any heat treatment was tested to see the only effect of additional electrolyte taking part in the enhancement of the cycling results as the original electrolyte might have been severely decomposed during cycles. However, as shown in Figure 1-3 plotting a profile with adding the same amount of fresh electrolyte after each cycle without any heat treatment, it was concluded that adding fresh electrolyte was not the key to the significant improvement of the cell performance. By adding fresh electrolyte we indeed observed the increase in the discharge specific capacity in the 2nd and 3rd cycle. However, the amount of increase is far less as compared with the cell with heat treatment after each cycle. (Figure 1-2b) We believe that the key lies in synergistic effect of heat treatment and fresh electrolyte applied to the used cathode in the respective order. All these cycle performance results with TSR indicate that even with the presence of reaction products left on the surface of RGO there was much more breathing space for reaction than what was expected previously. Moreover, a cathode with an ultrahigh carbon loading (~7.0 mg/cm^2) was also tested with and without the process of TSR. (Figure 1-4) The volumetric energy densities of the cell normalized by the volume of the cathodes at a current density of 0.3 mA/cm^2 show significant drops in the following cycles, whereas those with applying the process of TSR after each cycle remained over 1,500 Wh/L for

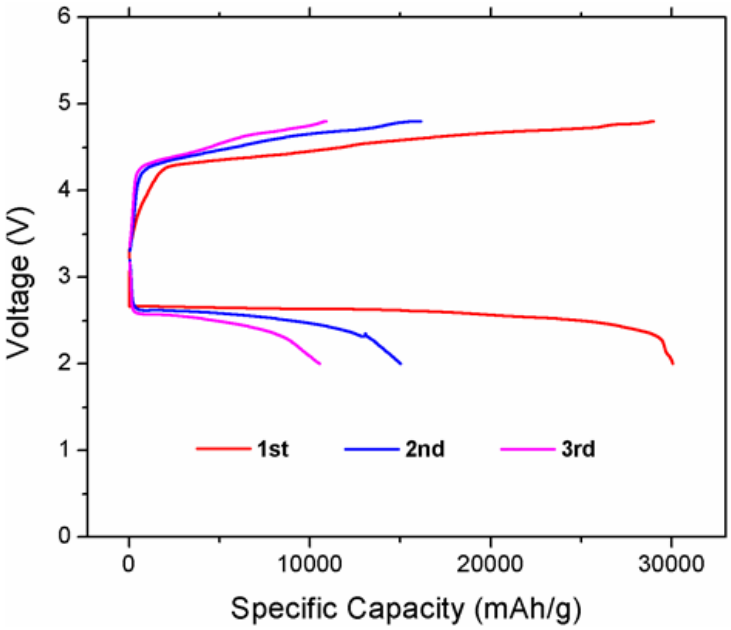

Figure 1-3. Voltage limit profile of lithium-air battery using RGO cathode and DME electrolyte, where fresh electrolyte was added after each discharge-charge cycle without any heat treatment

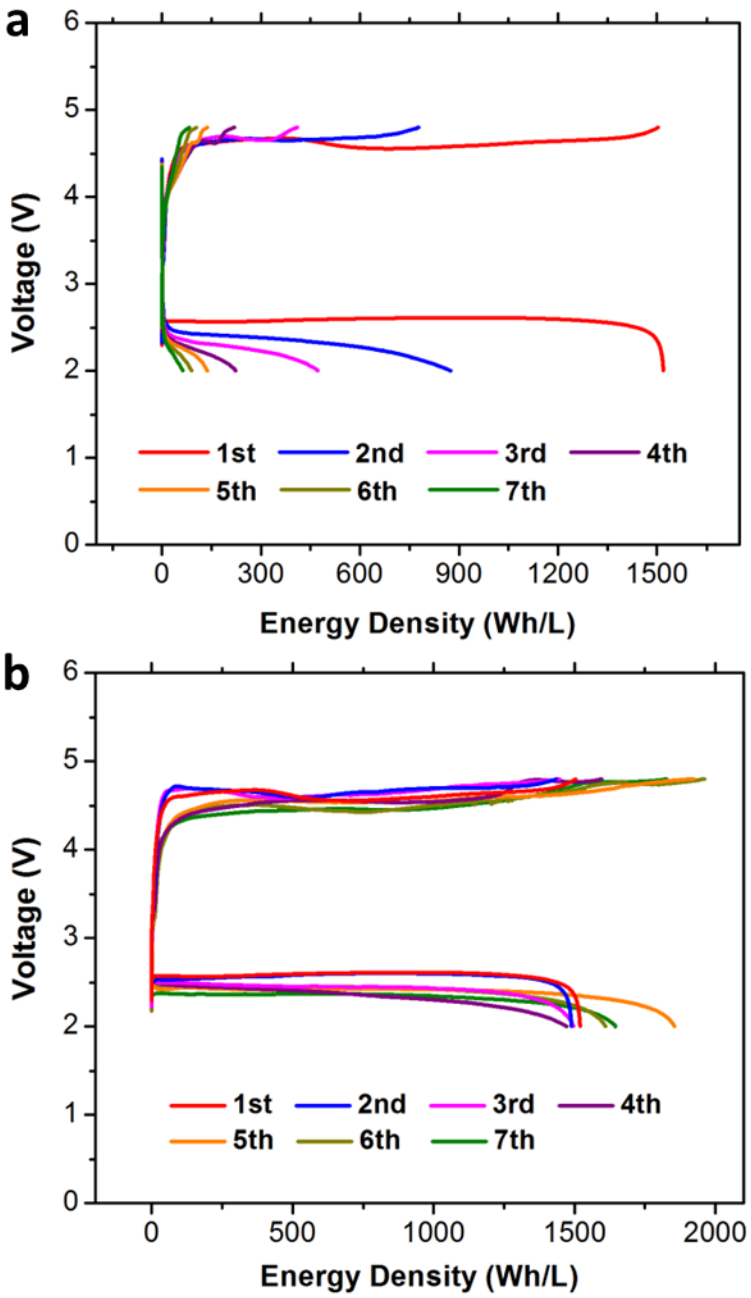

Figure 1-4. Voltage versus volumetric energy density profiles for highly-loaded CNF cathodes (a) without and (b) with the process of TSR after each cycle. The amount of carbon loading is ~7.0 mg/cm^2.

up to 7 cycles. This result demonstrates the possibility that a lithium-air cell can be fully and deeply discharged to a point of energy density that is at least 3 times as large as that of the conventional lithium-ion batteries for a number of cycles without a capacity loss.

ii) EFFECT OF THERMAL RESTACKING ON ELECTROCHEMICAL PROPERTIES

In support of the evidence of the lowered cell resistance shown in the previous section, the electrochemical impedance spectroscopy (EIS) data were obtained on the developed lithium-air cells at the pristine, discharged, charged, and thermally rearranged states as shown in Figure 1-5. All cell tests for this study were performed within a cut off voltage range from 2.0 V to 4.8 V versus Li/Li+. The width of the depressed semicircle followed by a straight line in the tail region of the Nyquist plots corresponds to the charge-transfer resistance and overall charge-transfer kinetics of the cell. The greater width of the semicircle indicates the higher charge-transfer resistance, and therefore the slower charge-transfer kinetics. It is noteworthy that the cells with the pristine cathode before discharge and thermally rearranged cathode after charge present very similar semicircle at high frequency. Even with the remaining reaction products in the pores of the active carbon material, the polarization resistance of the cell with thermally rearranged cathodes stayed almost the same as that of the pristine cell. The changes made during the process of TSR substantially recovered the charge-transfer kinetics and suppressed its resistance, leading to the enhancement of the ORR.

Raman microscope and XPS spectroscopy explicitly identified the reaction products formed on the air cathode during cell operation. (Figure 1-6) Both spectra results were commensurate with each other in that two major compounds, Li_2O_2 and Li_2CO_3 were produced and were partially decomposed during the charge. The peaks for Li_2O_2 and Li_2CO_3 appeared at 55.6 eV and 56.5 eV,

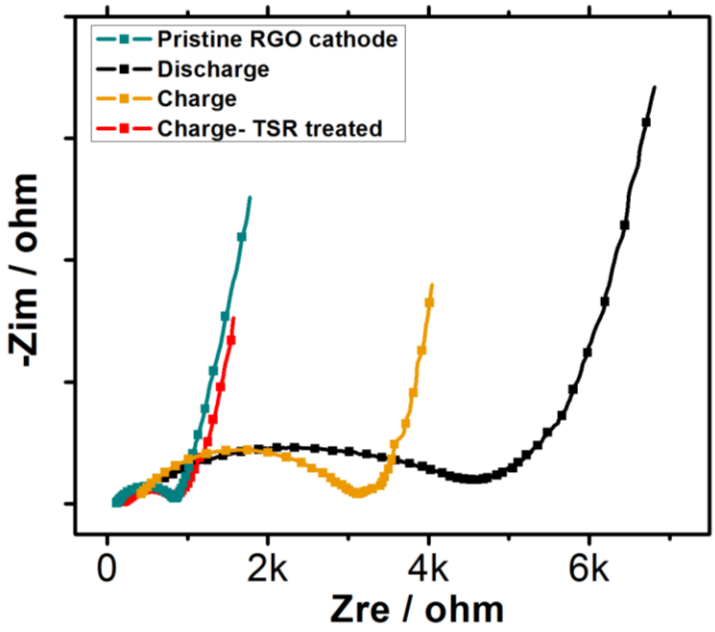

Figure 1-5. Nyquist plots of the lithium-air battery cells using DME electrolyte at the pristine, discharged, charged, and thermally rearranged (after charge) states.

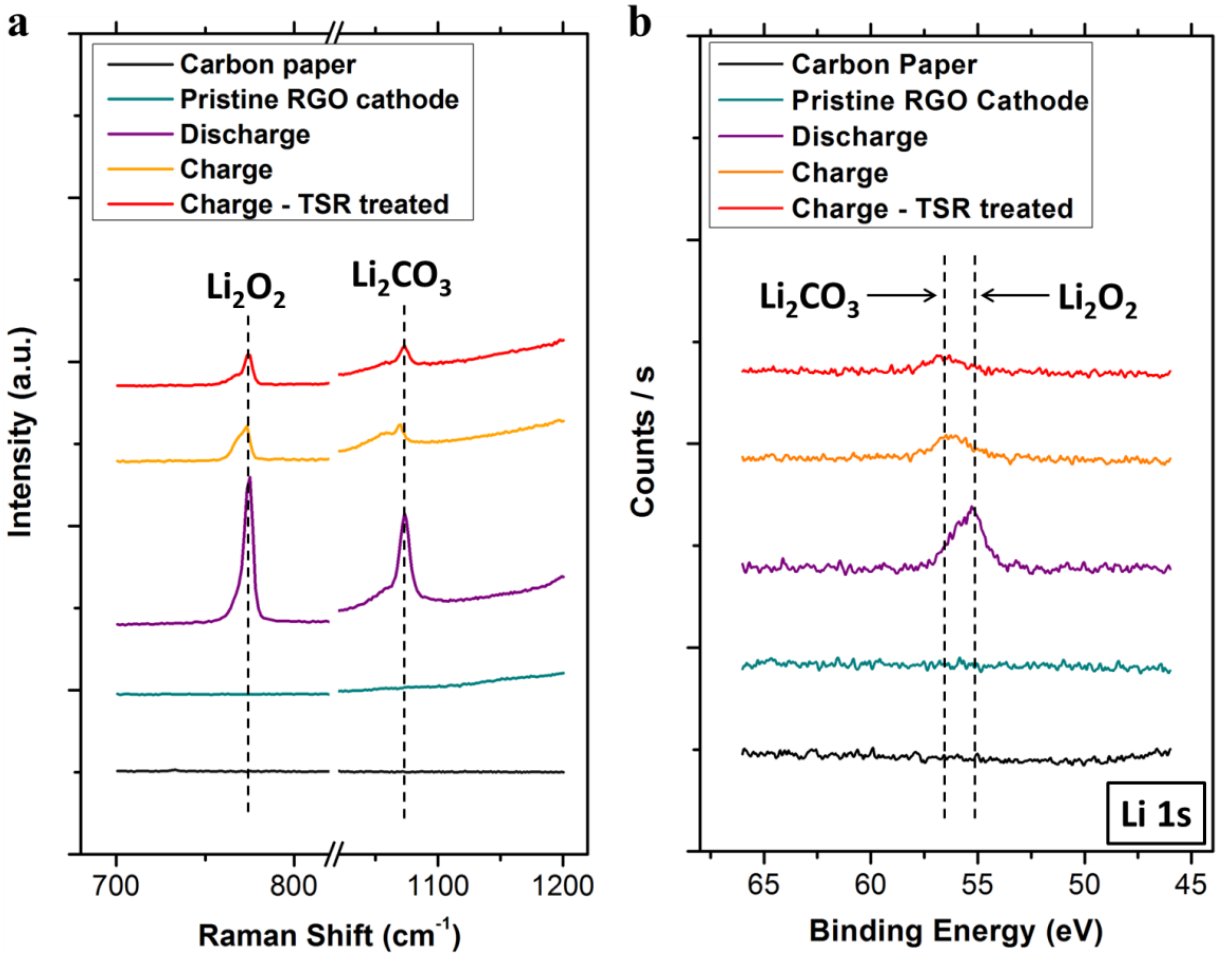

Figure 1-6. Spectra results of (a) Raman microscope (b) Li 1s XPS of the carbon paper before RGO coating and the RGO coated air cathode at the pristine, fully discharged, fully charged, and thermally rearranged (after charge) states.

respectively for the Li 1s XPS spectra and at 780 cm^{-1} and 1078 cm^{-1} for the Raman spectra. The percent decrease of the spectra intensities for the Li_2O_2 peaks between discharged and charged states of the air cathode was greater than that of the Li_2CO_3 peaks. Although the selected electrolyte, DME, is known for its stability during discharge, [98-100] the formation of the Li_2CO_3 associated with the surface defects and oxygenated functional groups of RGO were unavoidable. The spectra results of the charged cathode before and after the thermal rearrangement appear to be very similar to one another indicating that the process of TSR barely affected the state of the reaction products either qualitatively or quantitatively. Although the normalized intensities for both Li_2O_2 and Li_2CO_3 peaks slightly diminished after the heat treatment, this little change does not clearly explain the cause of significant improvement in the cycle performance.

Top view field emission scanning electron microscope (FE-SEM) images in Figure 1-7c and 1-7d show that there is no sign of notable changes in the morphology of reaction products covered on the RGO coated air cathodes before and after the heat treatment. However, the cross-sectional FE-SEM images in Figure 1-7g and 1-7h show a significant change in the cathode structure. While thermally removing the residual electrolyte solvent, the sizable crevices between carbon paper substrate and RGO layer generated during charge were closed up again and revealed no clear vacancies. Energy-dispersive X-ray spectroscopy (EDS) oxygen concentration elemental mapping images in Figure 1-7 also show that the RGO layers were merged into a single layer. These results suggest that the improved interconnectivity among RGO particles and reorganized pore structure by heat treatment recovered the charge transfer kinetics, leading to the higher energy densities at successive cycles. Water contact angle measurements in the inset images of Figure 1-7 indicate that the presence of the discharge reaction products remarkably altered the

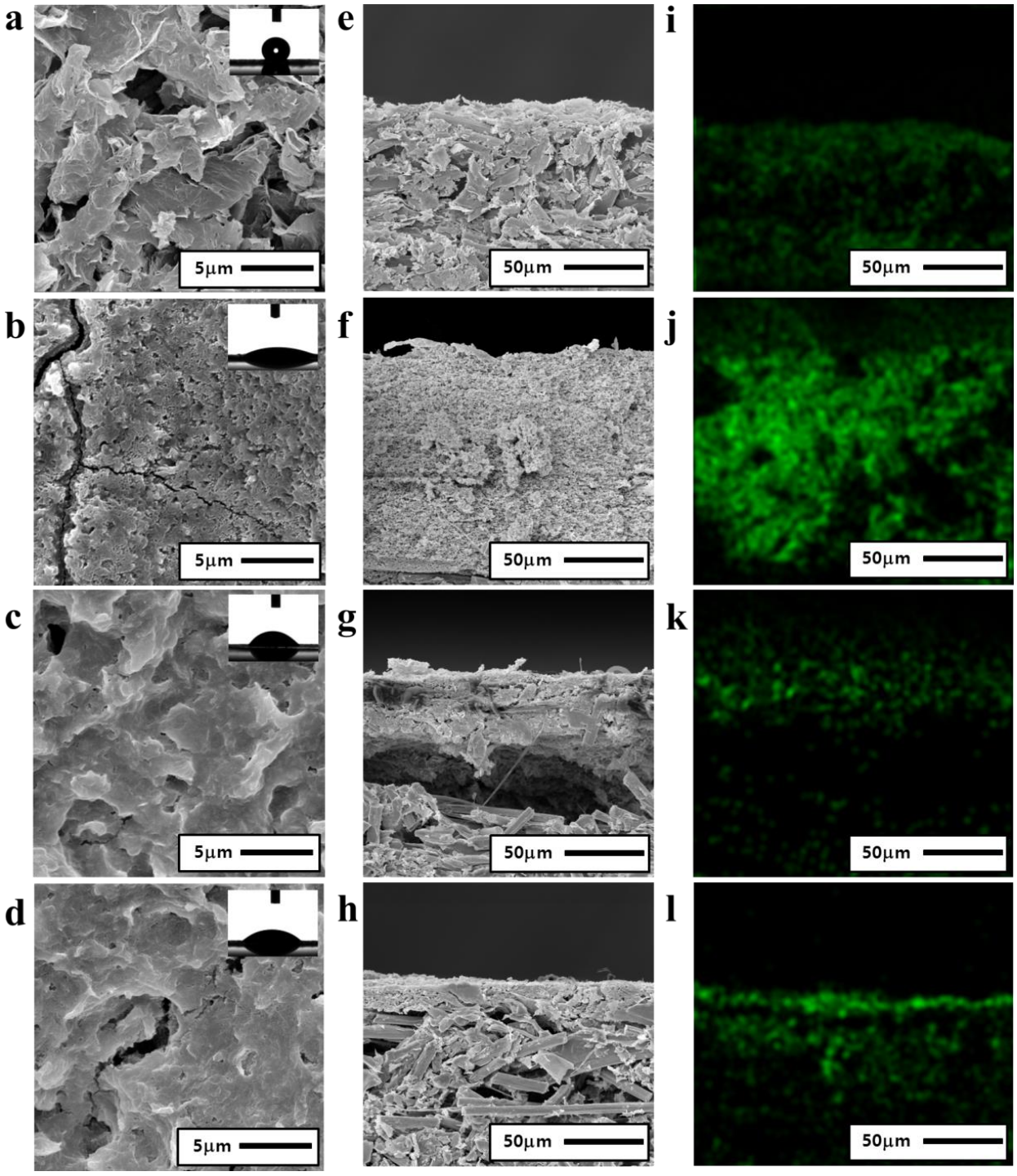

Figure 1-7. FE-SEM images of the RGO coated air cathode at the (a,e) pristine, (b,f) discharged, (c,g) charged, and (d,h) thermally rearranged (after charge) states. (e-h) are cross-sectional images of the same electrodes as in (a-d), respectively. (i-l) are EDS oxygen concentration elemental mapping images of (e-h). Inset images in (a-d) are of the water contact angle measurements for each case. (a) 134.16˚, (b) 28.68˚, (c) 51.88˚, (d) 45.76˚.

surface property of the air cathode. The water contact angles of the air cathode at the pristine, discharged, charged, and thermally rearranged states were 134.16˚, 28.68˚, 51.88˚, and 45.76˚, respectively. To our knowledge, no one in the field of lithium-air batteries has pointed out the significant change in the surface property due to the formation of the reaction products. The reaction products (Li_2O_2, Li_2CO_3) are classified as oxide minerals and possess a strong polarity. The larger the amount of the reaction products, the more hydrophilic the surface of the air cathode becomes. The slight decrease in the water contact angle between the charged cathodes before and after the heat treatment is presumably due to the evaporation of the residual electrolyte. N_2 adsorption-desorption isotherms, Barret Joyner Halendar (BJH), Brunauer Emmett Teller (BET) surface area analysis, and capillary flow porometry data further provides information on the pore size distribution of cathodes before and after the heat treatment. N_2 adsorption-desorption isotherms of the RGO cathodes before and after TSR in Figure 1-8a shows a type II curve in the overall range, a normal form of isotherm obtained with macroporous adsorbents according to the International Union of Pure and Applied Chemistry (IUPAC) classification. [101] The presence of macropores is attributed to the use of carbon paper, whereas a significant fraction of the mesopores in RGO is blocked after a discharge-charge cycle. BJH pore size distribution calculated from adsorption branch of the N_2 isotherms for cathodes before and after TSR in inset profile of Figure 1-8a exhibits a sizable change in pores in the range of 2 to 50 nanometer scales.

The pores of cathodes after TSR in the range of 15 to 50 nanometer in diameter are smaller in pore volume than those before TSR. According to the spectra analysis, the amount of reaction products on the surface of air cathodes before and after TSR hardly changed, which indicates that the reduced pore volume in meso-scale pore size is due to the change in the RGO structure rather

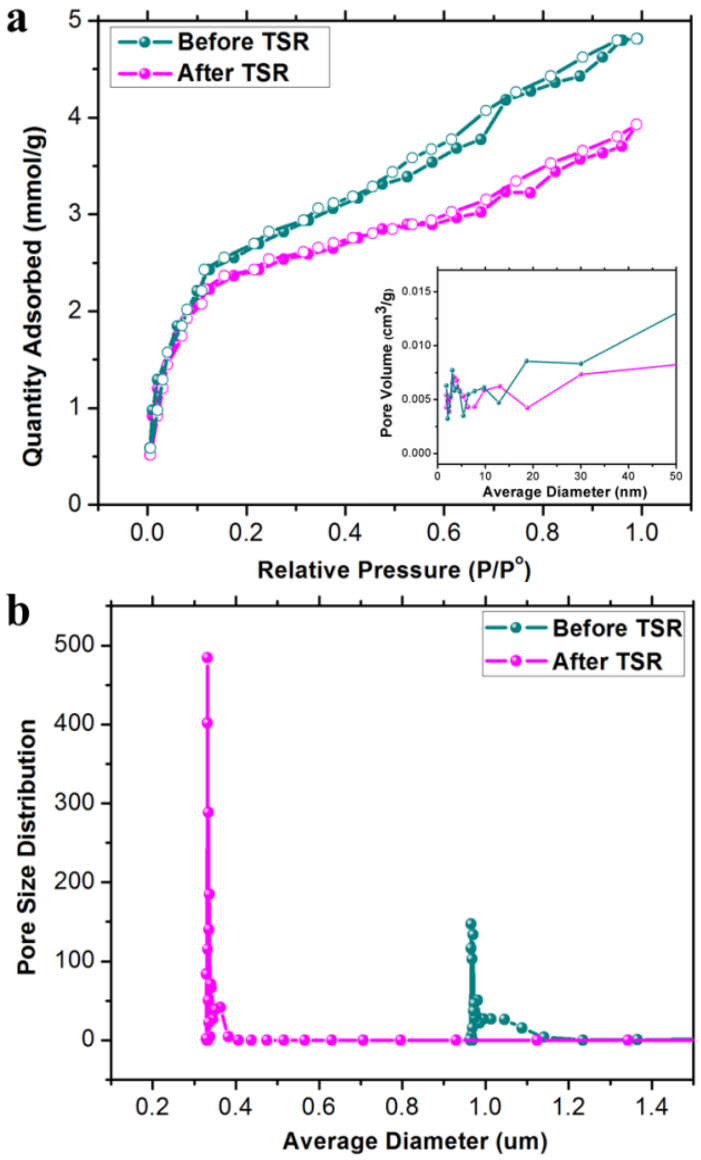

Figure 1-8. Pore Size Distribution Analysis (a) N_2 adsorption-desorption isotherms for RGO coated air cathodes before and after TSR. The inset provides the corresponding BJH pore size distributions calculated from the adsorption branch of the N_2 isotherms. (b) Capillary flow porometry data for pore size distribtion of RGO cathodes before and after TSR. All the cell tests were performed at a current density of 1 A/g within a cut off voltage range from 2.0 V to 4.8 V versus Li/Li^+. The cathode before TSR is same as the cathode at a charged state.

than the change in the amount of residual reaction products. BET surface area of the carbon paper before RGO coating was 5.15 m^2/g, after RGO coating was 232.14 m^2/g. The surface area of the RGO coated carbon paper decreased from that of the RGO powder (574.68 m^2/g) due to the addition of Nafion binder and the use of carbon paper. The cathodes at discharged state, charged state, and charged state after TSR have the BET surface areas of 196.27 m^2/g, 225.09 m^2/g, and 209.36 m^2/g, respectively. Capillary flow porometry profile in Figure 1-8b shows the pore size distribution in large scale (>100 nm) that the majority of pores in the cathodes before and after TSR are concentrated on the size of 0.97 μm and 0.33 μm, respectively. Although the average pore size has been reduced after TSR, the peak values for each case suggest that the pores after TSR become more uniformly distributed than those at charged state before TSR.

From all the analysis presented above, we can postulate the following: the air cathode, once cycled, equipped with the newly aligned three phase interface via mild heat treatment is given a new release of life. As the boiling point of DME electrolyte is 85 ℃, heat treating the air cathode at 120 ℃ under argon atmosphere would eliminate the residual solvent on the surface and rearrange the RGO particles in a way that the formation of their agglomeration during cycle becomes unraveled into the original state with relatively homogeneous pore structure as schematically described in Figure 1-9. After placing the thermally rearranged air cathode back into the system, the entire carbon surface with better contacts and more uniform pore structure is exposed to the newly added electrolyte and further ORR takes place during the discharge process.

The changes in the cathode pore structure, connectivity among the active materials, and electrolyte wetting behavior in and on the thermally rearranged air cathode are the keys to explain complete utilization of the available carbon surface. The strong polarity of the reaction

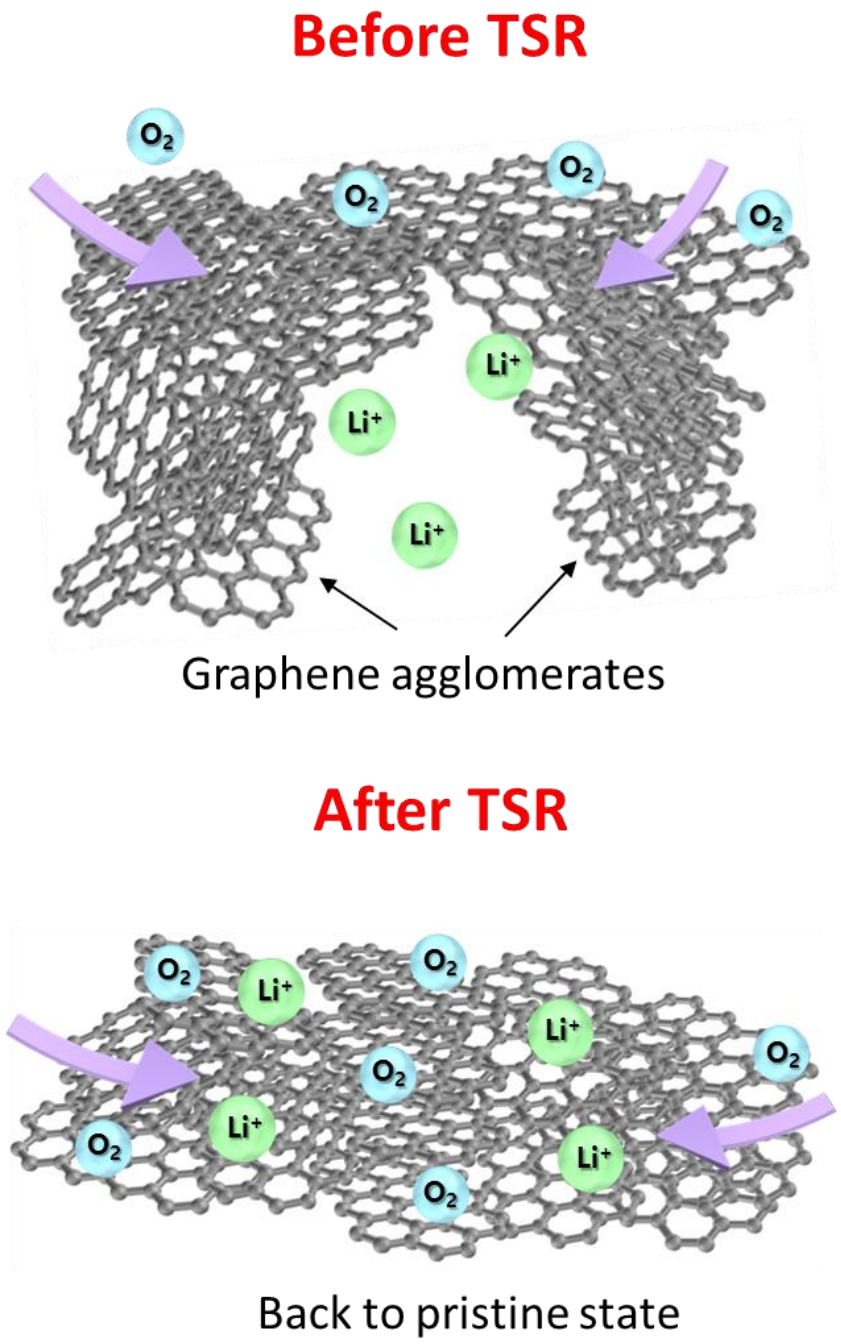

Figure 1-9. Schematic illustration of RGO cathode before and after TSR

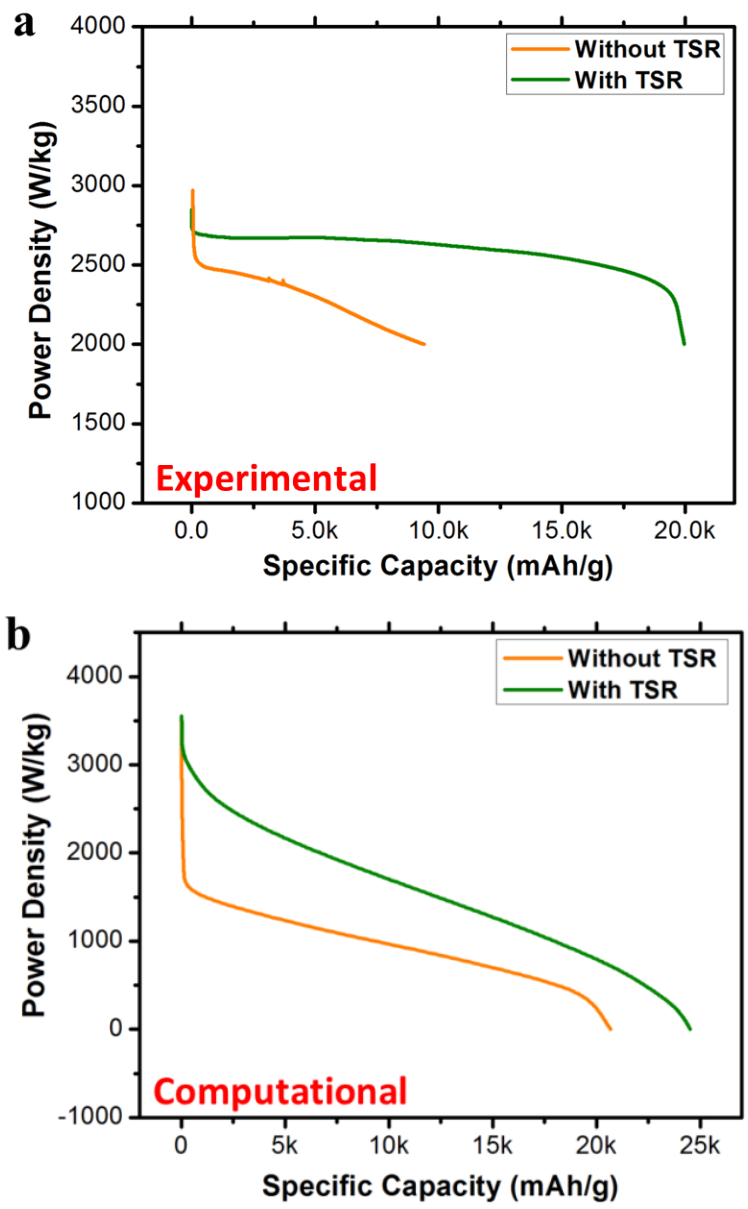

Figure 1-10. Comparison on the 2nd discharge cycle for RGO cathodes with and without the process of TSR between (a) experimental and (b) computational results

products may have blocked the way of the fresh electrolyte permeating through the entire region of the modified carbon surface while oxygen gets full access to the deeper regions of the air cathode.[102] Finally, the uniformly distributed pore structure and reduced thickness along with improved connectivity among active carbon layers on thermally rearranged air cathode not only facilitate the oxygen diffusion into the electrolyte filled pores but also enhance the charge transfer kinetics of the complete cell. [103, 104] In order to further support the strong hypothesis that the reorganization of the cathode structure helps to facilitate the ORR and improve the cycle performance, we demonstrated a numerical analysis by using Runge-Kutta and Lagrange interpolation method with a non-steady-state oxygen continuity equation and with the assumptions including that the process is isothermal, every pore is cylindrical filled with liquid electrolyte, and concentration of oxygen along *r*-coordinate, θ-coordinate of pores are constant. (Figure 1-10) The numerical analysis profiles describe the correlation between specific capacity and current density and between average pore size and the distance along the pore and between oxygen concentration and the distance along the pore as shown in Figure 1-11. Although the shapes of the curves for both experimental and computational results do not look exactly the same due to a number of assumptions made, it gives us an idea that under the fact that the reaction is diffusion-limited with respect to oxygen, the uniformity of the pore structure and the reduced thickness significantly affects the position of the discharge plateaus, which in turn increases the specific capacity. The amount of increase in the specific capacity with and without the process of TSR partially depends on the cut-off voltage. It would reach more to the right and have higher specific capacity in the experimental results when you set the cut-off voltage below2.0 V. Overall, the numerical analysis confirms the fact that the process of TSR helps the reaction for RGO cathodes to become more effective in terms of facilitating the oxygen transport

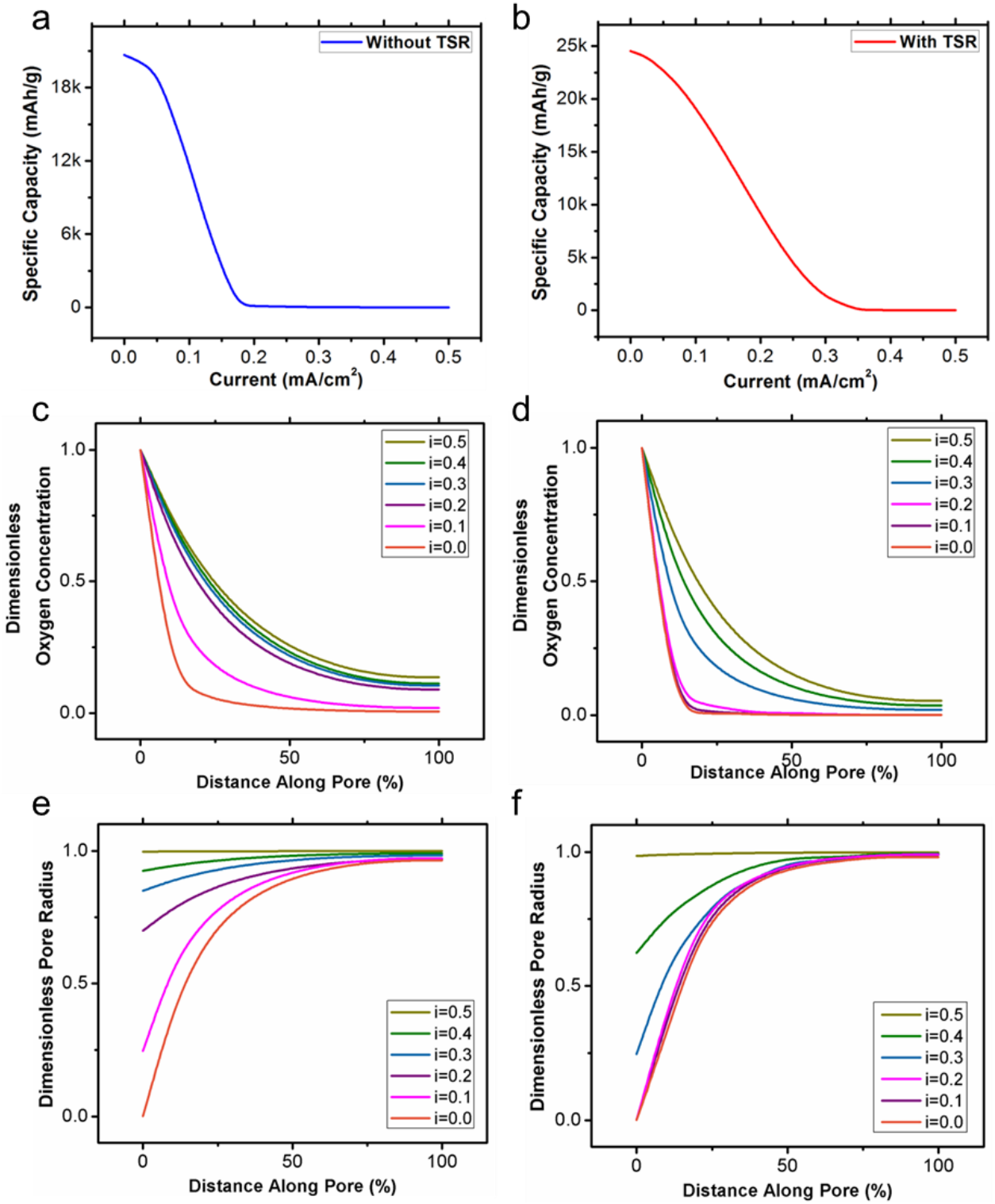

Figure 1-11. Numerical analysis profiles (a, c, e) without TSR (b, d, f) with TSR. Variable i is current density (mA/cm^2). Oxygen concentration, average pore radius and the distance along the cylindrical pore are normalized and dimensionless in all cases.

not to mention the improvement of the charge transfer kinetics.

The idea of thermal swing rearrangement is originated from the temperature swing adsorption (TSA) for separation process, a technology for regenerating a bed of adsorbents that are loaded with the targeted impurity gas. The TSA technique involves adsorbent materials, such as activated alumina, silica gel and zeolites, to adsorb gas at moderate temperatures (~40℃) and later release them when the temperature rises above 120℃. Likewise, we find that the technique is applicable to the lithium-air batteries incorporated within electric vehicles (EV) for that much heat from the motor can be utilized as combustion source of regeneration. Figure 1-12 schematically suggests a way of applying the thermal swing technique to the lithium-air system by letting hot dry air directly go into the air cathode followed by refilling the electrolyte solvent from an electrolyte reservoir. The evaporated electrolyte solvent will be condensed and stored in the reservoir for the purpose of recycling.

As briefly introduced in the first section, highly loaded cathode (7.0 mg/cm^2) was explored and applied with thermal restacking process after each full discharge-charge cycle to confirm that regardless of the type or the amount of carbon used for the air cathode, the method could still improve the battery performance. Figure 1-13a shows the cycle performance of highly loaded CNF cathodes using five different methods in extension to the thermal restacking process comparing with the original cathode without any treatment after each cycle. Interestingly enough, all five methods demonstrated significant improvement in the capacity retention, and one that is involved with the heat treatment at 120 ^{o}C presented the best result. The fact that the mechanically pressed CNF cathode performed relatively poorer can be explained with the low volumetric expansion occurred during discharge and charge process in comparison with the RGO

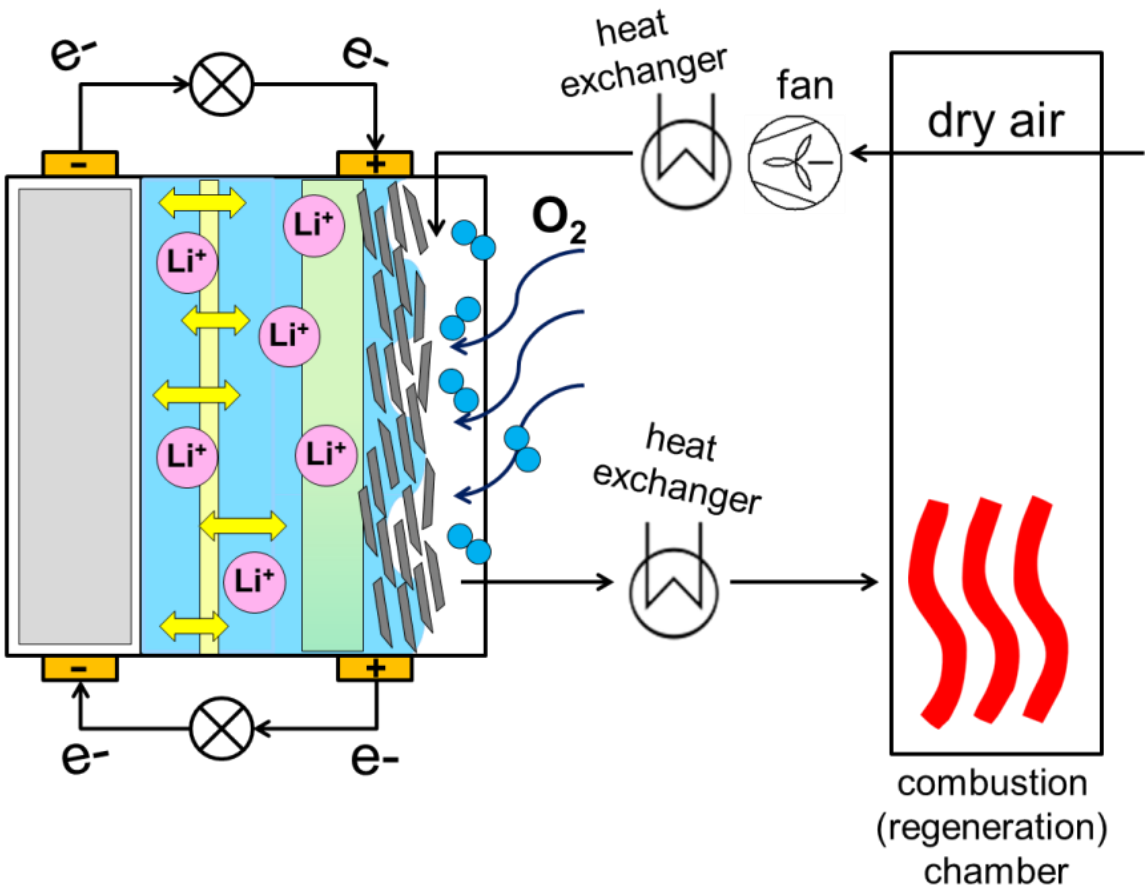

Figure 1-12. Schematic illustration of battery swapping technique replacing the used cathodes with new or thermally rearranged cathodes

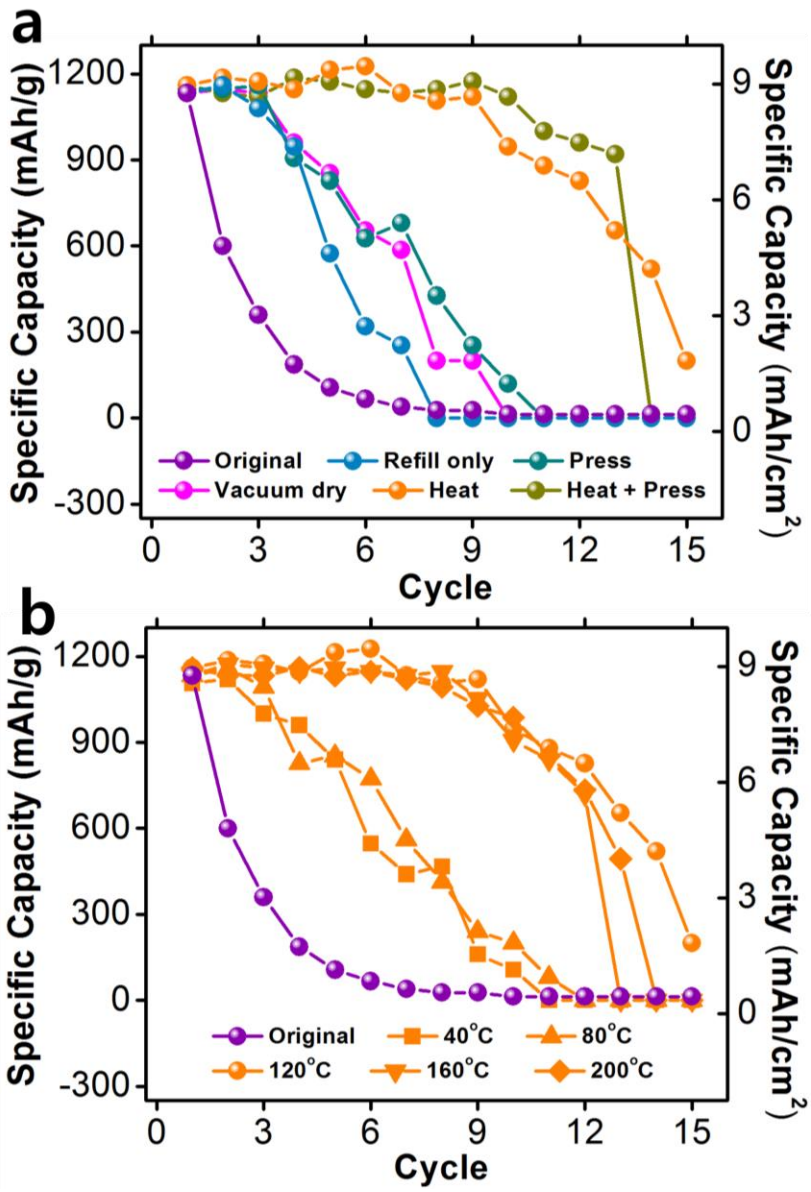

Figure 1-13. Cycle performance of F-CNF cathodes in lithium-air battery cells (a) treated with different methods (50 psi for press, 120 ^{o}C for heat, pores refilled with fresh electrolyte) and (b) heat treated with different temperature (40, 80, 120, 160, 200 ^{o}C) after each full discharge-charge cycle in the voltage range of 2.0 to 4.8 V versus Li/Li^{+} at a current density of 0.3 mA/cm^2.

cathode with 0.1 mg/cm^2 of loading. It is noteworthy that the level of volume expansion caused by the accumulation and subsequent removal of the reaction products varies a lot by the amount of total carbon loading. Due to the diffusion limitation of oxygen, the amount of reaction products inside the cathode pore structure exponentially increases with the decrease in the carbon loading, and therefore, the restacking process becomes less effective in the highly loaded cathode system. However, questions still remain in the cathodes performing with the heat treatment. Figure 5-1b is another cycle performance data concentrating on the heat treatment of the cathodes at different temperatures. Our preliminary analysis data show that there is no difference in the physical configuration of the cathodes heat-treated at different temperatures, and yet, a dramatic recovery of capacity retention is seen from 120 ^{o}C. It needs to be further identified and supported with precise scientific evidence of what have caused this improvement in the capacity retention after heat treating the used cathodes.

CHAPTER II

LITHIUM-AIR BATTERY CATHODE STRUCTURE

SANDWICH STACKING

INTRODUCTION

Non-aqueous lithium-air batteries widely known for their high theoretical energy density stand in the spotlight of the world with an expectation that they could promote electric vehicles or high grid energy storages to the next level. [1-5] This type of battery is composed of four different parts similar to most of the others: lithium anode, liquid electrolyte, insulating polymeric separator, and carbon cathode with oxygen incorporated. The system selection for carbon source and carbon loading for air cathodes is being rigorously discussed since these factors significantly affect the diffusion process of oxygen and determine the practical capacity of the lithium-air batteries which is still distant from its theoretical capacity. Lightweight, highly conductive, highly porous cathode materials such as CNT, [39-41] GNR, [45-47] CNF [51-54] are actively being used to study the effects on the battery performance to work out the drawbacks. However, only a few discussed the structural characteristics of lithium-air battery cathodes and the effect of the amount of carbon loadings using different types of carbon at the same time. [58] In the current study, layered cathodes were fabricated by successively stacking two different carbons selected among the pairs of RGO-CNT, RGO-GNR, or RGO-graphene oxide nanoribbons (GONR). Out of all carbon materials they were chosen as a pair because they possess two

distinct morphologies, which enable the stacking for layered structures. The structural variance of the cathodes controlled by different carbons with different morphologies demonstrated a clear synergic effect in terms of improving the overall performance of lithium-air batteries. With a constant amount of total active carbon materials, but with a different number of layers, the layered cathodes demonstrated a significant increase in specific capacity and decrease in overpotential. Moreover, regardless of the amount of carbon loading, the sandwich-stacked cathodes produced the highest value of all capacities in comparison with single layer or mixed type cathodes, and the more humid environment led to the higher specific capacities in the open air system. This study using different number of alternating graphene layers introduces a way of controlling the macropore structure of cathodes, and therefore, facilitating the diffusion process of oxygen, and suggests a promising strategy in designing oxygen diffusion pathways of cathodes.

EXPERIMENTAL METHODS

i) CATHODE FABRICATION AND CELL ASSEMBLY

Lithium metal disc purchased from MTI Corp. was used as anode. 1 M lithium trifluoromethanesulfonate ($LiCF_3SO_3$) / 1, 2-dimethoxyethane (DME) were purchased from Sigma-Aldrich and used as an electrolyte solution which impregnated a glass fiber separator (GF/D, Whatman). GNR and GONR were made by unzipping multi-walled CNTs gifted from Hodogaya Chemical Corp. with hexadecyl-functionalization and oxidation. Carbon (RGO, CNT, GNR, GONR) and polytetrafluoroethylene (PTFE) binder were dispersed in isopropyl alcohol (5 mL) in a weight ratio of 80:20. The slurries were ultra-sonicated for 30 minutes in a glass dish filled with ice, stirred overnight and drop casted onto a gas diffusion substrate (Toray, TGP-H-030). The weight of the cathode was measured carefully with ultrahigh precision scale (~0.0001 g) after placing each layer. The as-fabricated cathodes were dried overnight and transferred to the glove box for cell assembly. The total amount of carbon loaded on the substrate is 0.5 ± 0.01 mg/cm^2, and the weight ratio of RGO gifted from Dongjin Semichem and CNT/GNR/GONR is 70:30 in all cases. Cell assembly begins with placing a lithium disc foil on top of the Swagelok-type self-designed stainless steel lithium-air chamber followed by a glass fiber soaked by electrolyte (310 µl) and the cathode and stainless steel current collector. A Teflon tube with O-rings centering on both top and bottom was then placed surrounding all the cell components sideways followed by placing a load string connected to the other half of the stainless steel chamber. All of the assembly process was done in the argon filled glove box. (< 0.5 ppm. O_2 and H_2O) The lithium-air battery chamber was then taken out from the glove box and purged with ultrahigh purity oxygen for 5 min to replace the inside argon gas.

ii) ELECTROCHEMICAL AND STRUCTURAL CHARACTERIZATION

EIS was evaluated at the electrochemical workstation (Princeton Applied Research, PARSTAT 4000) within a frequency range of 50,000 to 0.01 Hz using 5 mV input voltage amplitude. The galvanostatic tests were performed under a cut-off voltage window from 2.4 V to 4.8 V versus Li/Li^+ in the voltage limit profile by using BST8-MA (MTI Corporation) multi-channel battery testing system at a current density of 0.05 mA/cm^2. The discharge-charge performance was controlled by Neware BTS system. All tests were carried out under the oxygen pressure of 1 atm. The observed capacity and applied current densities were normalized by the weight of the total carbon layers coated on top of the substrate. The nanostructured morphologies of the cathode materials were observed by TEM (FEI F20 Tecnai) and FE-SEM (Tescan Mira3). The cathodes were taken out in the argon filled glove box, stored and carried in a vial wrapped with a parafilm to prevent the air flowing inside and were transferred to the SEM anti-chamber which was then evacuated immediately. Electrolyte contact angle measurement was performed on a contact angle goniometer (Rame-Hart 500) with automated dispensing system which can be controlled by the workstation. One drop of electrolyte requires an amount of 100 µl. The surface properties were further investigated by XPS spectroscopy (Surface Science Instruments, SSX-100) at ~ 2 x 10^{-9} Torr operating pressure, and monochromatic Al K-alpha X-rays (1486.6 eV) were used with beam diameter of 1 mm. Photoelectrons were collected at a 55 degree emission angle. A hemispherical analyzer determined electron kinetic energy, using pass energy of 150 V for wide/survey scans, and 50 V for high resolution scans. Pore size distributions of cathodes in micro-scale (> 0.1 µm) were obtained by the capillary flow porometer (Porous Materials, Inc., CFP-1100-AEHXL). Silwick with surface tension of 20.1 dynes/cm was chosen as the wetting liquid. The thickness of each cathode was measured five times with the high precision digital

thickness guage with up to 0.001 mm (Mitutoyo), averaged out and confirmed by the FE-SEM cross-sectional images. Conductivity measurements of the sandwich-stacked cathodes were performed by using a 4-point probe set up (Cascade CP06) with a Keithley 2400 as a sourcemeter. The source current was 0.2 A, and measurement range was 100 mV.

RESULTS AND DISCUSSION

Two different types of carbon were used in one lithium-air battery cathode. The pairs selected in this study are RGO-CNT, RGO-GNR, and RGO-GONR. The RGO is used in all pairs because of its exceptionally high electrical conductivity, high specific surface area, and well-dispersive nature in slurry solvents such as water or isopropyl alcohol. It is noteworthy that by controlling the structure of cathode with fixed amount of total carbon loading using any one of those pairs, wide variations in the electrochemical performance of lithium-air battery cell were observed. The size of RGO is about 5 μm in width, 3 μm in length. CNT, GNR or GONR has much higher aspect ratio with 0.2 μm in diameter and 50 μm in average length. GONR is produced from GNR through chemical oxidation, and GNR is obtained from unzipping the multi-walled CNT. As schematically illustrated in Figure 2-1a**,** sandwich-stacked cathodes were fabricated by alternating drop casting method from respective slurry solution using different pairs of carbon. The high aspect ratio of CNT, GNR and GONR and their entanglement allow sandwich stacking with RGO layers on top of a gas diffusion layer (GDL). Figure 2-1b and 2-1c are FE-SEM cross-sectional images of the 7-layer cathode with alternating layers of RGO and GONR. The thickness of each cathode layer is measured approximately 5~7 μm. Figure 2-1d and 2-1f are FE-SEM images of RGO and GONR, and Figure 2-1e and 2-1g are transmission electron microscopy (TEM) images of one single particle of RGO and GONR, respectively. The inset in Figure 2-1a is a digital photo image of as-fabricated cathode with alternating layers of RGO and GONR. The alternating layers are very clearly placed and seen for their large difference in the aspect ratio. The C: O atomic percentage ratio of RGO, CNT, and GNR measured by the XPS full survey spectrum is approximately 9:1 whereas that of GONR is 7:3, showing that GONR has

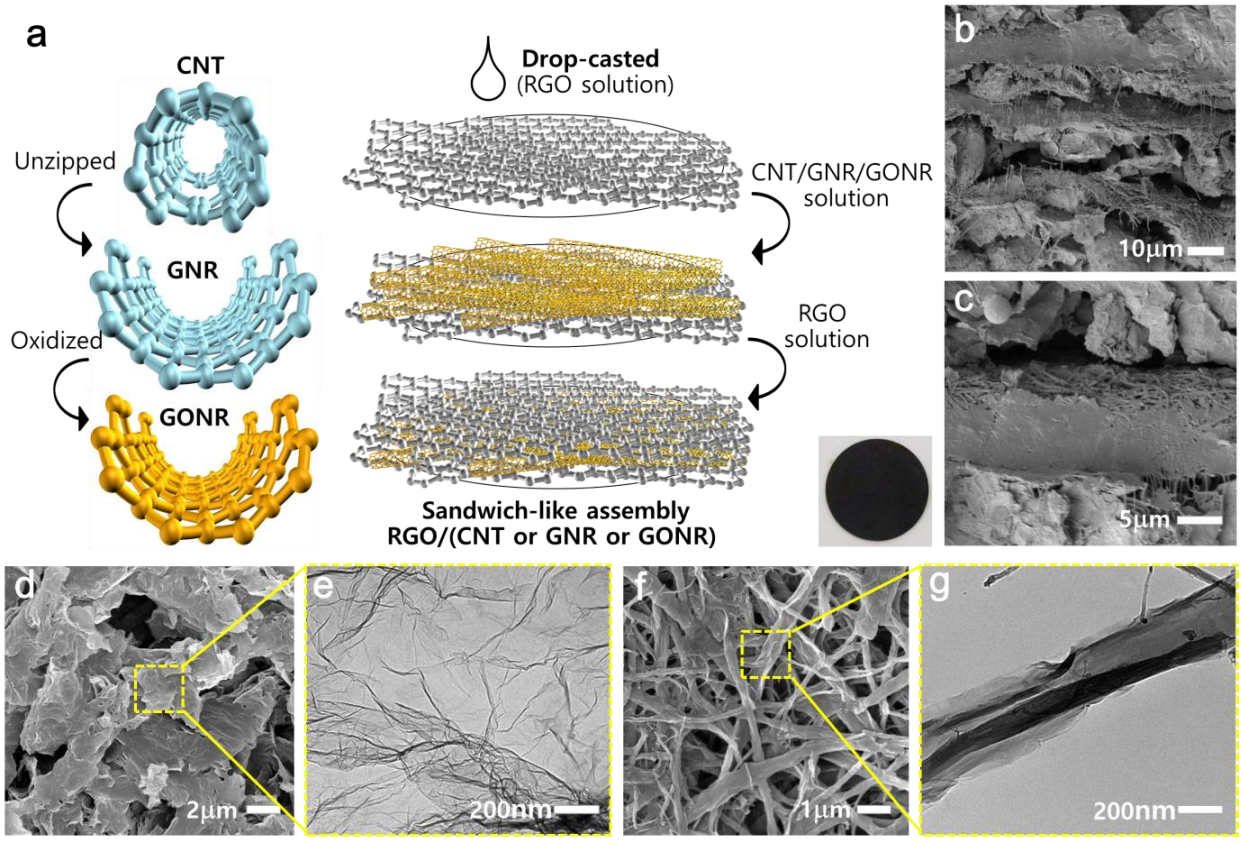

Figure 2-1. a) Schematic illustration of sandwich-stacked cathodes; b) c) cross-sectional FE-SEM images of RGO-GONR sandwich-stacked cathode; d) top view FE-SEM image and e) TEM image of RGO layer; f) top view FE-SEM image and g) TEM image of GONR layer

more oxygen functionalities as shown in Figure 2-2. Figure 2-3a and 2-3b show the FE-SEM images of CNT and GNR, respectively. The diameter of CNT is approximately one half of the diameters of GNR or GONR. By simply mixing or alternating two different carbon materials with different number of layers and comparing one after another in this study, the structural parameter of the lithium air cathode has emerged to be critical to its electrochemical performance. The weight ratio of RGO and high aspect ratio carbon (CNT, GNR, and GONR) is always fixed at 70:30 for all cases, and each layer for each cathode is equally distributed in weight within the total amount of each material. For sandwich-type cathodes, different odd numbers of layers (1 to 9) were coated with fixed amount of total carbon loading (0.5 mg/cm^2), having the first and the last layers always RGO. As the total number of layers increases, each layer for each cathode contain less amount of materials so it could match the total amount of carbon. For example, in the case of 7-layer cathode, there are four layers of RGO and three layers of CNT, GNR or GONR, alternating by one after another, and each layer of RGO weighs approximately 0.1 mg/cm^2 and CNT, GNR, or GONR 0.05 mg/cm^2, whereas in the case of 3-layer cathode, the weights are 0.18 mg/cm^2 and 0.15 mg/cm^2, respectively. The weight of the cathode was carefully measured every time each layer was casted.

i) SANDWICH STACKING OF RGO-GONR

a) EFFECT ON ELECTROCHEMICAL PERFORMANCE

Figure 2-4a and 2-4b shows both voltage limit and capacity limit profiles of single layer cathodes. Each cathode layer is composed of one single material selected among RGO, CNT, GNR, and GONR, and the carbon loading is 0.5 mg/cm^2 in all cases. The single layer RGO cathode shows the superior performance of 3,500 mAh/g of specific capacity in its first deep cycle and 21 cycles

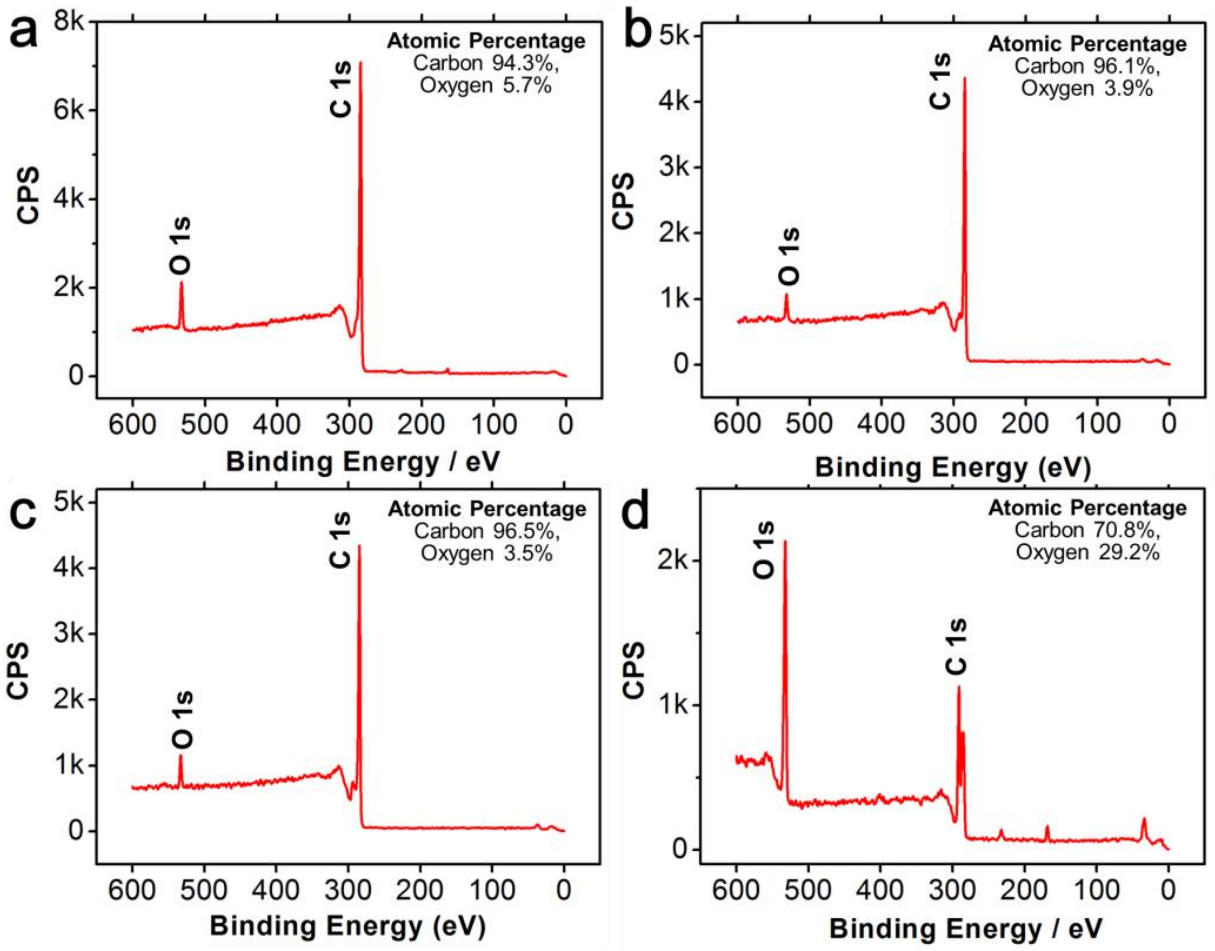

Figure 2-2. XPS survey spectrum of a) RGO, b) CNT, c) GNR, and d) GONR

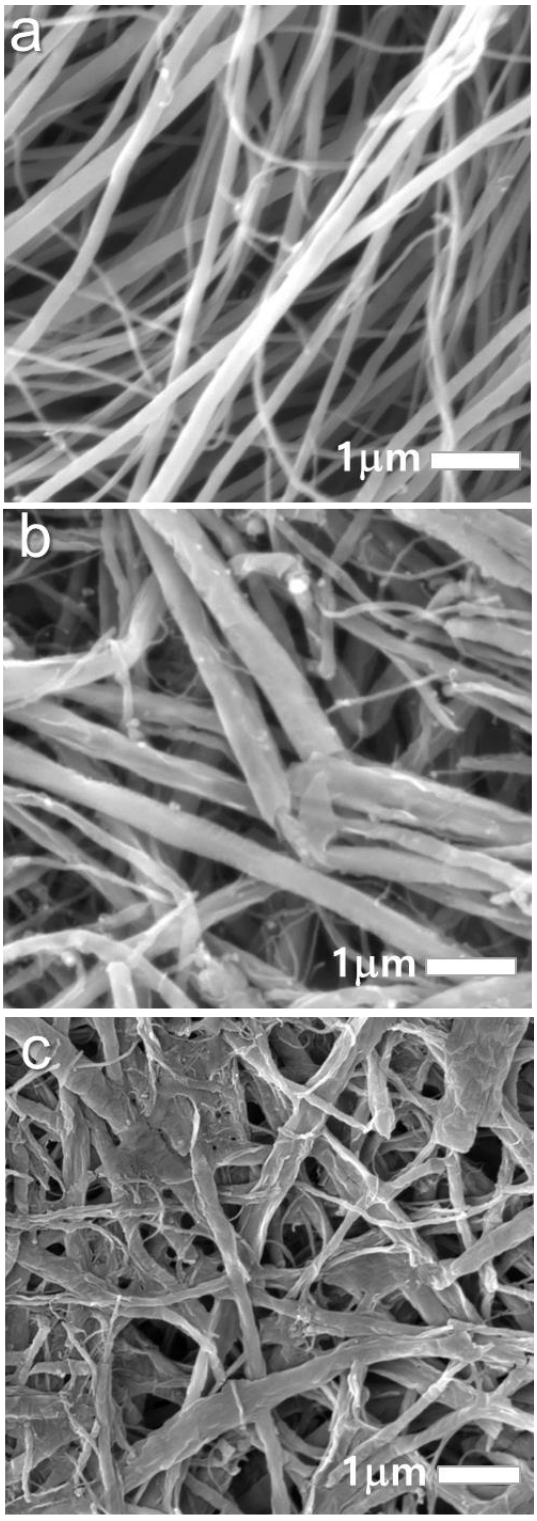

Figure 2-3. High resolution FE-SEM images of a) CNT, b) GNR, and c) GONR

at a limited capacity of 1,000 mAh/g at a current density of 0.05 mA/cm^2. The single layer GNR cathode shows 2,100 mAh/g, CNT 1,500 mAh/g and GONR show less than 500 mAh/g for their first discharge capacities at the same current density. There may be a number of different factors associated with the difference in the electrochemical performance for each different type of carbon. The specific pore surface area, electrical conductivity, the type and amount of functional groups and defects on the surface are normally responsible for determining the electrochemical properties when applied to electronic devices. In this study, however, we focus more on the structural aspect of cathode as a whole instead of looking into one specific material, which no one hitherto showed interests and studied in depth in the field of lithium-air batteries.

The electrochemical profiles of the RGO-GONR cathodes with different number of layers at a current density of 0.05 mA/cm^2 are presented in Figure 2-5. Among all the pairs, the sandwich-stacked RGO-GONR 7-layer cathode produced the highest specific capacity, and the specific capacities of the sandwich-stacked cathode with different number of layers varied from 1,745 mAh/g (3-layer) to 13,458 mAh/g (7-layer), which is almost one order of magnitude difference with the same types and the same amount of total carbon loaded. The sandwich-type or mix-type RGO-GONR cathodes showed relatively poor cyclability with capacities limited to 1,000 mAh/g as shown in Figure 2-5b. The low cycle number could partially be attributed to the irreversible byproducts generated from parasitic reactions during charge associated with the abundant defects and the oxygen functionalities on the surface of GONR, [96, 106] and partially to the intermittentinterconnected network within the cathodes due to a low volumetric mass density from two carbon system which would contribute to the charge transfer resistance. The mix-type RGO-GONR cathode showed the greatest cycle performance among other types of RGO-GONR

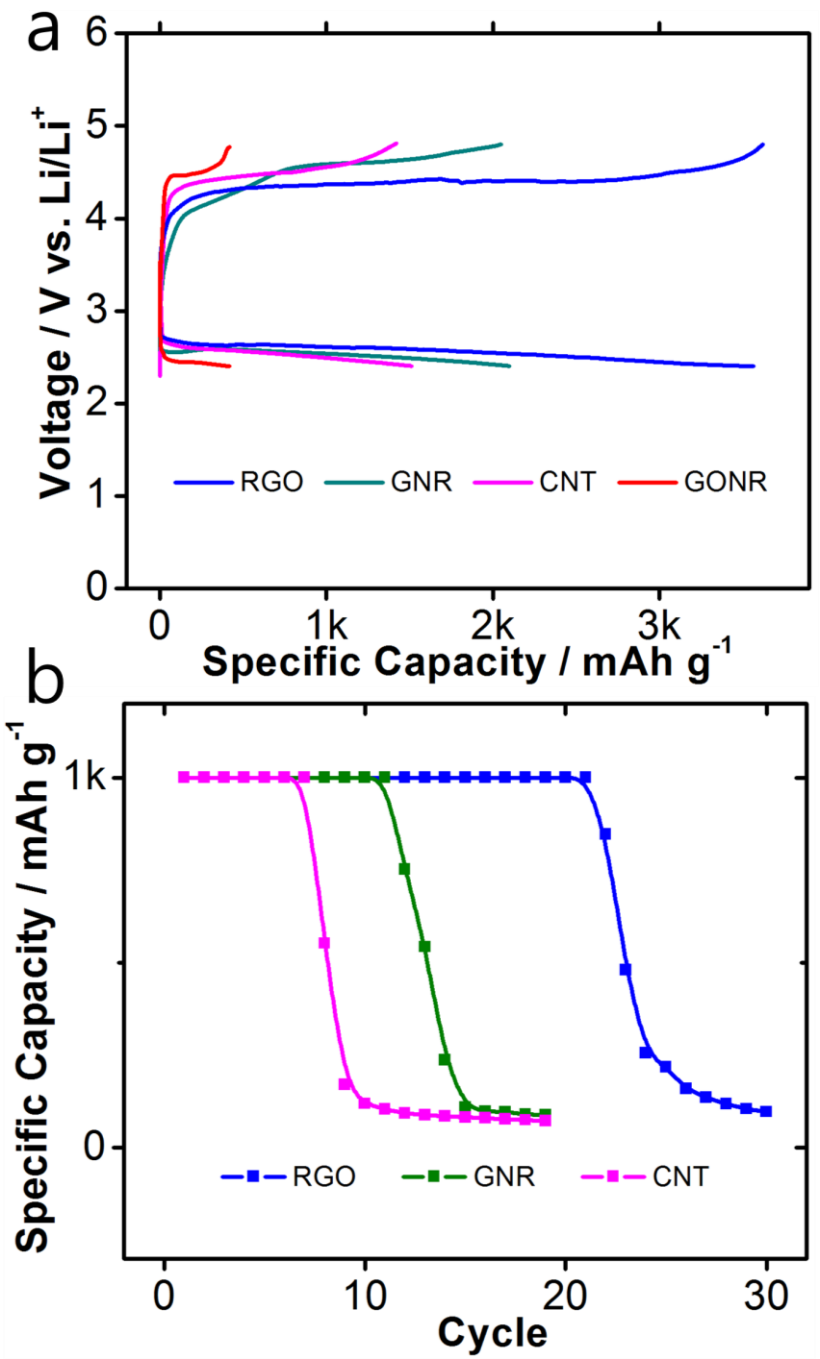

Figure 2-4. a) Voltage limit profiles (2.4 ~ 4.8 V) of the 1st discharge-charge cycles of single layer cathodes and b) capacity limit profiles with cycle life of single layer cathodes with limited specific capacity of 1,000 mAh/g

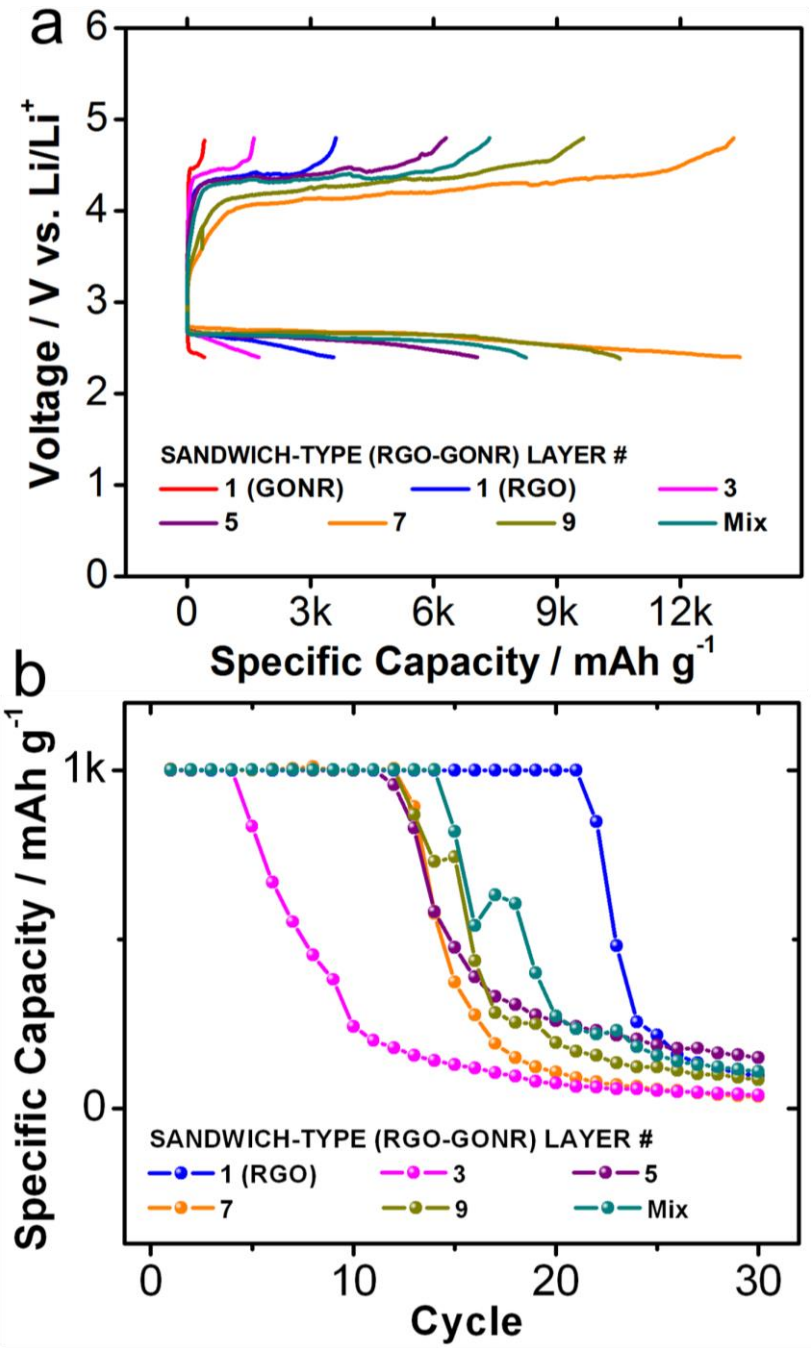

Figure 2-5. a) Voltage limit profiles (2.4 V ~ 4.8 V) of the 1st cycles, b) capacity limit profiles (1,000 mAh/g) with cycle life, of sandwich-stacked RGO-GONR cathodes with different number of layers. The carbon loading is 0.5 mg/cm^2 and the current density is 0.05 mA/cm^2 in all cases.

cathodes supposedly due to the increased interconnectivity among active and conductive carbon particles. Figure 2-6 shows the first twelve discharge-charge cycles of capacity limit profiles of RGO-GONR 7-layer cathodes with operating voltage versus specific capacities. The shapes of the discharge and charge curves of the capacity limited profiles of RGO-GONR cathodes look very much alike in all cases. The discharge and charge overpotentials slowly increase over cycle by cycle to a point where it hit the operating voltages. Figure 2-7 shows the change in capacities of RGO-GONR cathodes with increasing amount of carbon loading, and regardless of the amount, the sandwich-type RGO-GONR cathode achieved the highest capacities of all. The tested carbon loadings were 0.23, 0.5, 1.07, 2.61, and 4.29 mg, which correspond to 3, 7, 15, 37, and 61 alternating layers of RGO and GONR in the sandwich-stacked cathodes, and each layer weighs the same with that of the 7-layer cathodes. Because the oxygen diffusion is hugely limited in the liquid phase electrolyte the higher carbon amount leads to the lower gravimetric specific capacities and eventually arrives at the total capacity threshold in the non-aqueous lithium-air system. Attempts to overcome this systematic limitation were made in this study by using an environment of controlled relative humidity. The higher relative humidity led to the higher specific capacities of the sandwich-type RGO-GONR (61 layers) cathode as shown in Figure 2-7b. At 90% of the relative humidity the RGO-GONR cathode performed 18 mAh/cm^2 at a current density of 0.05 mA/cm^2, which is by far the highest number of specific capacity achieved and reported in the literature with less than 5 mg/cm^2 loading of total active carbon.

b) EFFECT ON ELECTROCHEMICAL PROPERTIES

Electrochemical impedance spectroscopy (EIS) data were obtained on the lithium-air cells with sandwich-type RGO-GONR cathodes with different number of layers. The greater width of the

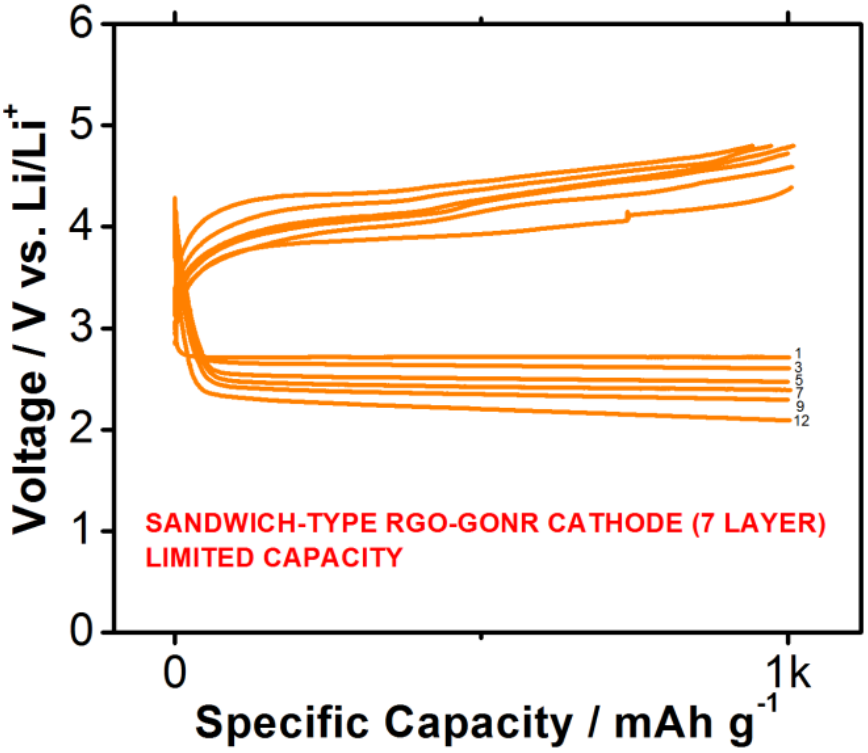

Figure 2-6. Capacity limit profiles of sandwich-type RGO-GONR cathodes (7-layer)

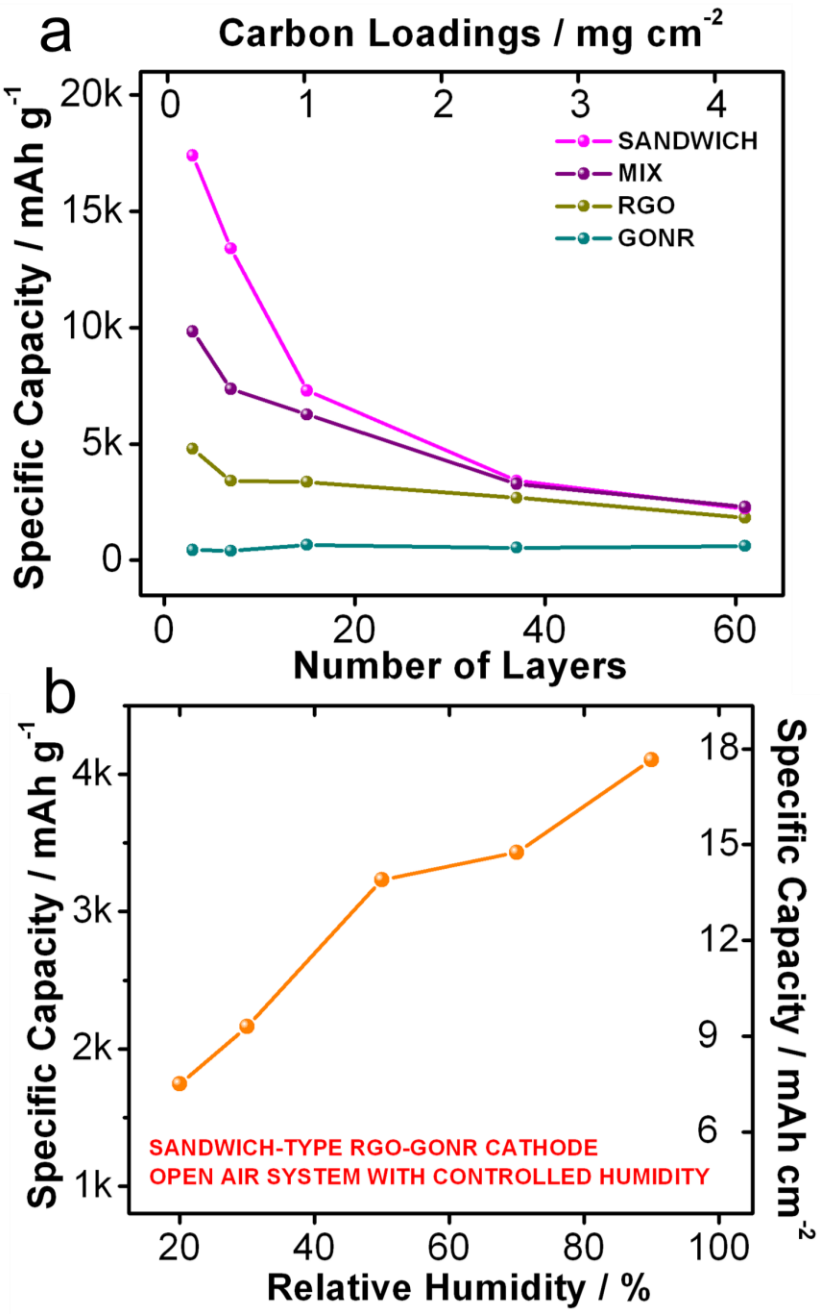

Figure 2-7. Electrochemical performance of RGO-GONR cathodes a) specific capacity versus carbon loading for single layer RGO or GONR, mixed, sandwich-stacked cathodes; b) full discharge capacities for highly loaded sandwich-stacked RGO-GONR cathodes (61 layer) in an open air system with controlled humidity.

semicircle of the Nyquist plots indicates the higher polarization resistance, and therefore the slower charge-transfer kinetics. The single layer GONR cathode has the greatest width of the semicircle whereas the smallest width belongs to the single layer RGO cathode as shown in Figure 2-8a. The onset of the semicircle at the highest frequency indicates the electrolyte resistance, and there is hardly any difference in this value in all cases. Among RGO-GONR cathodes with different number of layers, 3-layer cathode presented the largest charge transfer resistance whereas 9-layer cathode showed the smallest. This result consistently indicates that the higher number of layers produce the lower charge transfer resistance and reduce the discharge and charge overpotential accordingly. Capillary flow porometry profiles in Figure 2-8b demonstrate the pore size distribution of interparticle pores, that are larger than 100 nm in diameter, of the sandwich-type RGO-GONR cathodes with different number of layers. The result shows that the more alternating layers give larger interparticle pores inside the cathode structure. The single layer GONR cathode produced the smallest average pore size of ~500 nm in diameter but with the highest peak intensity, which indicates that the GONR cathode possess the largest number of pores within the size range. The next smallest average pore size of ~900 nm belongs to the single layer RGO cathode. And, all the other RGO-GONR cathodes with alternating layers have larger pore size than that of the single layer cathodes. It is confirmed by the data that the more number of alternating layers produce the larger average interparticle pore size within the cathode structure, and apparently, the 9-layer cathode showed the largest average pore size of ~1.3 μm in diameter. All the characterization experiments were performed under the same condition, and the amount of total carbon loading is fixed to 0.5 mg/cm^2 in all cases.

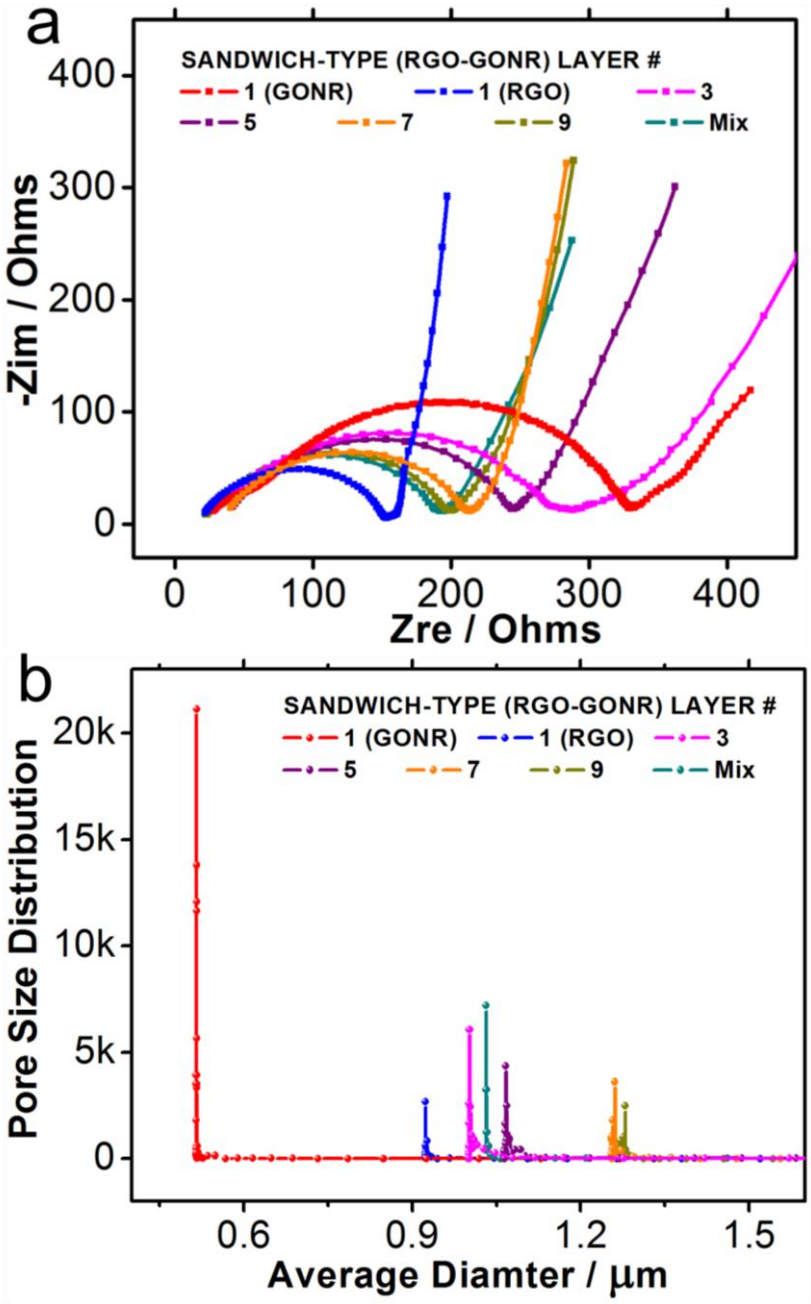

Figure 2-8. a) EIS spectra and d) capillary flow porometry profiles of sandwich-stacked RGO-GONR cathodes with different number of layers. The carbon loading is 0.5 mg/cm^2.

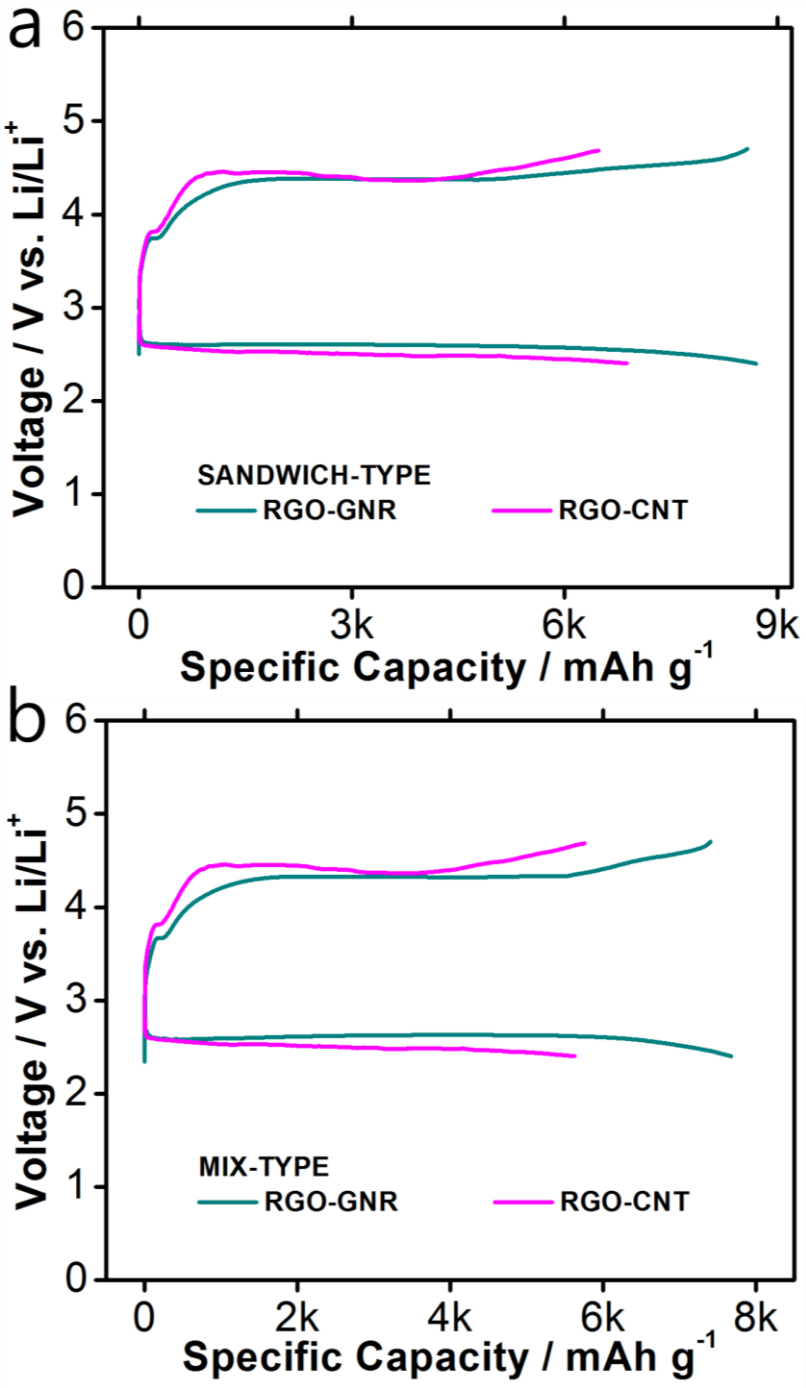

Figure 2-9. Electrochemical performance of sandwich-stacked and mixed cathodes with different pairs of carbon: voltage limit profile (2.4 V ~ 4.8 V) of the 1st cycles of (a) sandwich-stacked (7-layer) and (b) mixed cathodes with different pairs of carbon. The carbon loading is 0.5 mg/cm^2 and the current density 0.05 mA /cm^2 in all cases.

ii) SANDWICH STACKING OF RGO-CNT AND RGO-GNR

a) EFFECT ON ELECTROCHEMICAL PERFORMANCE

The comparisons of sandwich-stacked and mixed cathodes with two different pairs of carbon (RGO-GNR, RGO-CNT) in electrochemical performance are presented in Figure 2-9. Single layer cathode of RGO had greater specific capacity (3,564 mAh/g) than the single layer cathode of the GONR, GNR, or CNT, and both mixed and sandwich-stacked cathodes produced higher specific capacities than the single layer RGO cathode. RGO-GNR pairs showed the highest discharge specific capacities in both sandwich-stacked and mixed cathodes, and RGO-CNT followed in order. The more important aspect of this part of study is that the sandwich-stacked cathodes produced higher discharge specific capacities the mixed cathodes in all cases when comparing the same pairs. The total carbon loading in all cases is fixed to 0.5 mg/cm^2 and the cells were operated at a current density of 0.05 mA/cm^2. The weight ratio of RGO and GNR or CNT is 7:3 in all cases. In terms of rechargeability, the sandwich-stacked RGO-GNR 7-layer cathode produced the longest cycle life as presented in Figure 2-10 which outnumbers that of the single layer RGO cathode in Figure 2-5b. In fact, the cycle life of sandwich-stacked RGO-GNR cathode is almost twice as long as what was expected. ((Cycle number of RGO x 7 + cycle number of GNR x 3) / 10) The cycle lives of sandwich-stacked RGO-GNR or RGO-CNT cathodes are always longer than those of the mixed cathodes with the corresponding pair. On the other hand, the rechargeability of the sandwich-stacked RGO-GONR cathode is shown to be poorer than that of the mixed RGO-GONR cathode. The difference in RGO-GONR cathodes in rechargeability is thought to be attributed to the presence of oxygen functional groups on the surface of GONR particles, which are known to be detrimental to the formation and dissociation

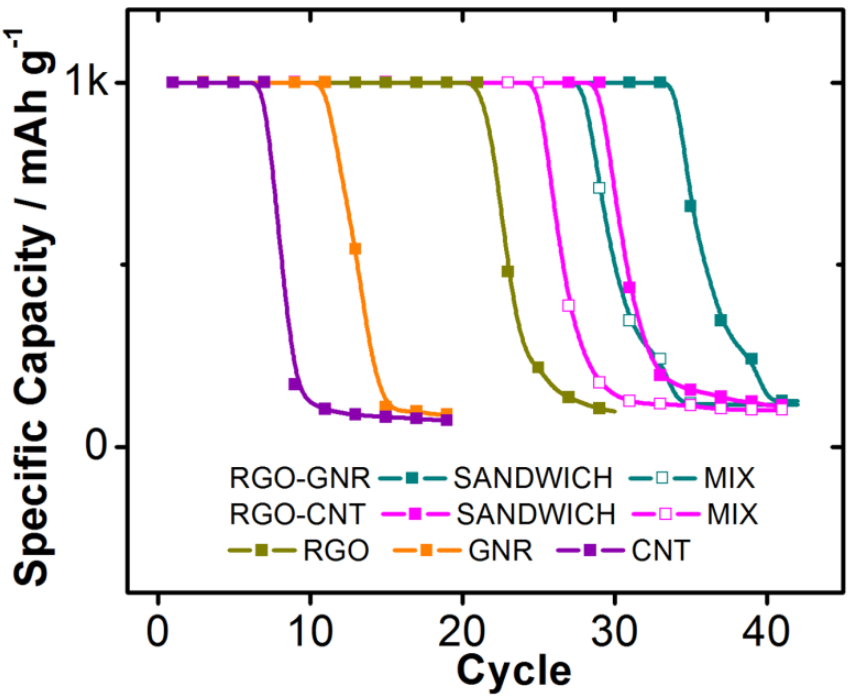

Figure 2-10. Electrochemical performance of sandwich-stacked and mixed cathodes with different pairs of carbon: capacity limit profiles with respect to cycle life. The carbon loading is 0.5 mg/cm^2 and the current density 0.05 mA /cm^2 in all cases.

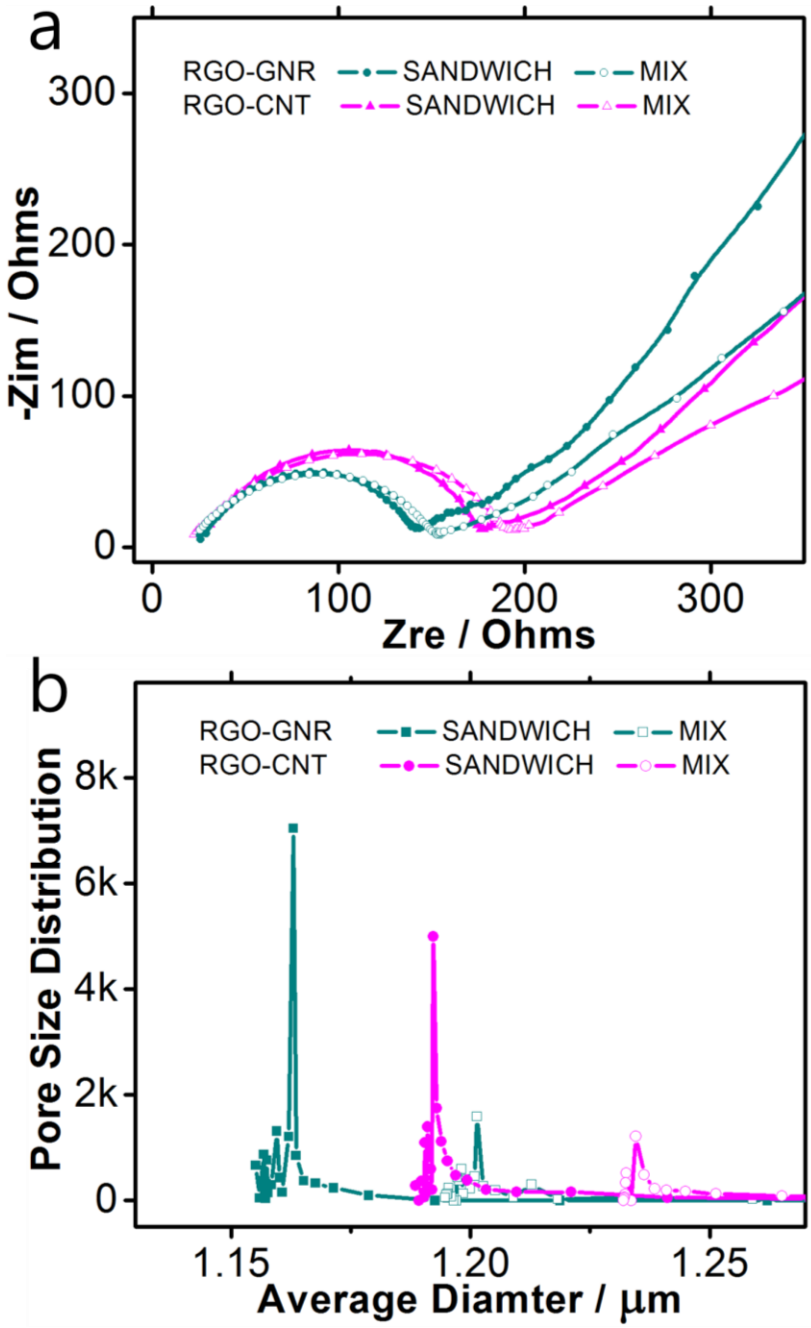

Figure 2-11. Characterization of sandwich-stacked and mixed cathodes with different pairs of carbon. a) EIS spectra, b) capillary flow porometry profile of pore size distribution. The carbon loading is 0.5 mg/cm^2 in all cases.

of lithium peroxides (Li_2O_2) during charge and the kinetics of oxygen evolution reaction (OER) and cause parasitic reactions to produce irreversible lithium carbonates (Li_2CO_3). In addition to GNR having the larger specific surface area, the flexibility of GNR as compared to CNT may also have participated in the improvement of interconnectivity among particles and the charge transfer kinetics of the cathode.

b) EFFECT ON ELECTROCHEMICAL PROPERTIES

EIS spectra of the complete cells that contain sandwich-stacked and mixed cathodes in Figure 2-11a show that the tilt angles of the tails of the Nyquist plot of the cell with sandwich-stacked cathodes in the low frequency region are higher than those of mixed cathodes in all cases, while the widths of the semicircles of the Nyquist plot of sandwich-stacked cathodes are smaller than those of mixed cathodes in all cases. This result indicates that the mix and sandwich-stacked cathodes have different diffusion mechanism of lithium ions on the SEI of active cathode materials. Figure 2-11b shows the capillary flow porometry data of both mixed and sandwich-stacked cathodes with different pairs of carbon. Unlike the RGO-GONR pair, the average pore sizes of the sandwich-stacked RGO-GNR or RGO-CNT cathode are smaller than those of the mixed cathodes with the corresponding pairs. However, judging from the significant differences in the peak intensity values the pores of sandwich-stacked RGO-GNR or RGO-CNT cathode are more uniformly distributed throughout the cathode structure than the mixed cathodes. This result indicates that when the two particles are mixed, they tend to agglomerate more severely and create larger pores in response.

Electrolyte contact angle measurements show the difference in the surface properties of all cathodes presented in this paper. (Figure 2-12a) The main reaction takes place on the three-phase

interface of active materials within the cathodes, and the electrolyte wettability is another important parameter to approximate the reaction responsible areas. [107-109] According to a number of literature reported, the partially wetted surface of cathodes by liquid electrolyte is highly conducive to oxygen diffusion into the cathode system which will enhance the electrochemical properties of the complete lithium-air battery cell. However, superhydrophilicity is not the answer for acquiring the maximum area of the three-phase interface. It is crucial to control and meet the optimum level of hydrophobicity of the carbon surface with respect to the polarity of liquid electrolyte. RGO-GONR cathodes have the highest electrolyte contact angles among the three pairs, and RGO-GNR cathodes have the lowest largely attributing to the amount of oxygen functional groups on the surface of each cathode. The highest discharge specific capacities of lithium-air battery cells using RGO-GONR cathodes may be responsible for their optimum level of electrolyte wettability which could have maximized the area of reaction sites within the cathode structure. The facilitated oxygen diffusion associated with the electrolyte wettability will increase the number of reaction sites, reduce the discharge and charge overpotential, and finally improve the specific capacities not to mention the cycle life of the lithium-air battery cells.

Electrical conductivities and volumetric mass densities were also measured and plotted in Figure 2-12b. It is noteworthy that the RGO-GONR cathodes are more densely packed than the other two presumably because the highly dispersive nature of GONR in the slurry solution produced less number of agglomerates and entanglements. RGO-GNR cathodes are slightly denser than RGO-CNT cathodes because GNR is designed to be more flat and flexible than CNT, which allows more particles to be placed in a unit volume. The density of 7-layer RGO-GONR cathode

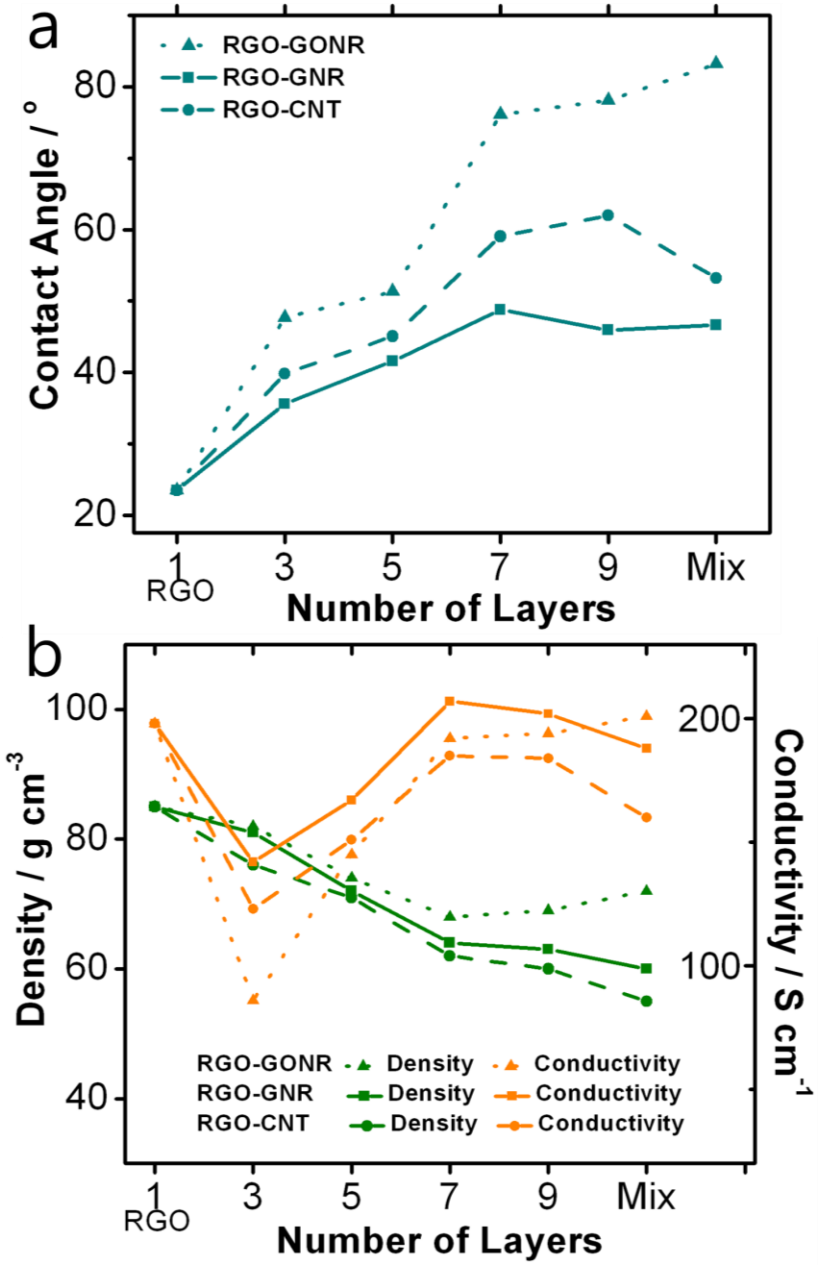

Figure 2-12. Characterization of sandwich-stacked and mixed cathodes with different pairs of carbon: a) electrolyte contact angle measurements, and b) density and electrical conductivity of sandwich-stacked and/or mixed cathodes with different pairs of carbon with different number of alternating layers. The carbon loading is 0.5 mg/cm^2 in all cases.

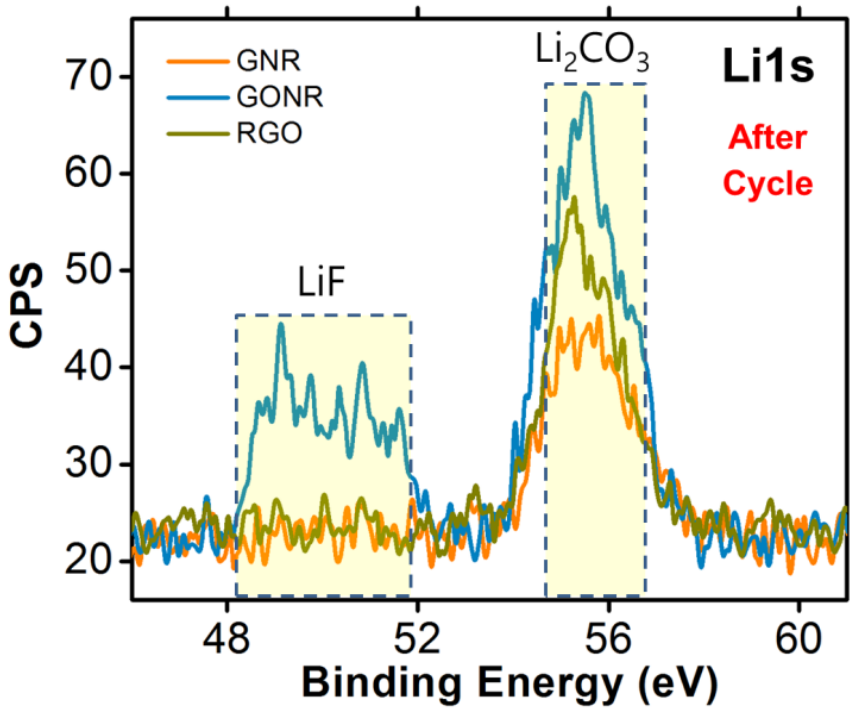

Figure 2-13. Li 1s high resolution XPS spectrums of single layer GNR, GONR, and RGO cathodes after a full discharge-charge cycle

is slightly lower than that of the 9-layer RGO-GONR cathode whereas the densities of the other 7-layer cathodes remain slightly higher. And it is also noteworthy that the mixed RGO-GONR cathode shows both higher density and higher electrical conductivity than the sandwich-stacked 7-layer RGO-GONR cathode whereas the other two pairs go the opposite way. This is because the highly dispersive nature of GONR has started making layers thin enough so they overlap with the layers of RGO and become more like the mixed cathodes at 9-layer RGO-GONR cathode and has prevented the agglomeration of GONR when GONR is mixed with RGO and promoted the interconnectivity among the mixed particles. This explains well the sudden drop in the discharge specific capacity of 9-layer cathode from 7-layer cathode even with the fact that 9-layer RGO-GONR cathode showed lower charge transfer resistance and higher electrical conductivity than 7-layer RGO-GONR cathode, and that the 9-layer cathode had the largest average interparticle pore size. The 9-layer cathode with the higher density and the larger average interparticle pore size leads to the smaller active specific surface area of the entire pores and therefore to the reduced specific discharge capacity. GNR and CNT are much less dispersive in slurry solution and produce agglomerations when mixed with RGO, and this makes the thicknesses of mixed RGO-GNR and RGO-CNT cathodes become even higher than those of corresponding sandwich-stacked cathodes and lose the electrical conductivity.

The three types of graphene, GNR, GONR, and RGO used in the sandwich stacked cathodes were further characterized individually with XPS analysis. Each single layer cathode using 0.5 mg/cm^2 loading of GNR, GONR, and RGO was fully discharged and charged in the voltage range of 2.0 V to 4.8 V. The outcome of its surface spectrum in Figure 2-13 shows that the amount of surface functional groups on the surface of graphene is directly proportional to the

amount of irreversible byproducts such as lithium fluorides (LiF) and lithium carbonates (Li_2CO_3) generated during discharge and charge process. This result matches well with the poor cycle performance of RGO-GONR cathodes and the significant improvement in RGO-GNR cathodes. Thus, it is highly recommended to review and further investigate the correlation between the carbon surface functional groups and the formation of electrochemically irreversible byproducts during cell operation.

In summary, sandwich-stacked cathodes composed of alternating two different graphenes demonstrate the improvement in the electrochemical performance of lithium-air batteries largely due to the enhanced diffusion process of both lithium ion and oxygen and possibly to the enlarged three phase interface caused by the change in the surface properties. Controlling and comparing the lithium-air battery cathode structures by laying different number of alternating layers or simply by mixing the two, the physical configuration along with its surface chemistry has been found to be the key parameter to consider when designing the more efficient lithium-air battery cell, in a way that the entire pore surface of the carbon cathode can be fully utilized, the diffusion of oxygen be facilitated, and the charge transfer kinetics of the entire cell be improved.

CHAPTER III

LITHIUM-AIR BATTERY CATHODE STRUCTURE

FUSED NANOFIBER

INTRODUCTION

By limiting the capacity the over-accumulation of primary reaction products and/or byproducts from parasitic reactions can be avoided. [7, 110] However, in order for this technology to be considered commercially viable, the volumetric capacity must outnumber that of the existing lithium-ion battery, and by limiting the capacity and with the addition of air channels experts started feeling dubious about its feasibility of commercialization. In this study, we have discovered a way to improve the capacity retention over discharge-charge cycles with and without limiting the capacity by applying mechanical pressure onto the as-spun nanofiber during the pre-oxidation process of fabricating freestanding carbon nanofiber (F-CNF) cathode. Our results indicate that the cause of the capacity drop is not only because of the formation of electrochemically irreversible byproducts filling up the cathode pores due to electrolyte decomposition or carbon surface oxidation or because of the insulating nature of primary reaction products but also because of the disruption of carbon structure due to the subsequent removal of over-accumulated reaction products within the pores of carbon cathode during charge.

F-CNF was chosen as a lithium-air battery cathode for its superior porosity fully accommodating

the volume expansion and structural damage during discharge and charge process which we have discovered in our previous studies. In addition, no polymeric binder is used in fabricating F-CNF cathode, which enhances the interconnectivity for electron transport pathways. In this study, four different F-CNF samples with different average fiber diameters and average interfiber distances were spun by using different electrospinning parameters such as applied voltage or polymer concentration. They were chosen for comparison in full discharge specific capacity and oxygen reduction reaction (ORR) kinetics by both experiments and simulations. Although the experimental results were commensurate with our numerical analysis in their discharge specific capacities, four samples presented very similar capacity retention over a number of discharge-charge cycles within the voltage window of 2.0 V ~ 4.8 V. Controlling the structural parameter such as average pore size or specific surface area by changing the electrospinning condition was confirmed to be less conducive in enhancing the cycle life, while directly related to the change in gravimetric specific discharge capacities. On the other hand, the thermo-mechanical stabilization of F-CNF fabrication process and higher ramping rate of the pre-oxidizing temperature have produced the unique type of F-CNF which the fibers are fused with each other, and the as-fabricated F-CNF as the lithium-air battery cathode demonstrated significant improvement in the capacity retention largely due to the fact that the full discharge and charge process did not affect or alter the cathode structure from continuous cycle of accumulation and removal of the reaction products. Moreover, this method of fabrication alerts a synergistic effect when combined with sandwich stacking of other types of carbon additives such as Super P or RGO, serving as an ultimate solution for the lithium-air battery cathode.

EXPERIMENTAL METHODS

i) F-CNF CATHODE FABRICATION AND CELL ASSEMBLY

PAN solution was prepared by dissolving PAN purchased from Sigma-Aldrich with an average molecular weight of 150,000 in DMF solvent. The solution was stirred overnight at 45 ^{o}C on a hot plate. Air-assisted electrospinning was used to form a fibrous mat. The electrospinning conditions were different by each sample as described in Figure 3-3. The controlled parameters are air pressure, applied DC voltage, distance between the tip of the syringe needle and copper wire mesh current collector, inner core flow rate of PAN solution for the syringe pump, size of the needle, rotating speed of the current collector drum, size of the current collector, relative humidity, and the concentration of PAN in the solution. The stirred PAN solution is poured carefully in the disposable 5 mL plastic syringe purchased from BD, and the co-axial needle designed by rame-hart is placed at the tip of the syringe. The introduction of air into the outer shell makes the flow rate and the corresponding production rate faster by an order of magnitude. The collected fibers undergo thermal stabilization at a ramping rate of 1 ◦C/min to 260 ^{o}C for 1 hour in the air furnace for and carbonization at 10 ^{o}C/min to 900 ^{o}C for 3 hours under nitrogen atmosphere. The carbonized PAN nanofiber was cut in a disc size of 1.56 cm in diameter and directly used as the lithium-air battery cathode. The weight of total freestanding carbon nanofiber per unit area is around 0.5 mg/cm^2 in all cases. The fabricated freestanding air cathodes were dried overnight at 95 ^{o}C in an air furnace and then transferred to the glove box filled with ultrahigh purity argon gas for cell assembly. (< 1 ppm O_2 and H_2O)

Lithium-air cell assembly begins in the argon filled glove box with placing the lithium disc foil (1.56 cm diameter, 0.025 cm thickness, MTI Corp.) on top of a stainless steel disc, a bottom part

of the Swagelok-type chamber that has been self-designed in the lab. A glass fiber (GF/D, Whatman) dried overnight at 95 ^{o}C in an air furnace was then placed on top of the lithium foil. 300 µl of the 1 M lithium trifluoromethanesulfonate ($LiCF_3SO_3$) and 1,2-dimethoxyethane (DME) electrolyte solution purchased from Sigma-Aldrich and purified by 3 Å molecular sieve was injected into the glass fiber followed by immediately placing the as-prepared F-CNF cathodes. A Teflon tube with O-rings was placed surrounding all the cell components sideways followed by placing a load string connected to the other half of the stainless steel disc. The lithium-air battery chamber was then taken out from the glove box and purged with ultrahigh purity oxygen for 5 min to replace the inside argon gas.

ii) ELECTROCHEMICAL AND STRUCTURAL CHARACTERIZATION

EIS was evaluated at the electrochemical workstation (Princeton Applied Research, PARSTAT 4000) within a frequency range of 20,000 to 0.01 Hz using 1 mV input voltage amplitude. The galvanostatic tests were performed under a cut-off voltage window from 2.0 V to 4.8 V versus Li/Li^+ in the voltage limit profile by using BST8-MA (MTI Corporation) multi-channel battery testing system at a current density ranging from 0.05 mA/cm^2 to 0.3 mA/cm^2. The discharge-charge performance was controlled by Neware BTS system. All tests were carried out under the oxygen pressure of 1 atm. The observed capacities were normalized by the total weight of the F-CNF cathode, the current densities by the area of the F-CNF cathode. The nanostructured morphologies of the F-CNF at each different state were observed by TEM (FEI F20 Tecnai) and FE-SEM (Tescan Mira3). Electrolyte contact angle measurement was performed on a contact angle goniometer (Rame-Hart 500) with automated dispensing system which can be controlled by the workstation. One drop of electrolyte requires an amount of 100 µl. The surface properties were further investigated by XPS spectroscopy (Surface Science Instruments, SSX-100) at ~ 2 x

10^{-9} Torr operating pressure, and monochromatic Al K-alpha X-rays (1486.6 eV) were used with beam diameter of 1 mm. Photoelectrons were collected at a 55 degree emission angle. A hemispherical analyzer determined electron kinetic energy, using pass energy of 150 V for wide/survey scans, and 50 V for high resolution scans. Pore size distributions of cathodes in micro-scale (> 0.1 μm) were obtained by the capillary flow porometer (Porous Materials, Inc., CFP-1100-AEHXL). Silwick with surface tension of 20.1 dynes/cm was chosen as the wetting liquid. The thickness of each cathode was measured five times with the high precision digital thickness guage with up to 0.001 mm (Mitutoyo), averaged out and confirmed by the FE-SEM cross-sectional images. Conductivity measurements of the sandwich-stacked cathodes were performed by using a 4-point probe set up (Cascade CP06) with a Keithley 2400 as a sourcemeter. The source current was 0.2 A, and measurement range was 100 mV. N_2 isotherms and pore size distribution in mesoscales (1 ~ 50 nm) were obtained from a Micromeritics Gemini VII 2390 surface area analyzer. Specific surface areas were calculated by BET method. Pore volumes and areas were estimated from the adsorption isotherms using the BJH method.

RESULTS AND DISCUSSION

i) FABRICATION AND CHARACTERIZATION OF CNF

F-CNF cathodes are top notch and notable for they use no addition of the polymeric binder or a metal substrate which lightens the entire cell to a great extent without compensating the specific capacities. On the process of making F-CNF cathodes, precursor solution was prepared by using PAN with an average molecular weight of 150,000 in DMF organic solvent. Samples were stirred overnight at 45 ^{o}C. Air-assisted electrospinning was used to form a fibrous mat as schematically described in Figure 3-1b. [111-113] The introduction of air into the outer shell of the electrospinning needle assured the pumping or the production rate faster by an order of magnitude. The as-spun fibers were heat treated at a ramping rate of 1 ^{o}C/min to 260 ^{o}C for an hour in air for stabilization or pre-oxidation process to maintain the fiber morphology and at 10 ^{o}C/min to 900 ^{o}C for 5 hours under high purity nitrogen atmosphere for carbonization. The carbonized PAN nanofiber also named in this study as F-CNF was cut in a disc size of 1.56 cm in diameter and directly used as the air cathode. The as-fabricated air cathodes were dried overnight at 95 ℃ and transferred to the glove box for cell assembly.

Figure 3-1d and 3-1f shows the FE-SEM images of the as-spun fibers and carbonized fibers, respectively, by using 12 wt.% of PAN in DMF solution. The average diameter of the as-spun fiber significantly decreases on the process of carbonization not to mention its flexibility. The electrical conductivity of the F-CNF cathode is in the range of 250 to 300 S/cm. Figure 3-2 shows the XPS analysis of both full spectrum and high resolution of C1s and O1s of the F-CNF cathode. The atomic percentage of C: O: N is approximately 8: 1: 1. The most of the oxygen functional groups are formed during pre-oxidation stage whereas the nitrogen groups are derived

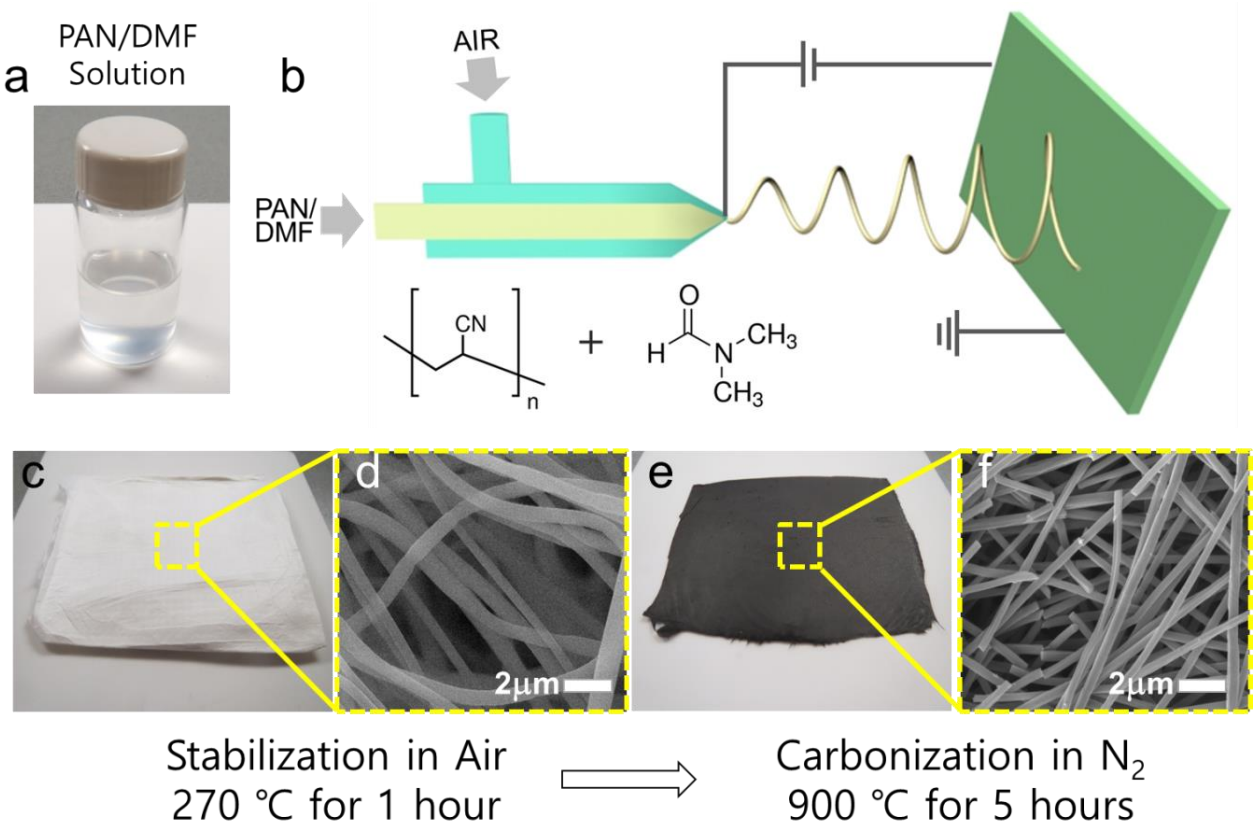

Figure 3-1. Lithium-air battery cathode fabrication. (a) 12 wt% PAN/DMF solution, (b) schematic illustration of air-assisted electrospinning as a process of making nonwoven nanofiber mat, (c) photo image of a PAN as-spun fiber, (d) SEM image of (c), (f) photo image of a carbonized PAN nanofiber, (g) SEM image of (f)

from the remaining parts of nitrile groups from PAN fibers. In order to remove all the functional groups on the surface, a further graphitization process at 2,000 ^{o}C under inert gas environment must be done. [114, 115] However, some of the oxygen and nitrogen functional groups on carbon surface are known to be beneficial to the electrochemical performance of the electronic devices in general, [116-121] and our focus in this study is not about the chemistry of carbon surface that affects the electrochemical properties of lithium air battery cathodes, but more about the structure and its mechanical stability.

Figure 3-3 demonstrates a number of different as-spun PAN fiber samples and their properties of average interfiber pore distance and average fiber diameter by controlling six different electrospinning parameters: 1. pump rate, 2. size of the needle, 3. rotating speed of the cylindrical current collector drum for highly aligned fibers, 4. size of the current collector, 5. weight concentration of PAN in DMF solution, 6. distance between the tip of the needle and the current collector. Among all the samples presented, four of them with wide variations in the average interfiber pore distance and average fiber diameter were chosen to investigate deeper in terms of electrochemical properties when applied to the lithium-air battery cathodes as marked with red circles in Figure 3-3. Each chosen sample has its own unique structural characteristic and was listed with both low and high resolution FE-SEM images in Figure 3-4. The sample type 4 had the largest average interfiber distance whereas sample type 2 had the smallest. In terms of the average fiber diameter the sample type 4 again had the largest whereas type 3 had the smallest. The BET specific surface area of each sample was also calculated from N_2 adsorption isotherm data measured by the surface analyzer. The BET surface areas of the sample type 1, 2, 3, and 4 are 132, 111, 159, and 94 m^2/g, respectively.

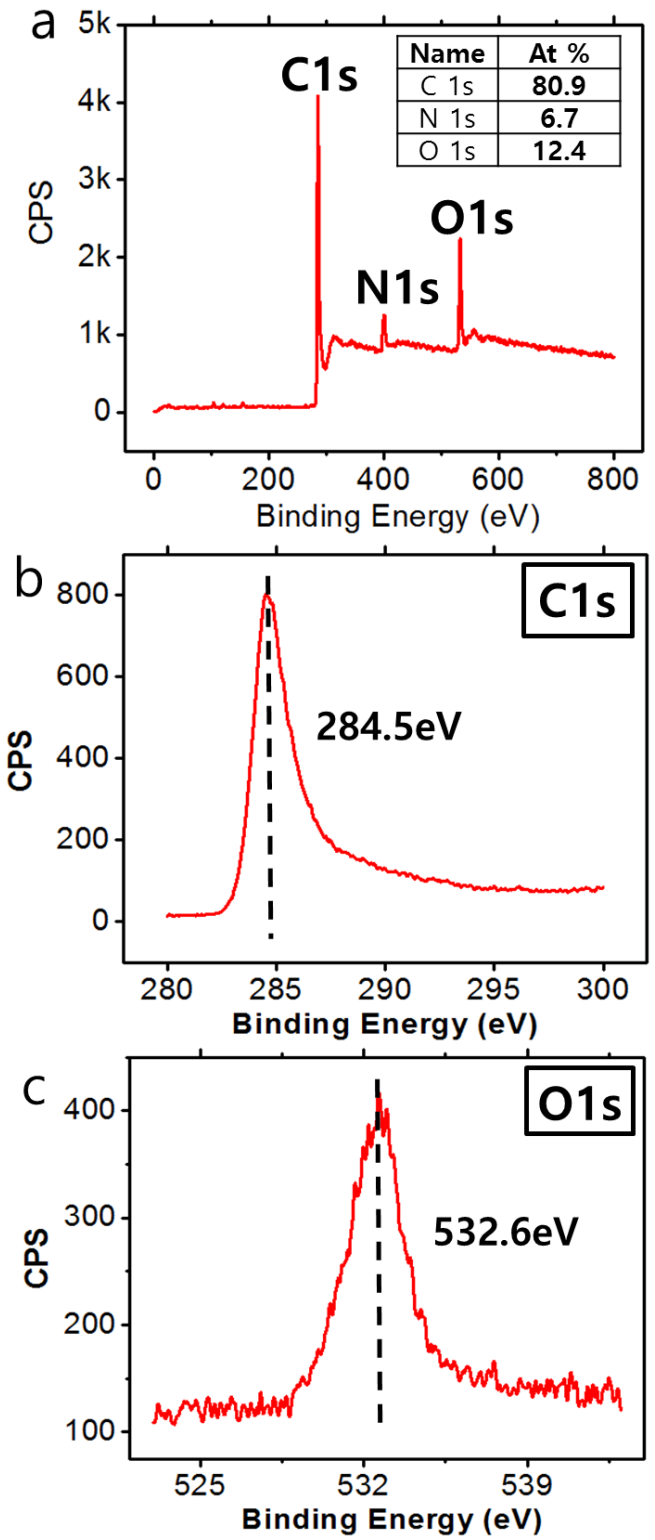

Figure 3-2. XPS analysis of both full spectrum and high resolution of C1s and O1s of F-CNF cathode

ii) MODELING AND EXPERIMENTS OF CELL PERFORMANCE OF CNF

The discharge curves in voltage limit profiles (2.0V) and the corresponding discharge specific capacities of the lithium-air battery cells using the four different F-CNF samples chosen as the air cathodes are presented in Figure 3-5a. The sample cathode type 1 shows the highest discharge specific capacity of 8,009 mAh/g, whereas the sample cathode type 2 showed the lowest of 5775 mAh/g. The discharge overpotential of each cathode follows the order of the specific capacities. It is worth noting that despite the highest BET specific surface area, sample cathode type 3 did not produced the highest discharge capacity, and sample type 4 with the lowest BET surface area showed higher specific discharge capacity than sample type 2. This result indicates that the BET method that measures the specific surface area of the entire pores is hardly a determining factor when deciding which sample would store more of the reaction products. Interestingly, the sample cathode type 1 with mediocre average interfiber distance, mediocre average fiber diameter, and mediocre BET specific surface area performed the greatest in terms of discharge specific capacity, which may indicate that the uncounted specific pore volume has contributed to the additional reaction sites, oxygen diffusion pathways and storages for the reaction products. Moreover, the difference in other fiber properties such as rigidity and electrical conductivity due to the structural variance may have influenced the overall electrochemical performance. Figure 3-5b shows a theoretical result utilizing the diffusion limited, non-steady state, two-dimensional numerical model with respect to the flow of oxygen that has already been presented in the first part of this study. [14] The assumptions include that the process is isothermal, every pore is cylindrical filled with liquid electrolyte, and concentration of oxygen along *r*-coordinate, θ-coordinate of pores are constant. The discharge curve of theoretical result for each of the sample

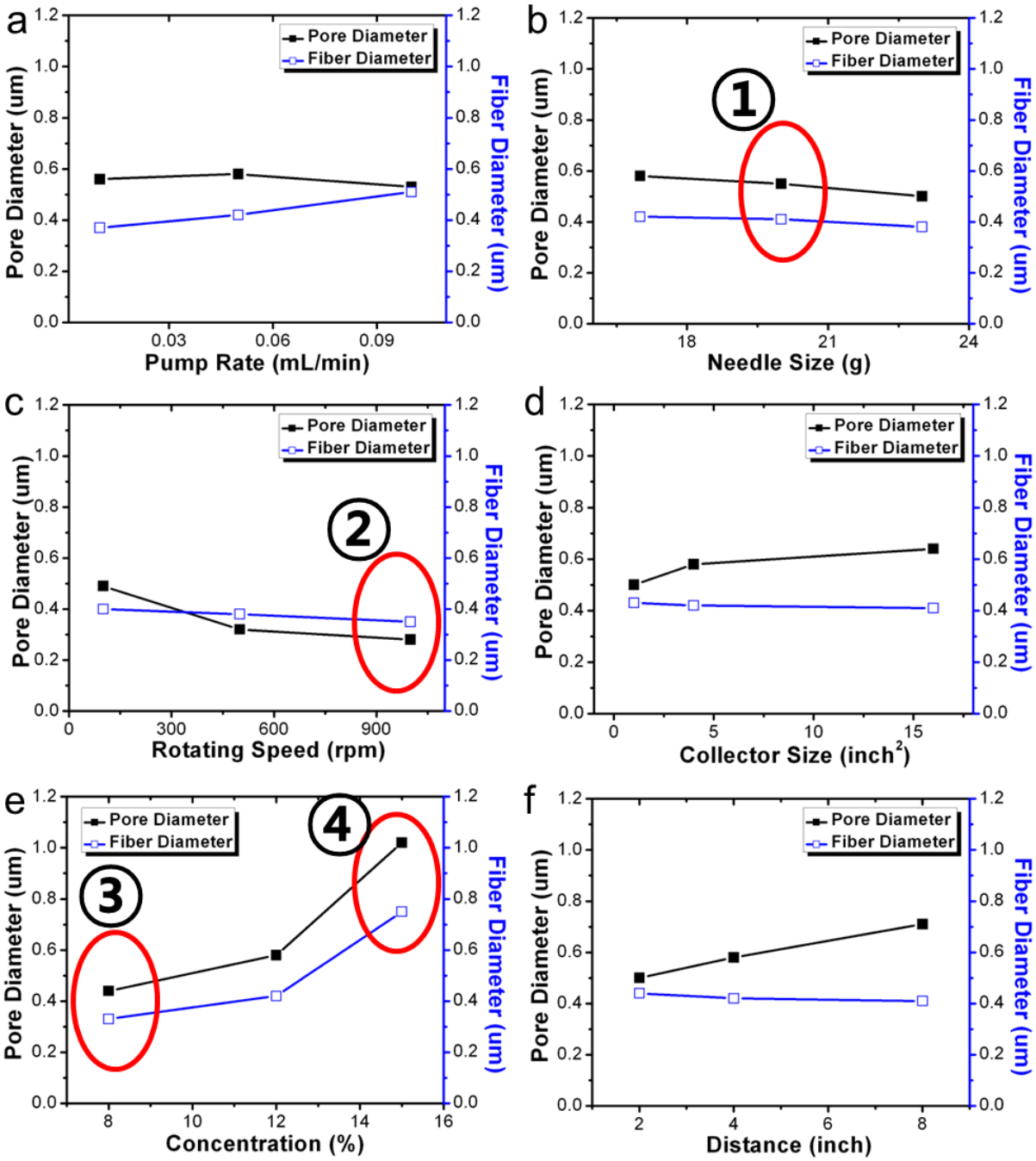

Figure 3-3. Fiber property profiles of the average interfiber pore distance and the average diameter of as-spun PAN fibers along with six different electrospinning parameters: a) pump rate, b) size of needle, c) rotating speed of the cylindrical current collector for highly aligned fibers, d) size of the current collector, e) weight concentration of PAN in DMF solution, f) distance between the tip of the needle and the current collector

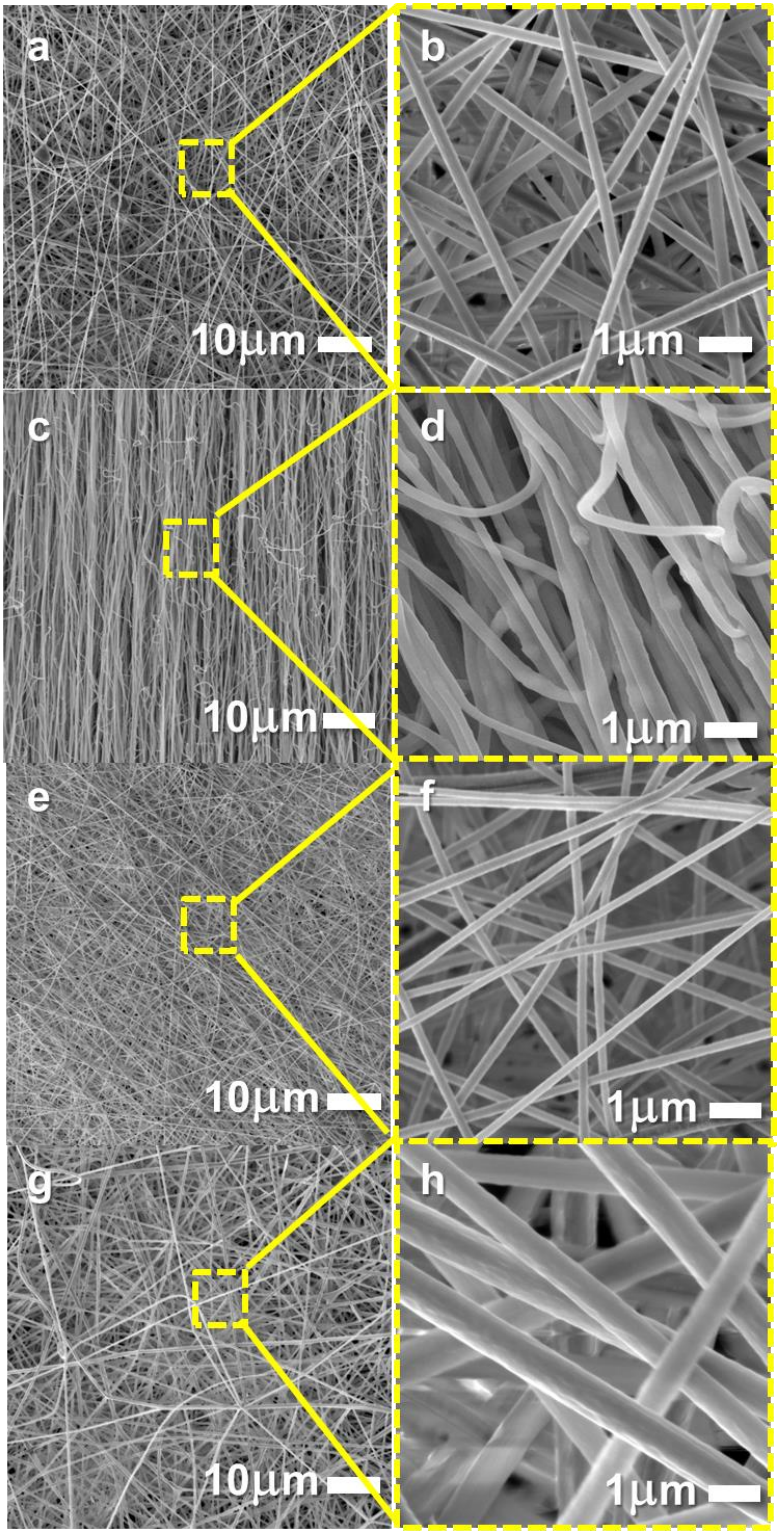

Figure 3-4. FE-SEM images of four different F-CNF samples chosen from previous studies. (a, c, e, g) are sample type 1, 2, 3, 4 in order. Each sample has its unique structural characteristic. (b, d, f, h) are the high resolution images of (a, c, e, g)

cathode type corresponds well with the experimental results.

The cyclability data of the lithium-air cells with the four sample cathodes chosen in Figure 3-6a, however, do not present significant difference from one another. The discharge capacities of all four samples at the second cycle encounter at around 4,000 mAh/g, and the discharge capacity of the sample type 3 with the smallest fiber dimension goes below all the others whereas that of the sample type 2 with the lowest discharge capacity at the first cycle starts to have the highest discharge capacity from the third cycle. However, the differences in specific capacity at each cycle are so small that one cannot be assured to say that it has the better or the best rechargeability over the others. Figure 3-6b is a typical voltage limit profile of sample cathode type 1 within a voltage window of 2.0 V to 4.8 V, presented in Figure 3-6a. The decrease from the 1^{st} discharge specific capacity to the 2^{nd} is more dramatic than any of the following results, and it keeps decreasing down to approximately 100 mAh/g from 8,000 mAh/g. All of the samples have a fixed carbon loading of 0.5 mg/cm^2 and the current density is set at 0.05 mA/cm^2 in all cases.

iii) EFFECT OF FUSION ON CELL PERFORMANCE AND ELECTROCHEMICAL PROPERTIES

On our way of searching for the reasoning behind the dramatic capacity loss over cycles, FE-SEM images were taken again with F-CNF sample type 1 cathode at each different state of pristine, discharge, and charge of the first deep cycle. (Figure 3-7) At fully discharged state it is notable that the discharge reaction products covered up all the surface of F-CNF cathode to a point where you do not see any trace of fiber morphologies on the air side as observed in Figure 3-7b whereas on the separator side in Figure 3-7c the fibers are clearly exposed with some of the

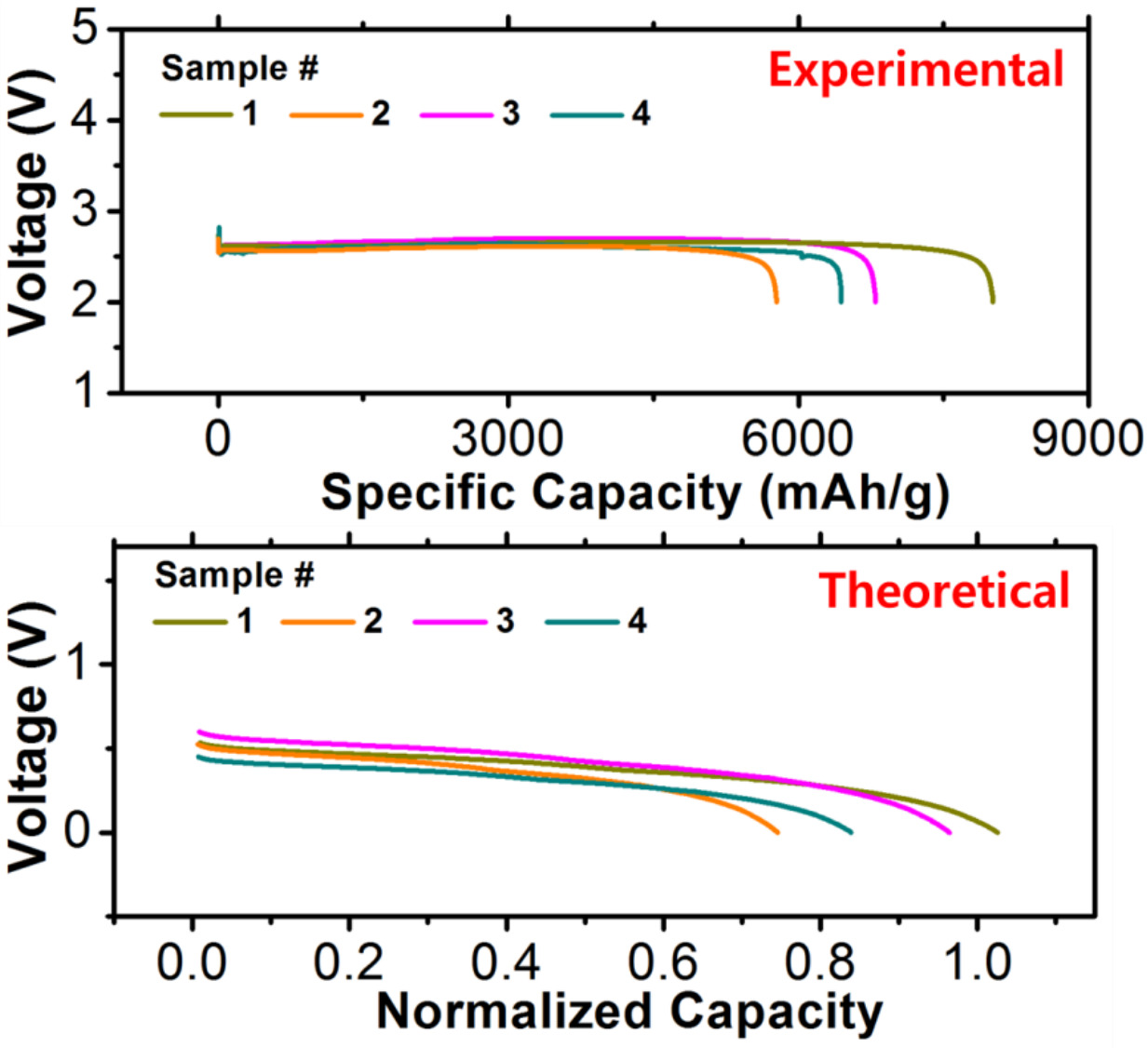

Figure 3-5. Voltage limit profiles (2.0V ~ 4.8V) of the discharge curves of the four samples chosen a) experimental, b) theoretical results using a diffusion limited model with respect to oxygen

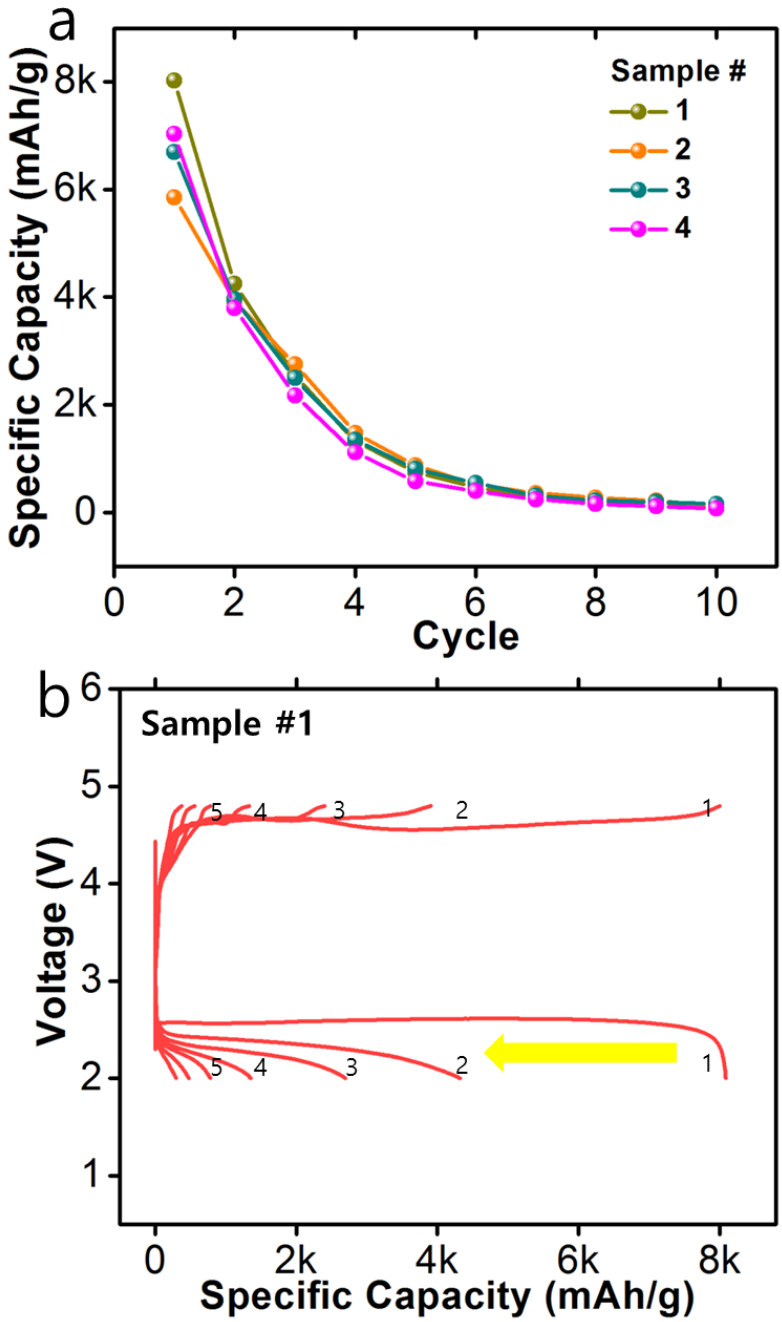

Figure 3-6. Voltage limit profiles (2.0V ~ 4.8V) with respect to (a) cycle life of the four samples chosen, and (b) specific capacity of the sample type 1. The amount of carbon loading is 0.5 mg/cm^2, and the cells operated at 0.05 mA/cm^2 in all cases.

reaction products filling the interfiber pores and adhering on the surface of the fibers. These images of F-CNF cathodes at discharged state indicate that the diffusion of oxygen is limited across the diffusion length or the thickness of the cathode that is soaked with liquid electrolyte. The oxygen concentration is apparently not high enough on the surface of the cathode at the separator side that the reaction products do not precipitate and cover up all the fibers. At charged state the F-CNF cathode on the air side shows its fibers again although the electrochemically irreversible byproducts or the reversible reaction products that have lost their electron pathways on the process of dissociation during charge are still remaining on the surface as shown in Figure 3-7d. The average fiber diameter of the charged F-CNF cathode on the air side is ~1.1 μm, which is almost five times as large as that of the pristine cathode. The thickness of the discharged F-CNF cathode has increased by 30% as shown in Figure 3-7f. Interestingly, the cross-sectional image of the charged F-CNF cathode in Figure 3-7g shows a number of delaminating crevices while the total thickness is similar with that of the discharged cathode. This result explains that on the process of over-accumulation and subsequent removal of the discharge reaction products the F-CNF cathode fails to maintain its structure generating discontinuities among the layers of fibers due to the lack of its mechanical properties such as rigidity or elasticity.

One way to improve the elasticity of PAN-derived F-CNF cathode is to lower the carbonization temperature from 900 ^{o}C down to 600 ^{o}C. However, heat treating at such a low temperature hardly eliminates a large amount of unnecessary functional groups or defects on the surface of fibers that are detrimental to the improvement of the electrical conductivity and charge transfer kinetics when applied to lithium-air battery cathode. On the other hand, there is a number of different ways to improve the mechanical rigidity of F-CNF cathode or the mechanical resistance

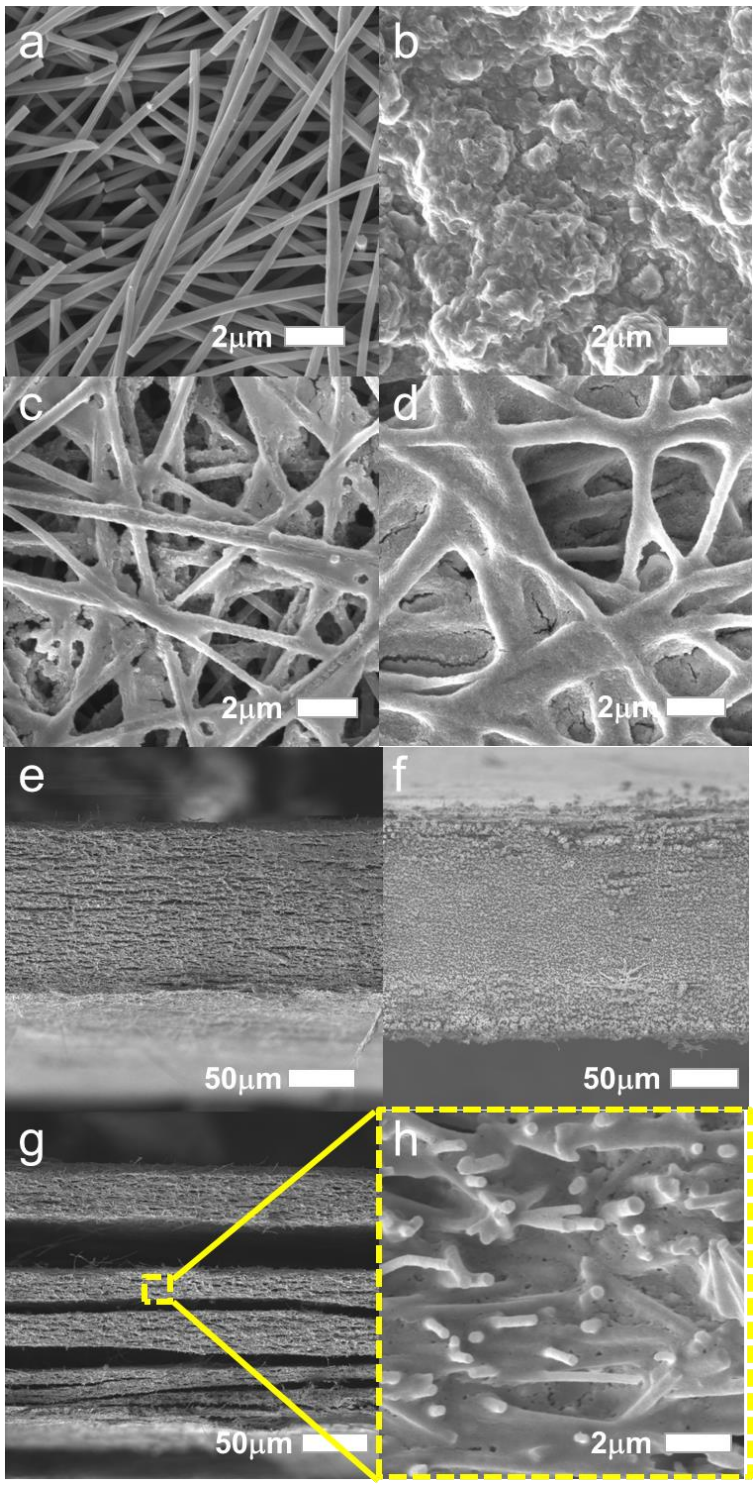

Figure 3-7. FE-SEM images of F-CNF sample type 1 at (a) pristine state, (b) discharged state on the air side, (c) on the separator side, (d) charged state on the air side, cross-sectional image of (e) pristine cathode, (f) fully discharged cathode, (g) charged cathode, and (h) high-resolution image of charged cathode

to its bending. One of the most common way is to use high concentration of polymer solution when electrospinning the fibers, so the fibers get thick enough to maintain its structure regardless of how much stress is imposed from inside the cathode structure due to the large amount of reaction product formation. However, as described and shown in Figure 3-5, the fiber mat with larger diameter and larger interfiber distance do not necessarily produce and store the larger amount of reaction products due to its reduced overall pore surface area. By imposing the mechanical pressure (50 psi) while thermally stabilizing the as-spun PAN fibers at 270 ^{o}C for one hour at a ramping rate of 10 ^{o}C/min, the fibers start fusing with each other as shown in Figure 3-8 and enhances the rigidity of F-CNF cathode to a great extent. This process named thermo-mechanical stabilization (TMS) not only improved the rigidity and the mechanical strength of the entire F-CNF cathode, but also alleviated the rapid loss of capacities over cycle when applied to the lithium-air battery cathode. Although the BET surface area of the fused F-CNT cathode (79 m^2/g) was expectedly lower than that of the original F-CNF cathode. (132 m^2/g), our previous experimental results with different F-CNF sample cathodes confirmed that the BET surface area of the air cathode is not the most important parameter to determine the electrochemical performance for lithium-air batteries.

Figure 3-9 summarizes the effect of TMS process in the fabrication of F-CNF cathodes on the electrochemical performance of the capacity retention of lithium-air battery cells over a number of discharge-charge cycles. It is noteworthy that the capacity retention has improved by 12% with the F-CNF cathode fused by TMS process as compared with the original F-CNF cathode. FE-SEM cross-sectional images before and after a full discharge-charge cycle are shown in Figure 3-9c and Figure 3-9d, respectively. The average thickness of the fused F-CNF cathode at

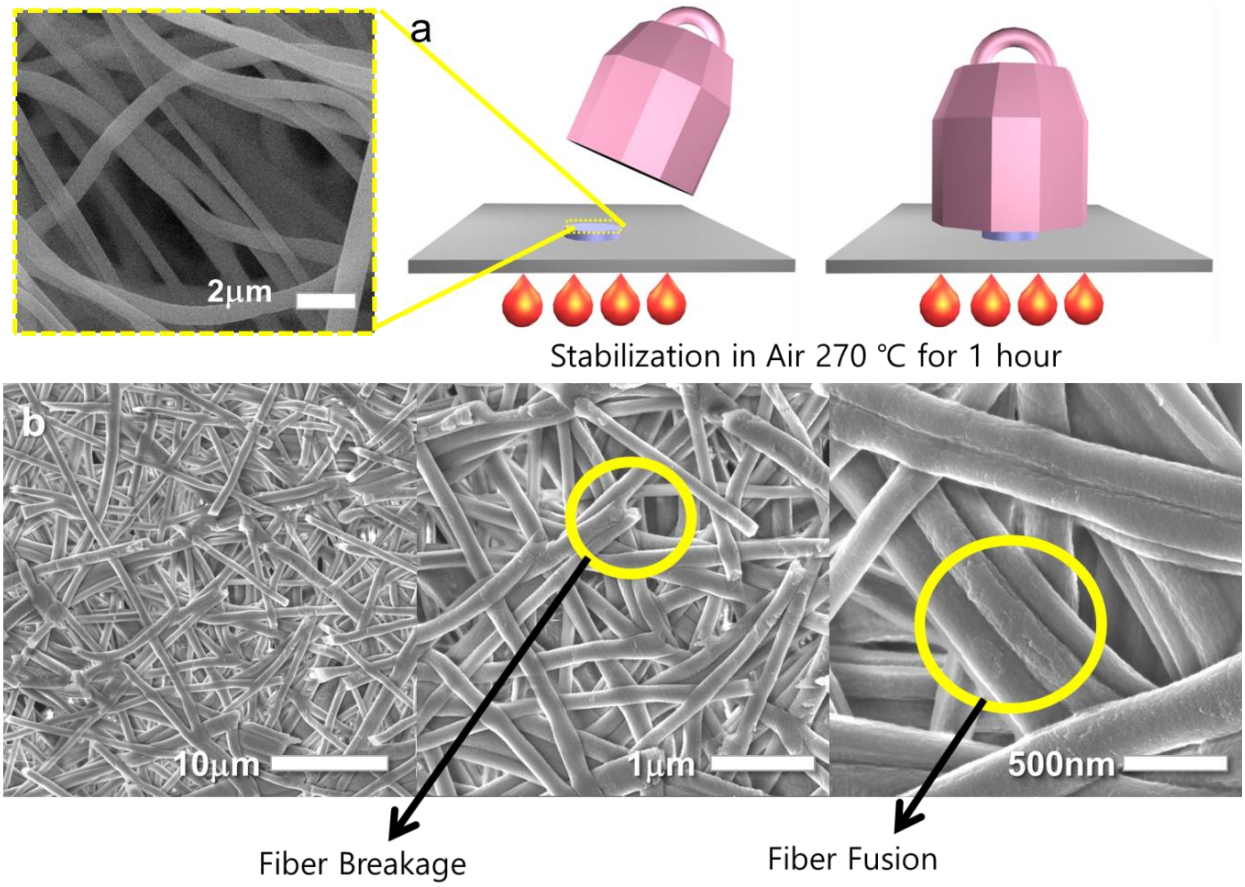

Figure 3-8. (a) Schematic illustration of giving mechanical pressure while stabilizing the as-spun PAN fibers at 270 ^{o}C under the air environment. (b) FE-SEM images of F-CNF fused fibers after the process of thermo-mechanical stabilization

charged state has increased by 3% as compared with the same cathode at pristine state, and this amount of increase in the fused F-CNF cathode is certainly not as significant as that of the original F-CNF cathode without TMS process because of its enhanced rigidity of the entire cathode structure. The lithium-air cells with both cathodes were operated at a current density of 0.3 mA/cm^2 and the total carbon loading for each case was fixed to 0.5 mg/cm^2.

Capillary flow porometry profiles in Figure 3-10a show the average interfiber pore diameters of fused and original F-CNF cathode before and after five full discharge-charge cycles. Original F-CNF cathode at its pristine state before cycle has the larger average interfiber pore diameter (0.62 μm) than the fused F-CNF cathode (0.48 μm) before cycle. Expectedly and similarly, the original F-CNF cathode at its charged state after five discharge-charge cycles show the larger average interfiber pore diameter (0.55 μm) than the fused F-CNF cathode (0.26 μm) after five cycles. Both fused and original F-CNF cathodes show decrease in the average interfiber pore diameter after five cycles presumably due to the remaining reaction products filling up the pores that had failed to converse back to the lithium ions and evolve oxygen gas. The BJH pore size distributions and its corresponding adsorption isotherm plots of the fused and original F-CNF cathodes before and after five cycles were also presented in Figure 3-10c. As shown in both plots, the original F-CNF cathode at its pristine state before cycle has the larger quantity of nitrogen absorbed on the surface of pores within the range of 0 to 50 nm in diameter as compared with the fused F-CNF cathode at its pristine state before cycle. On the other hand, unlike capillary flow porometry data, the nitrogen isotherm curves of the fused and original F-CNF cathodes after five cycles show very similar to each other. This result indicates that regardless of the types of F-CNF cathodes with or without the TMS process, the pores of the F-CNF cathodes that are within the

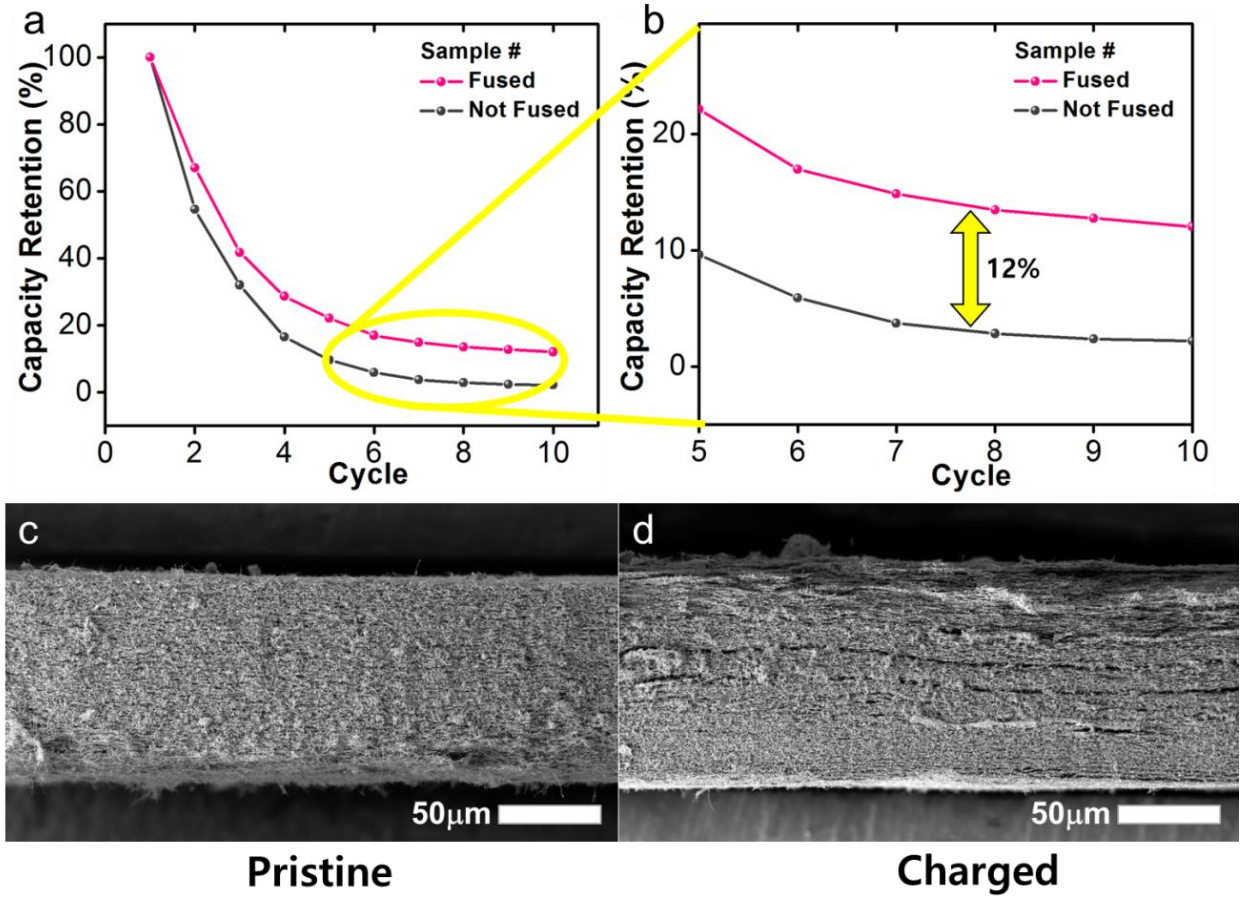

Figure 3-9. (a, b) Electrochemical performance of cycle retention over cycle number of F-CNF cathodes with and without the thermo-mechanical stabilization. The amount of total carbon loading is 0.5 mg/cm^2, and the current density is 0.3 mA/cm^2. FE-SEM cross-sectional images of fused F-CNF cathode at (c) pristine and (d) charged states.

size range of 0 to 50 nm are almost completely filled with remaining reaction products after five full discharge-charge cycles.

Nyquist plots of EIS spectra results for fused and original F-CNF cathodes before and after five discharge-charge cycles are shown in Figure 3-10b. The difference in the numbers of the onsets of the curves for the F-CNF cathodes before and after cycles represents the difference in the electrolyte resistance, which corresponds to the level of electrolyte corrosion or decomposition. The electrolyte in the complete lithium-air battery cells is very vulnerable to its decomposition during a number of operating cycles. The shift of the onset of the Nyquist plots tells how much the electrolyte is decomposed during cell operation. The shifts of the onsets of the Nyquist plots for both fused and original F-CNF cathodes before and after cycles are very similar in numbers, which indicate that the change in the mechanical properties due to the TMS process hardly affects the level of electrolyte decomposition during the cell operation. The width of the semicircles of the Nyquist plots represents the charge transfer resistance of the complete lithium-air battery cell, which includes the resistance of solid electrolyte interfaces, the resistance of electrodes, and the resistance of interface between electrodes and current collectors. The widths of the semicircles of the Nyquist plots for the fused and original F-CNF cathodes at pristine state before cycle are very similar (~134 Ω) whereas the width of the semicircle for the fused F-CNF cathode after cycles (~211 Ω) is a lot smaller than that for the original cathode after cycles (~338 Ω). The difference shown in the charge transfer resistance of the lithium-air cells with the fused and original F-CNF cathodes after cycles is noteworthy because this serves as a supporting proof of fused F-CNF cathodes having improved charge transfer kinetics over cycles, which lead to the enhancement of the cycle retention as shown in Figure 3-9a. Figure 3-10d presents the electrical

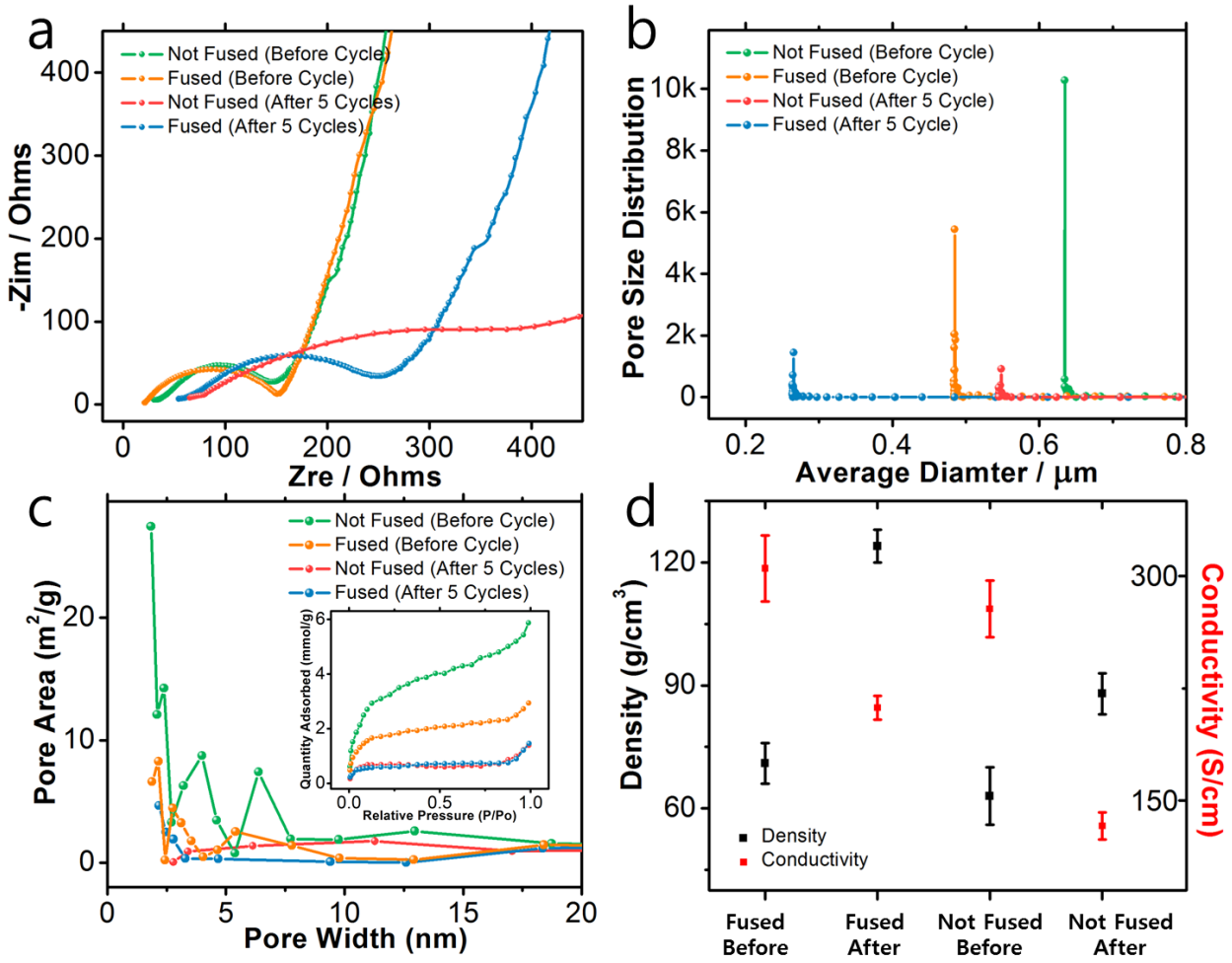

Figure 3-10. (a) Capillary flow porometry profiles, (b) EIS spectra, (c) BJH pore size distribution with N_2 adsorption isotherm plot (inlet), and (d) electrical conductivity and volumetric mass density of original and fused F-CNF cathodes before and after running five full discharge-charge cycles.

conductivity and volumetric mass density of both fused and original F-CNF cathodes before and after cycles. At a given specific weight of 0.5 mg/cm^2 the volumetric density of the fused F-CNF cathode before cycles is higher than that of the original cathode before cycles, and the density of the cathodes after cycles is always higher than that of the cathodes at pristine states before cycles. This is again attributed to the remaining reaction products filling up the pores of cathodes after discharge-charge cycles. The amount of increase in volumetric density of the fused F-CNF cathode before and after cycles is much greater than the amount of increase in the original F-CNF cathode because as shown in Figure 3-7g the original cathode suffers from severe structural disorder and delamination during cycles which contribute to the increase in the average interfiber pore diameter and decrease in the overall volumetric mass density. The electrical conductivity of the fused F-CNF cathode at its pristine state is slightly higher than the original pristine F-CNF cathode presumably due to the enhanced interconnectivity among the fibers fused by the TMS process. The cathodes after cycles show decrease in the electrical conductivity from the cathode before cycles in general, but the fused F-CNF cathode shows the higher electrical conductivity than the original cathode after cycles, which is commensurate with the EIS spectra results plotted in Figure 3-10b.

Combining what we have learned in the previous and current studies on the structural aspect of lithium-air battery cathode, an attempt to add a different type of carbon such as Super P (carbon black) or RGO in the fused F-CNF cathode by a layer-by-layer assembly method was made as pictured in Figure 3-11. Figure 3-11a is the top view FE-SEM image of RGO layer and Figure 3-11b is that of the fused F-CNF layer. Figure 3-11c and Figure 3-11d are low and high resolution cross-sectional images of a sandwich-stacked RGO-CNF cathode whereas Figure 3-11g and

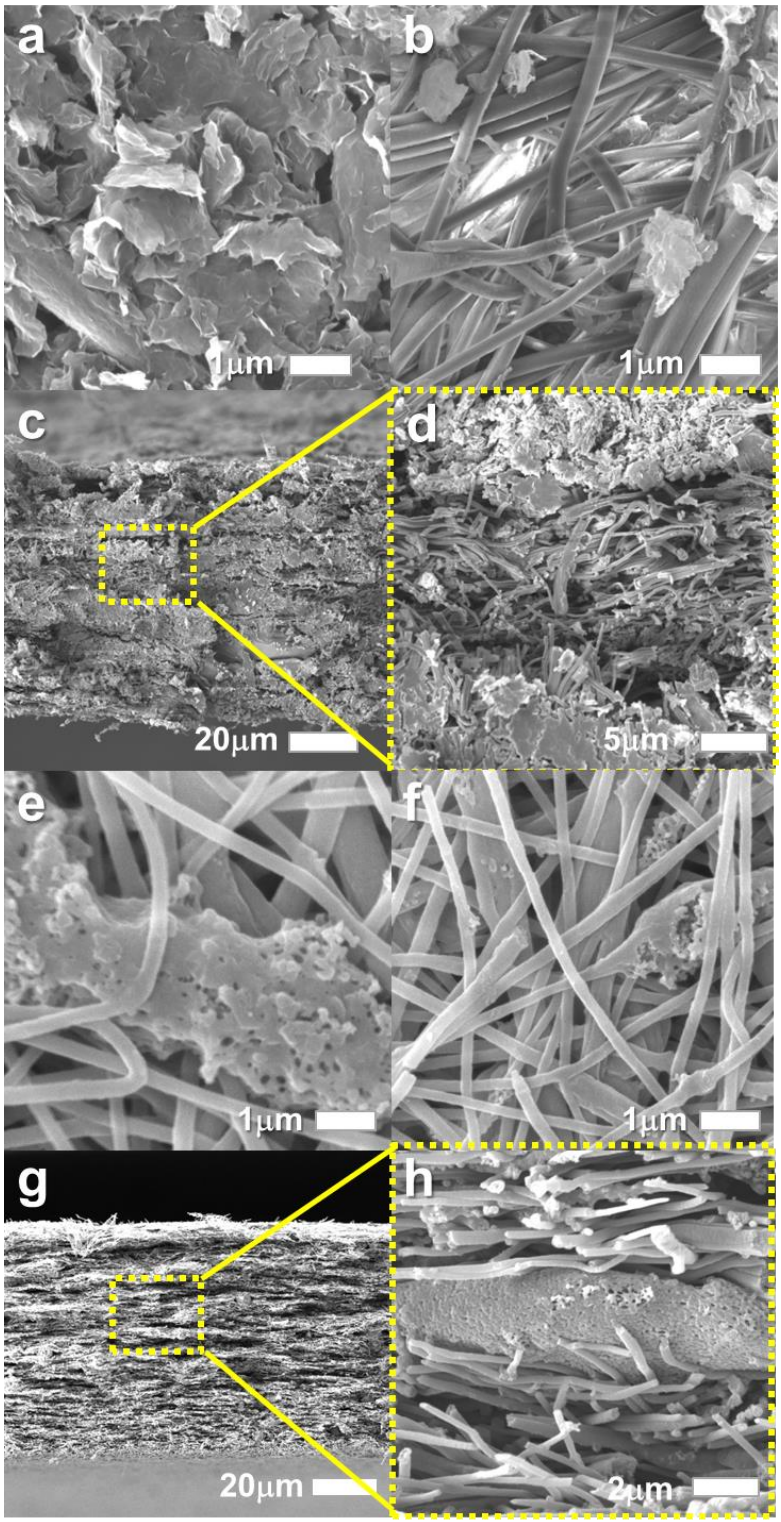

Figure 3-11. FE-SEM images of sandwich-stacked and fused F-CNF cathodes with (a, b, c, d) RGO and (e, f, g, h) Super P. Cross-sectional image of (c) RGO-F-CNF, (d) high resolution of (c) and (g) Super P-F-CNF, (h) high resolution of (g).

Figure 3-11h show those of a sandwich-stacked Super P-CNF cathode. As observed in Figure 3-11d and Figure 3-11h, the average thickness of each RGO layer is approximately 7 μm whereas that of each Super P layeris 2 μm. Unfortunately, no matter how carefully and consistently the additional carbon particle layers are laid with the layers of PAN fibers, while thermo-mechanically stabilizing and carbonizing the entire layers of cathode, it was inevitable to see the agglomeration of the added carbon particles and the inconsistencies in the thickness of each layer of carbons. However, it was still very clearly seen that the thickness of RGO layers is much larger than that of the Super P layers, and it is highly expected that the thicker the added carbonlayers combined with the fused F-CNF layers get, the effect of fusion of fibers as demonstrated in both electrochemical performance and characterization in Figure 3-9 and Figure 3-10 will be dampened as shown in Figure 3-12.

In terms of the initial or the discharge specific capacities of the first deep cycle, the fused RGO-CNF cathode earned the highest of 6839 mAh/g whereas the fused F-CNF cathode without any addition of carbon particles showed the lowest of 3201 mAh/g. However, regarding the capacity retention, the fused Super P-CNF cathode showed the highest of 22% at tenth cycle whereas the original F-CNF cathode showed the lowest of 2% at tenth cycle. It is worth noting that the capacity retention of the fused RGO-CNF cathode is less than that of the fused Super P-CNF cathode by more than 10% whereas the capacity retentions of both the single layer RGO and Super P cathodes do not present much difference (3%) from each other. The capacity limit profiles in Figure 3-12b show the cycle life of the fused and original F-CNF cathodes with or without the addition of RGO or Super P at a specific capacity limited to 1,000 mAh/g in the order of the capacity retention in the voltage limit profiles in Figure 3-12a. The fused Super P-

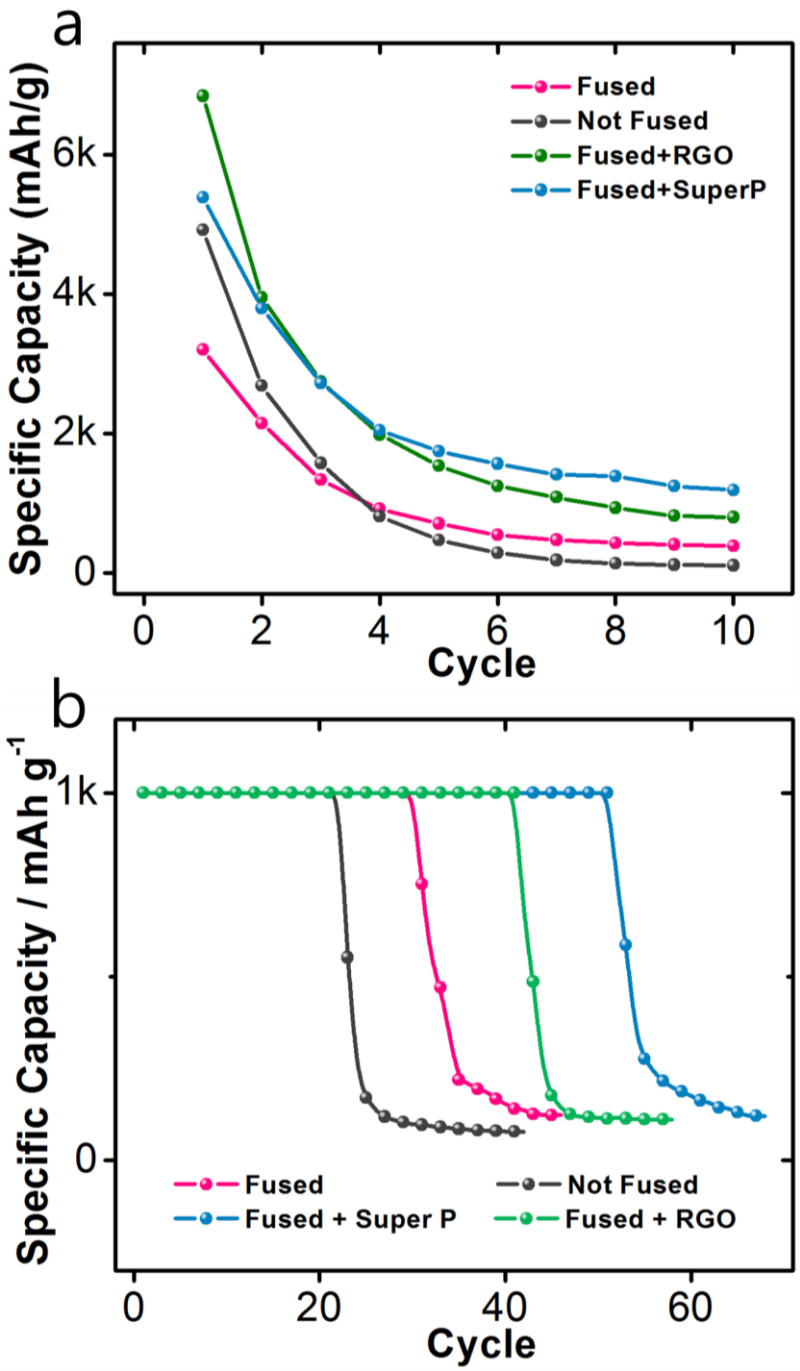

Figure 3-12. Electrochemical performance of (a) voltage limit (2.0 V ~ 4.8 V) and (b) capacity limit (1,000 mAh/g) discharge specific capacity profiles over cycle life of the original or fused F-CNF cathodes with and without the addition of RGO or Super P layers. The total carbon loading is 0.5 mg/cm^2 and the current density is 0.3 mA/cm^2 in all cases.

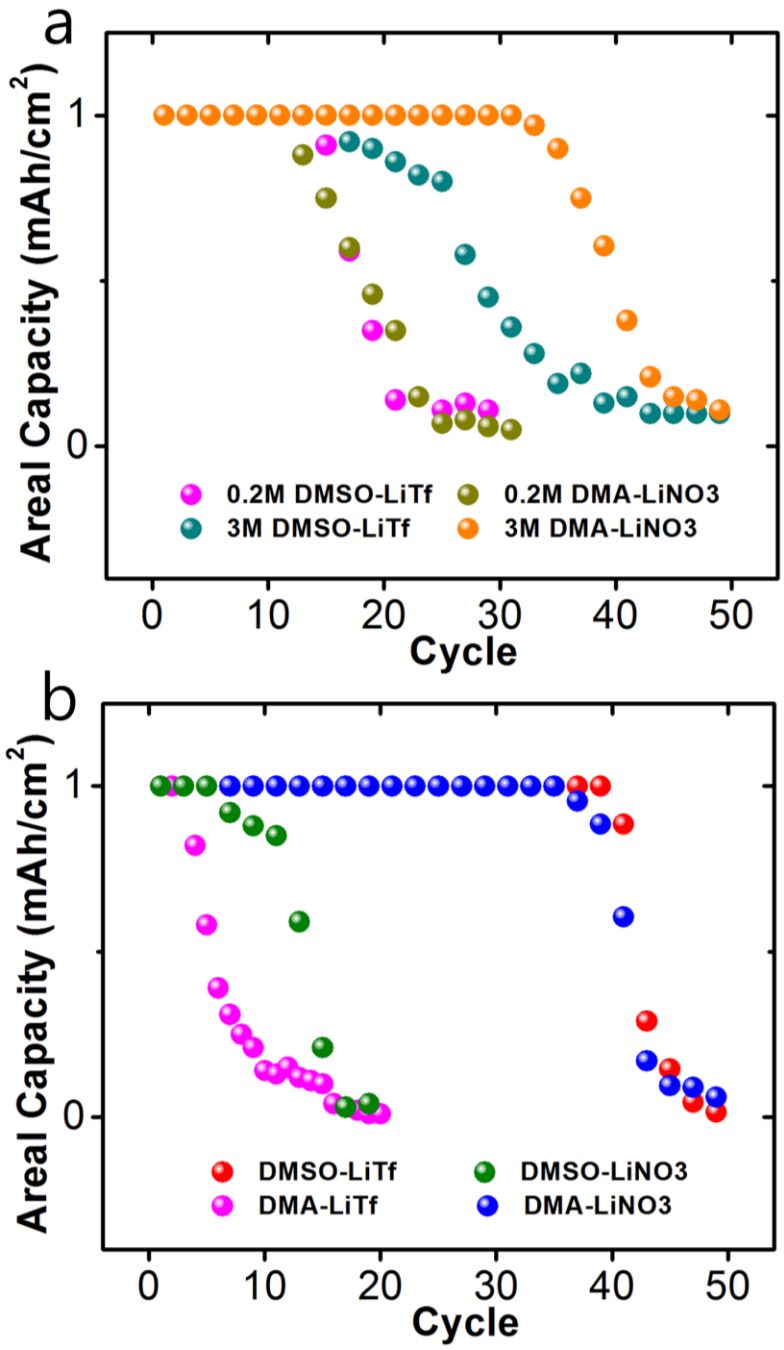

Figure 3-13. Cycle performance of F-CNF cathodes in lithium-air battery cells using DMSO and DMA as electrolyte solvents and LiTf and $LiNO_3$ as electrolyte salts (a) with different concentration of salts dissolved in the solvents and (b) with different pairs of electrolyte solvents and salts with 1 M concentration. All cells were operated under ambient air with 50% relative humidity in the voltage range of 2.0 to 4.8 V versus Li/Li^+ at a current density of 0.3 mA/cm^2.

CNF cathode with the highest capacity retention showed the longest cycle life of 51 cycles with the specific capacity limited to 1,000 mAh/g at a current density of 0.3 mA/cm^2 whereas the original F-CNF cathode with the lowest capacity retention produced the smallest cycle number of 22 cycles under the same condition. These results along with the FE-SEM images in Figure 3-11 indicate that the addition of Super P hardly affected the process of making fused fibers and brought a synergistic effect on the electrochemical properties of the entire cathode whereas the RGO particles were bulkier and easier to agglomerate that their addition mitigated the fusion of fibers and caused a significant loss in the capacity retention.

Electrolyte chemistry is another indispensable research area in the field of lithium-air batteries as the electrolyte decomposition is known to be the major cause of rapid loss in capacities over cycles. It has always been considered important to find an optimum solution that is less or non-reactive towards superoxide radicals or reaction products and less volatile than DME under ambient environment. Our preliminary results shown in Figure 3-13 further demonstrate significance in the compatibility between electrolyte solvent and salts and present cycle performance data simply by controlling the electrolyte salt concentration or the selection of electrolyte solvent and salt pair. Dimethylacetamide (DMA) coupled with lithium nitrate ($LiNO_3$) and dimethylsulfoxide (DMSO) with lithium triflate (LiTf) performed the best achieving over 40 cycles with the limited capacity of 1 mAh/cm^2 at a current density of 0.3 mA/cm^2 under the ambient air environment, using the original F-CNF cathode whereas DMA with LiTf and DMSO with $LiNO_3$ achieved less than 10 cycles respectively under the same condition. Profound and fundamental study in the electrolyte compatibility is required to enhance the rechargeability of lithium-air batteries.

In summary, the pore structure of the F-CNF cathode for the lithium-air batteries can be designed in a way to facilitate the oxygen diffusion and to maximize the discharge specific capacity of the first operating cycle. However, controlling the interfiber pore size or the fiber diameter with the electrospinning parameters seemed not enough to significantly improve the rechargeability. Introducing the TMS process during the fabrication of the F-CNF cathodes and the addition of other types of carbon such as Super P or RGO provided the ultimate solution of the rechargeable lithium-air battery cathode with the elimination of unnecessary weights for polymeric binders or adhesives and metal current collector mesh foils.

CHAPTER IV

LITHIUM-SULFUR BATTERY CATHODE STRUCTURE

SULFUR NANOFIBER

INTRODUCTION

Lithium-sulfur battery has exceptionally high theoretical specific capacity of 1,675 mAh/g. Its technology and the abundance of sulfur are recognized attractive to the various people in the industry. [59-62] The chemistry in the lithium-sulfur battery technology brings each sulfur atom to host two lithium ions to form lithium sulfide (Li_2S) whereas conventional lithium-ion batteries accommodate only 0.5 lithium ions per carbon atom. The discharge reaction follows a sequence of following: $S_8 \rightarrow Li_2S_8 \rightarrow Li_2S_6 \rightarrow Li_2S_4 \rightarrow Li_2S_3 \rightarrow Li_2S$, and the reverse of it during charge. [63-65] Sulfur has conductivity of 5×10^{-30} S/cm at 25 ℃, which requires a carbon coating to provide an effective electron pathway and structural stability. [66-68] A few but critical obstacles still left to be overcome in the industry, such as capacity loss due to intermediate polysulfide (Li_2S_8, Li_2S_6, Li_2S_4, Li_2S_3) dissolution into liquid electrolyte [69-79] and volume expansion of sulfur during lithiation process (nearly 80% of the original volume of sulfur). [80-88] The intermediate polysulfides formed during discharge process dissolve and react to form insoluble lithium sulfides on the surface of lithium metal at the anode during charge. This so-called shuttle effect slowly removes the active sulfur in the cathode and causes rapid degradation of the cell. Moreover, the volume expansion of sulfur gives stress on the cathode and reduces the contact

between the carbon coating and the sulfur and hinders the diffusion of lithium ions on the carbon surface. The uses of many different types of protective layers on the lithium metal anode are reported to alleviate the cell degradation by preventing the reaction and precipitation of the intermediate polysulfides on the anode. [89-93] Seh, *et al.* [82] invented and proposed sulfur-TiO_2 yolk-shell type nanoparticles with internal void spaces to mitigate the effect of volume expansion of sulfur and to minimize the dissolution of intermediate polysulfides and applied successfully to lithium-sulfur battery cathodes with significant improvement in the capacity retention. However, the use of heavy weight ceramic instead of carbon lowers the specific gravimetric capacity and the process of nanoparticle synthesis is not trivial to reduce the cost of materials as compared to conventional lithium-ion batteries. Interestingly, Xin, *et al.* [94] implies that the cyclic octatomic molecules of sulfur will not be able to completely avoid its loss within the cathode structure and will cause the rapid fading of capacity. They show and claim that the metastable small sulfur molecules of $S_{2\text{-}4}$ instead of S_8 completely avoid the unfavorable transition to soluble intermediate polysulfides. The synthesis of smaller sulfur molecules requires the stress of confinement within conductive carbon matrix. Here, we propose a facile fabrication of cathode using electrospun sulfur-containing copolymer, poly(sulfur-random-(1,3-diisopropenylbenzene)) or poly(S-r-DIB), nanofiber with interfiber void space to accommodate the volume expansion of lithiated sulfur. The unique stretched-out chain structure of sulfur copolymer converted from the original cyclic octatomic sulfur molecules and confined within the polymer matrix is proven to be conducive to minimizing the polysulfide dissolution, [95] which results in the improvement of the capacity retention over cycles. Due to the ductile and sticky nature of poly(S-r-DIB), this cathode system offers a direct deposit of sulfur/conductive carbon materials on the current collector which can potentially be used in a flexible Li-S battery system.

EXPERIMENTAL METHODS

i) SYNTHESIS OF POLY(S-r-DIB) COPOLYMER

Sulfur powder purchased from Sigma-Aldrich and kept in room temperature and 1,3-diisopropenylbenzene (DIB) which is a transparent liquid stored under 5 ^{o}C in the refrigerator are mixed well in a weight ratio of 1:1 in a 20 mL glass vial that has cap with PTFE liner and heated at 185 ^{o}C on a hot plate for 15 minutes. As the sulfur starts to melt and become a liquid sulfur diradical, the cyclic octatmoic ring chain breaks and forms a linear molecule waiting for DIB to hold them still so that they would not go back to the original ring structure. During the synthesis, the color of the mix changes from yellow to dark yellow, dark yellow to light red, and light red to dark red over time. After cooling the as-synthesized poly(S-r-DIB) copolymer down to a room temperature, high purity chloroform was added directly into the vial, and the vial is heated again at 205 ^{o}C on a hot plate until the copolymer is completely dissolved into the solvent. This process takes about 30 ~ 45 minutes depending on the amount of copolymer synthesized in the previous step. Poly(ethylene oxide) (PEO) purchased from Sigma-Aldrich with average molecular weight of ~300,000 and/or Ketjen Black (KB) (EC-600JD) carbon black powder were added to the poly(S-r-DIB) copolymer and chloroform solution and stirred overnight at high intensity. The weight ratio of poly(S-r-DIB): KB: PEO is 85: 10: 5 in all cases.

ii) CATHODE FABRICATION AND CELL ASSEMBLY

5 mL disposable plastic syringe is filled with the poly(S-r-DIB) copolymer solution. The tip of the syringe is connected with a coaxial needle (18 gauge inside, 14 gauge outside). Air flows on the shell of the needle at a fixed pressure of 10 psi, and the solution flows in the core of the

needle at a flow rate of 0.01 mL/min. The 20 V direct current (DC) is applied to the needle and the aluminum foil current collector. When the solution is charged through the needle, the electrostatic repulsion counteracts the surface tension and stretches the droplet to form a cone shape. The as-spun poly(S-r-DIB) nanofiber with the addition of KB is collected on the aluminum foil, disc-cut 1.56 cm in diameter and further coated with RGO slurry solution with 20 wt.% of Nafion as a binder by spin coater at 1,000 rpm for 10 seconds. The amount of RGO particles coated on top of the electrospun materials is carefully measured so that it matches with the amount of KB incorporated within the fibers. The overall weight ratio of poly(S-r-DIB): RGO: KB: PEO is 75: 10: 10: 5. The assembly of the battery starts with placing the lithium disc foil (MTI Corporation) 1.56 cm in diameter on the bottom part of the 2032 type coin cell kept in an argon filled glove box (< 0.1 ppm, O_2 and H_2O). Celgard separator with 1.91 cm in diameter of trilayer polypropylene-polyethylene-poly propylene (PP-PE-PP) membrane is placed next on top of the lithium foil, followed by 100 ul of electrolyte solution of 1 M lithium bis(trifluoromethylsulphonyl)imide (LiTFSI) in 1,2-dimethoxyethane (DME) and 1,3- dioxolane (DOL) in the volume ratio of 1:1 with 0.5 M lithium nitrate ($LiNO_3$) dropped onto the separator. The as-spun fabricated poly(S-r-DIB) nanofiber cathode is finally placed on top of the electrolyte-wet separator followed by a stainless steel spacer, a spring, and the top part of the coin cell covering all the cell components.

iii) ELECTROCHEMICAL METHODS AND INSTRUMENTATION

The EIS spectra was obtained with a PARSTAT 4000 electrochemical workstation (Princeton Applied Research) within a frequency range of 10^5 to 10^{-2} Hz using 5 mV (RMS) input voltage amplitude. The galvanostatic tests were performed under a cut-off voltage window from 1.6 V to

2.8 V versus Li/Li+ in the voltage limit profile by using BST8-MA (MTI Corporation) multi-channel battery testing system. The discharge-charge performance was controlled by Neware BTS system and evaluated at a constant current density of 0.2 C, which is equivalent to 335 mA/g. CV was conducted with the same workstation as EIS spectra was obtained (PARSTAT 4000) at a scan rate of 0.1 mV/s in the voltage range of 1.6 to 2.8 V versus Li/Li^{+}. The morphologies of the electrospun poly(S-r-DIB) copolymer nanofiber were observed by FE-SEM equipped with EDS (Tescan Mira3).

RESULTS AND DISCUSSION

i) SYNTHESIS OF POLY(S-r-DIB)

As described in Figure 4-1, the synthesis of poly(S-r-DIB) starts with preparing sublimed sulfur powder with cyclic octatomic molecules, and 1,3-diisopropenyl-benzene (DIB). The sulfur powder and DIB with a weight ratio of 1:1 are mixed well in a 20 mL glass vial with a cap that has PTFE liner and heat treated at 185 ^{o}C on a hot plate for 15 minutes. As the sulfur starts to melt and become a liquid sulfur diradical, the cyclic octatmoic ring chain breaks and forms a linear molecule waiting for DIB to hold them still so that they would not go back to the original ring structure. [95] During the synthesis, the color of the mix changes from yellow to dark yellow, dark yellow to light red, and light red to dark red over time, and the final product of poly(S-r-DIB) copolymer possess the polymeric properties such as transparency, elongation, and elasticity as demonstrated in Figure 4-1b.

The elongation and elasticity of as-synthesized copolymer are two significant prerequisite properties in order for it to be electrospun and form the fiber morphologies. The high aspect ratio of the electrospun poly(S-r-DIB) fibers is beneficial in terms of storing the reaction products without deforming the structure especially when applied to the lithium-sulfur battery cathodes because the structural disorder due to the 80% volume expansion of the lithiated sulfur is known to be one of the major cause of the cell degradation of the lithium-sulfur battery as schematically described in Figure 4-2.

ii) DIRECT DEPOSIT OF POLY(S-r-DIB) NANOFIBER

On the process of making the electrospun poly(S-r-DIB) copolymer nanofiber, the as-synthesized

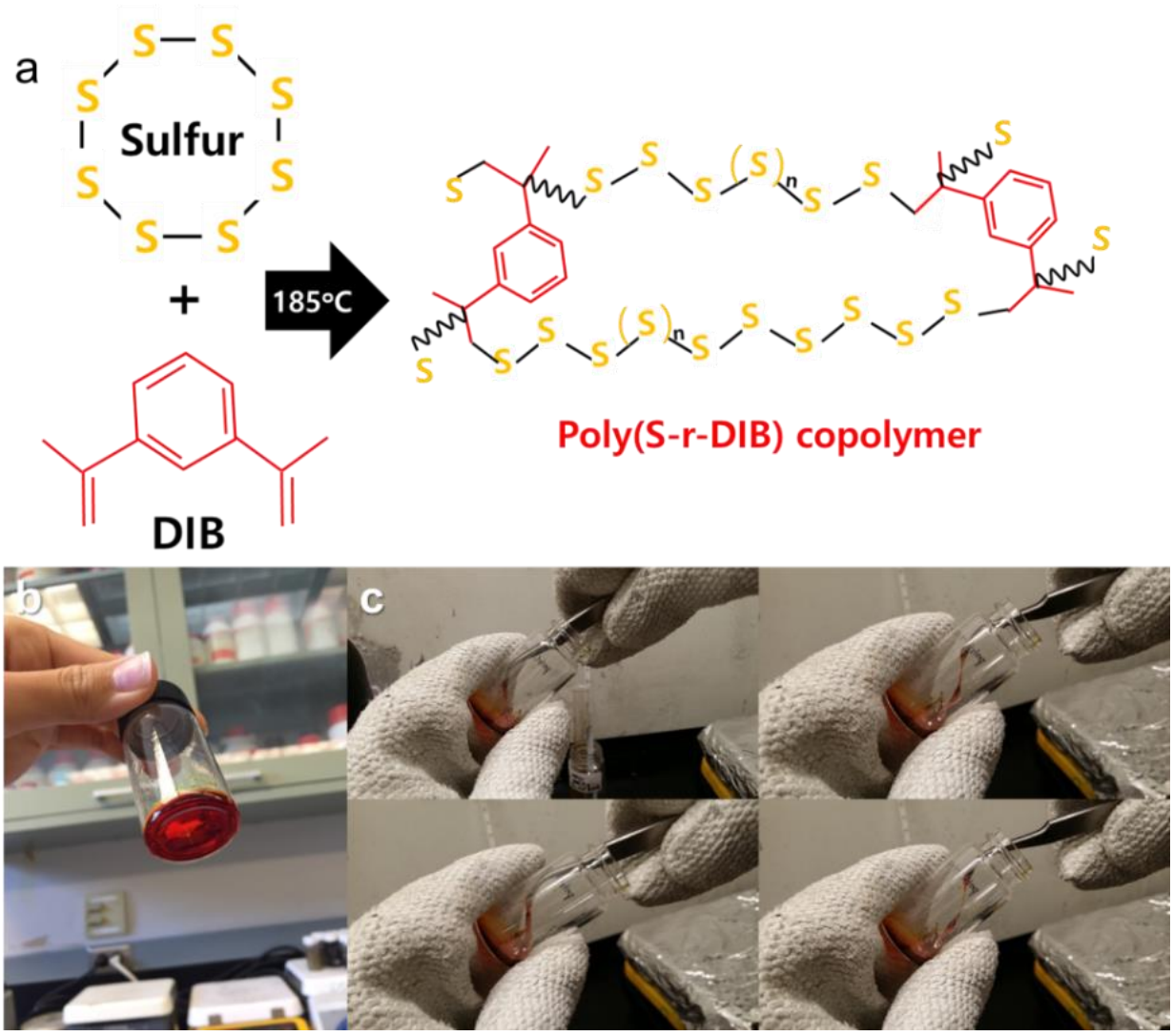

Figure 4-1. (a) Synthesis of poly(S-r-DIB) copolymer, (b) Photo image of poly(S-r-DIB) copolymer in a 20 mL vial and demonstration of its elongation property

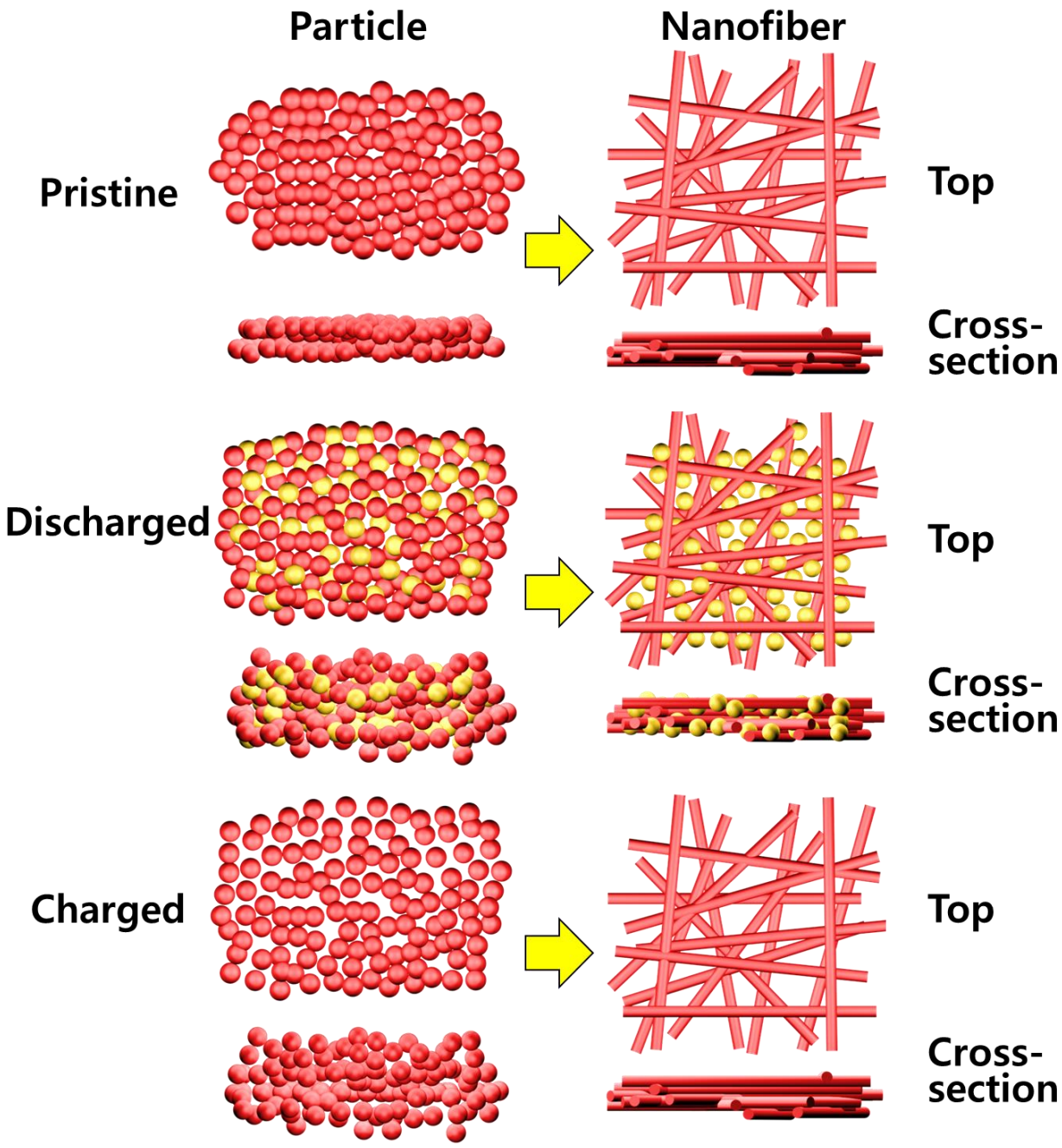

Figure 4-2. Schematic illustrations of top and cross-sectional views of (a) poly(S-r-DIB) copolymer nanofiber, (b) pure sulfur particles applied as lithium-sulfur battery cathode at pristine, discharged and charged state.

poly(S-r-DIB) is dissolved in the high purity (>99%) chloroform at 205 ^{o}C until the copolymer is completely dissolved into the solvent. Poly(ethylene oxide) (PEO) and/or Ketjen Black (KB) powder were added to the solution and stirred overnight. Figure 4-3a describes the air-assisted electrospinning process for fabricating poly(S-r-DIB) nanofiber electrodes. The introduction of air into the outer shell of the electrospinning co-axial needle at a fixed pressure of 10 psi makes the production rate faster by almost an order of magnitude. When the solution is charged through the needle, the electrostatic repulsion counteracts the surface tension and stretches the droplet to form a cone shape. The polymeric substance dissolved in the droplet is stretched at the same time and sticks to the aluminum foil current collector as the pump slowly pushes the solution out from the syringe. The morphologies as-spun poly(S-r-DIB): PEO nanofiber with and without 10 wt% KB are shown with FE-SEM images in Figure 4-3b to Figure 4-3e with different magnification. The average fiber diameter is measured to be 192 nm. A single poly(S-r-DIB) fiber is detected as shown in Figure 4-4 and further analyzed with EDS elemental mapping of sulfur, carbon, fluorine, nitrogen, and oxygen. The sulfur and carbon derived from DIB are detected with a strong intensity along and throughout the entire regions of the fiber whereas no trace of fluorine, nitrogen, and oxygen are identified along the fiber through EDS mapping technique. These results are significantly noteworthy, especially in the discovery of the electrospinnability of the poly(S-r-DIB) copolymer that no one else has achieved or attempted so far to our knowledge. After directly depositing electrospun poly(S-r-DIB) copolymer nanofiber with the addition of KB onto a sheet of aluminum foil current collector, it is disc-cut 1.56 cm in diameter and further coated with RGO slurry solution with Nafion as a binder by spin coater at 1,000 rpm for 10 seconds. The amount of RGO coated on top of the electrospun materials is carefully measured so

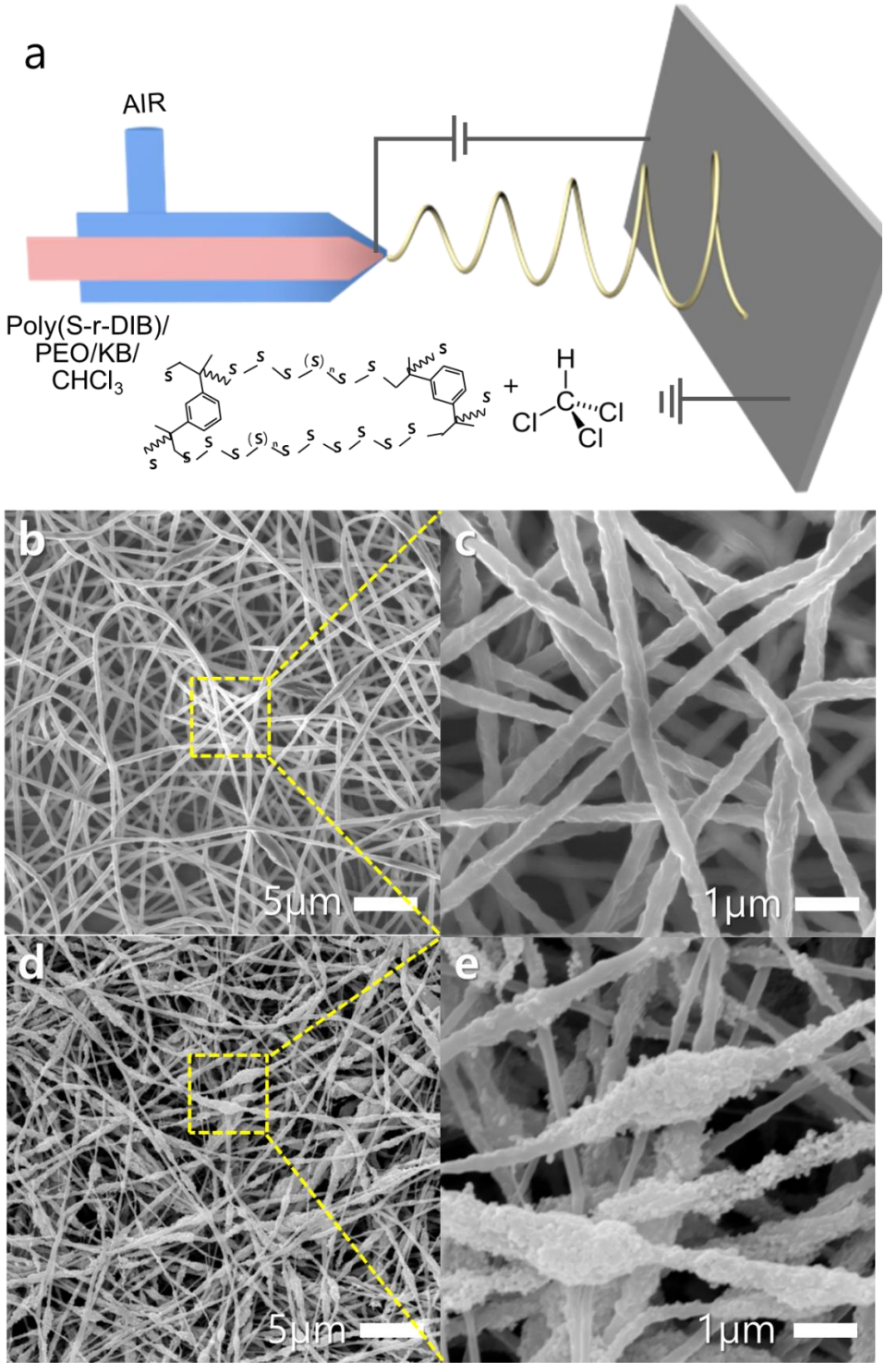

Figure 4-3. (a) Schematic illustration of air-assisted electrospinning of poly(S-r-DIB) copolymer with KB dispersed in chloroform. FE-SEM images of (b, c) electrospun poly(S-r-DIB) nanofiber, and (d, e) poly(S-r-DIB) nanofiber with the addition of KB.

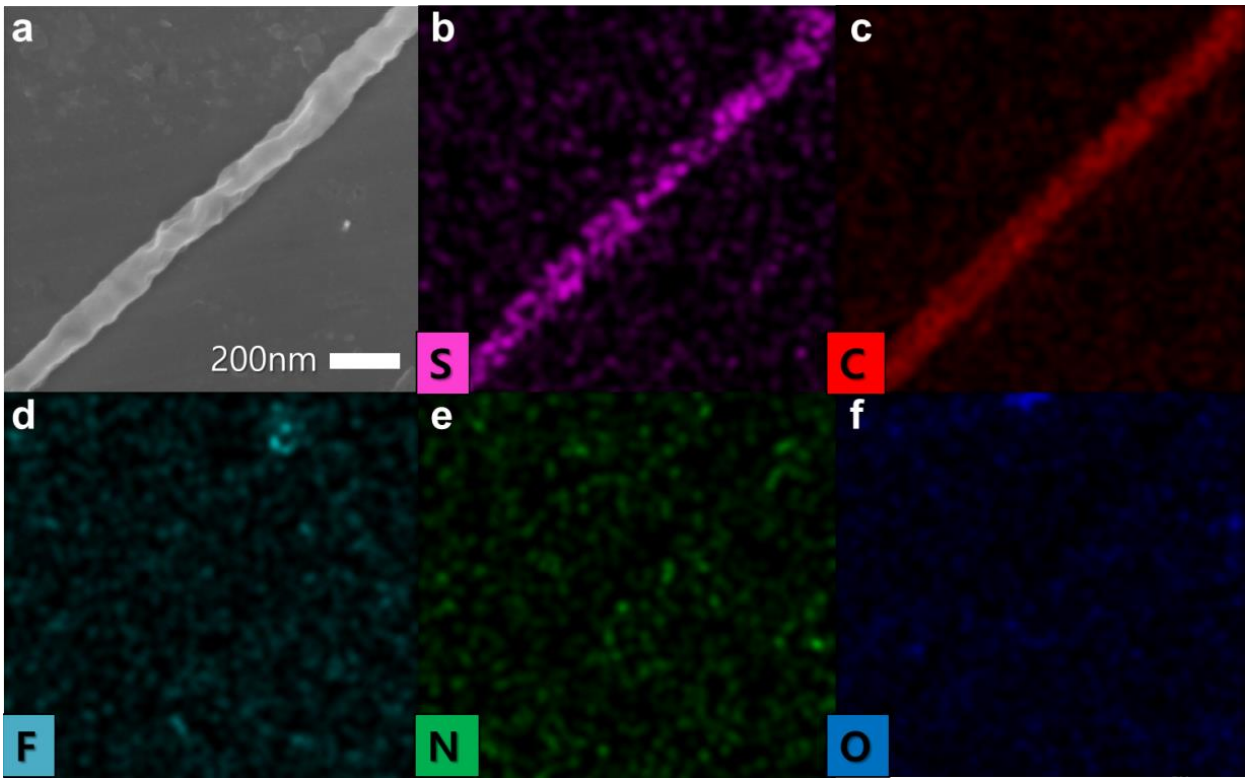

Figure 4-4. (a) FE-SEM image and EDS element detection of (b) sulfur, (c) carbon, (d) fluorine, (e) nitrogen, (f) oxygen, of a single electrospun poly(S-r-DIB) nanofiber

that it matches with the amount of KB incorporated with the fibers. The overall weight ratio of poly(S-r-DIB): RGO: KB: PEO solution is 75: 10: 10: 5. The final product of flexible electrode is shown with a digital photo image in the inset of Figure 4-5a. Top view FE-SEM image of RGO film on top of the electrospun poly(S-r-DIB) copolymer nanofiber is shown in Figure 4-5b. The main purpose of this RGO thin film coating is to minimize the intermediate polysulfide dissolution and to enhance the charge transfer kinetics of the complete lithium-sulfur battery cell. As shown in Figure 4-5b, the RGO particles are tightly adhered by Nafion, and this film as an interlayer is known to effectively block the lithium polysulfides to dissolve into the electrolyte and diffuse onto the other side of the cell, lithium metal anode.

iii) ELECTROCHEMICAL PROPERTIES AND CELL PERFORMANCE

The cycle performance with discharge gravimetric specific capacities of poly(S-r-DIB) nanofiber cathode with and without the spin-coated RGO layer is shown in Figure 4-6a. Four different samples are tested including bulk poly(S-r-DIB) copolymer cathode without any modification of its surface morphology and pure sublimed sulfur cathode made with slurry solution of sulfur particles dissolved in the carbon disulfide. 10% of KB is added in all of the four samples to secure the electron pathways, and 5% of PEO has been used for an additional polymeric binder. All cells are operated at 0.2 C, normalized by the amount of sulfur. The electrolyte solution of 1 M Lithium bis(trifluoromethylsulphonyl)imide (LiTFSI) in 1,2-dimethoxyethane (DME) and 1,3-dioxolane (DOL) in the volume ratio of 1:1 with addition of 0.5 M $LiNO_3$.

The discharge specific capacities of the 1st cycles of poly(S-r-DIB) nanofiber cathodes with RGO layer, bulk-type poly(S-r-DIB) copolymer cathode with RGO layer, bulk-type poly(S-r-DIB) copolymer cathode without RGO layer, and finally pure sublime sulfur cathode with RGO

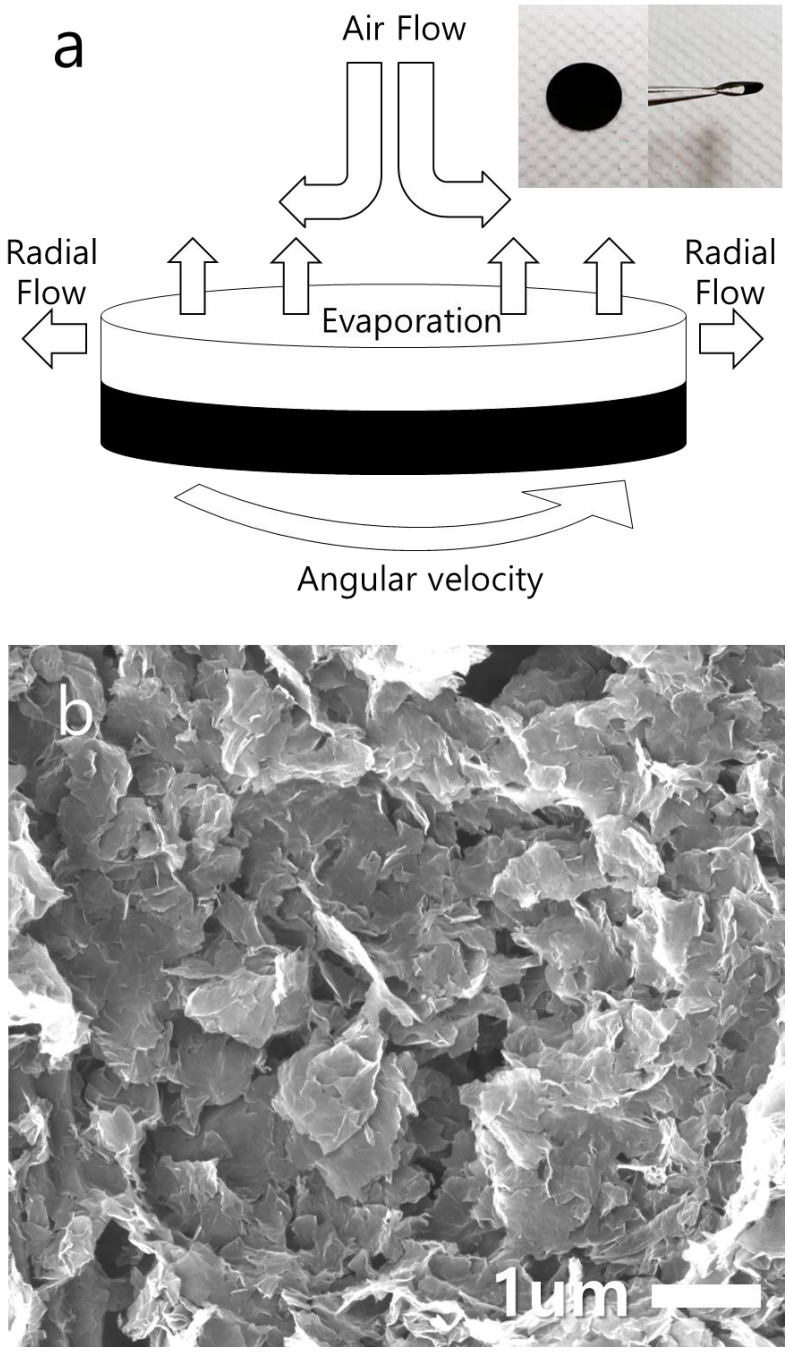

Figure 4-5. (a) Schematic of spin-coating RGO thin film on top of the poly(S-r-DIB) nanofiber: Inset is a digital image of a cathode and demonstration of its flexibility, (b) FE-SEM image of RGO film on top of poly(S-r-DIB) nanofiber

layer are 1549, 1391, 1382, and 1182 mAh/g, with respect to the amount of sulfur, respectively whereas at 100th cycle, they slowly fade down to 952, 768, 527, and 359 mAh/g, respectively, at0.2 C. The discharge-charge curves of the first cycle of poly(S-r-DIB) nanofiber cathodes with RGO layer are shown in Figure 4-6b within a voltage window of 1.6 ~ 2.8 V. The formation of nanofiber morphology helped improve the capacity retention over a number of cycles due to the alleviating effect of the volume expansion, not to mention the discharge specific capacity of the first cycle due to the enlarged specific surface area of the poly(S-r-DIB) copolymer. Although the thin film RGO layer was not as much effective as the fiber morphology of poly(S-r-DIB) copolymer in terms of the first discharge capacity, it sure has enhanced the capacity retention by almost 50% at the 100^{th} operating cycle, and proved in part that the spin coated RGO layer has successfully reduced the amount of intermediate polysulfide dissolution. The poly(S-r-DIB) copolymer cathode, regardless of its morphology or the addition of RGO layer, still excels in its cycle performance in comparison with the cathode made of pure sublimed sulfur powder mixed with KB. The total sulfur loading is ~2.5 mg/cm^2 and the sulfur copolymer content among the cathode materials is 75 wt% in all cases.

According to the well-recognized EIS model for the lithium-sulfur batteries, the high frequency intercept corresponds to the cell ohmic resistance, the middle frequency semicircle to the interfacial resistance, and the low frequency semi-circle to the charge transfer resistance of the cell. The Nyquist plots using AC impedance data in Figure 4-6c show only one semicircle for each cathode, which combines both interfacial and charge transfer resistance. From the plots it can be seen that the width of the semicircle of pure sublime sulfur cathode with RGO layer shows larger than that of the poly(S-r-DIB) nanofiber cathode with RGO layer, and poly(S-r-DIB)

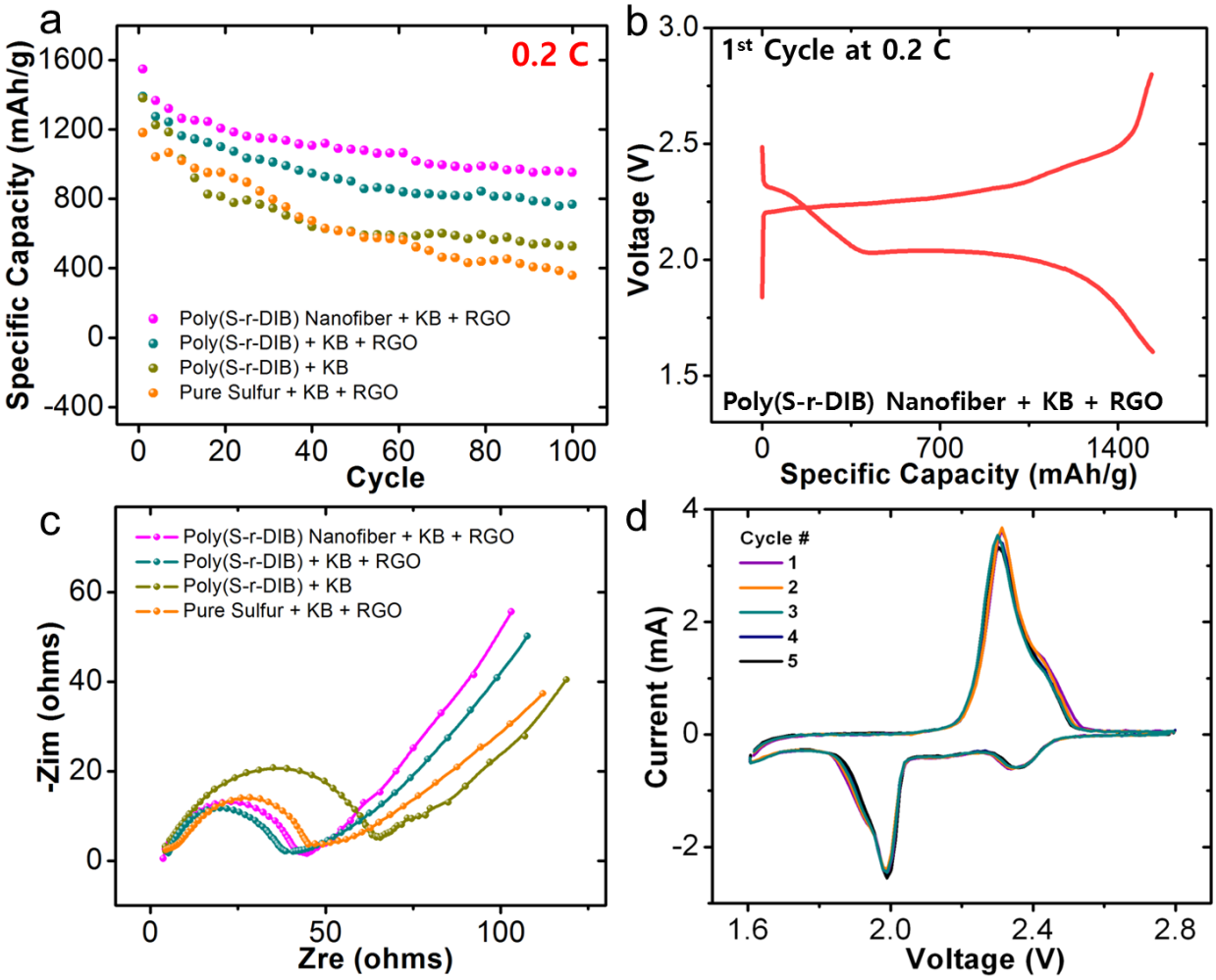

Figure 4-6. (a) Cycle performance with specific capacities of poly(S-r-DIB) cathode with and without RGO layer and cathode using pure sulfur as active material at 0.2 C. (b) Voltage limit profile of the first discharge and charge cycle of poly(S-r-DIB) nanofiber cathode with addition of KB and RGO layer. (c) EIS data of poly(S-r-DIB) cathode with and without RGO layer and cathode using pure sulfur (d) Cyclic voltammetry (CV) curves at the first 5 cycles conducted at a scan rate of 0.1 mV/s in the voltage range of 1.6 to 2.8 V versus Li/Li^{+}.

nanofiber cathode with RGO layer has the width of the semicircle slightly larger than the bulk-type poly(S-r-DIB) cathode with RGO layer, while the charge transfer resistance of the bulk-type poly(S-r-DIB) cathode without RGO layer is significantly larger than any of the others. Figure 4-6d shows the first five cycles of CV for the poly(S-r-DIB) nanofiber cathode with RGO layer with sulfur loading of 2.5 mg/cm^2 at a scan rate of 0.1 mV/s in the voltage range of 1.6 to 2.8 V versus Li/Li$^+$. During the cathodic scans, one large and one small reduction peaks at about 2.0 and 2.3 V appeared presenting a two-step reduction of lithiated sulfur. According to the reported mechanisms, the peak at 2.3 V is responsible for the reduction of elemental sulfur to higher order polysulfide ions (Li_2S_8, Li_2S_6, Li_2S_4), and the peak at 2.0 V corresponds to the reduction of high order polysulfide ions to lower order polysulfide ions (Li_2S_2, Li_2S). [66, 69, 122-125] In the case of anodic scans, one large oxidation peak was observed at 2.31 V which can be assigned to the transition of lithium sulfide (Li_2S) and polysulfide ions into elemental sulfur. Every peak from anodic and cathodic scans shows very little change over the first fiver cycles, indicating that the poly(S-r-DIB) copolymer nanofiber cathode with RGO layer possesses an excellent electrochemical reversibility.

In summary, the elongation and elasticity of the synthesized poly(S-r-DIB) copolymer allow it to be electrospun to produce poly(S-r-DIB) nanofiber with ~200 nm in diameter. The as-spun poly(S-r-DIB) nanofiber with the addition of KB and RGO layer onto the aluminum foil current collector can be directly used as lithium-sulfur battery cathode, which accommodates the volumetric expansion of lithiated sulfur and significantly reduces the polysulfide dissolution into the electrolyte and onto the lithium metal anode. Spin-coated RGO layer on top of the poly(S-r-DIB) nanofiber helps to further reduce the amount of polysulfide dissolution, and the cathode

performs ~ 900 mAh/g for over 100 cycles at 0.2 C with total sulfur loading of 2.5 mg/cm^2. CV curves of the poly(S-r-DIB) nanofiber cathode with large peaks show little change over the first five cycles, indicating that the cathode material and its structure have the superior reversibility in electrochemical reaction during discharge and charge cycle.

CHAPTER V.

SUMMARY AND FUTURE WORK

Lithium-air and lithium-sulfur batteries are the most promising candidates for next generation rechargeable batteries for their high theoretical energy density and low price of active materials. The importance of the structural stability of cathode for lithium-sulfur batteries has been emphasized for long and researchers proposed a number of solution to accommodate the volume expansion of the lithiated sulfur. The last part of this study on the lithium-sulfur battery cathode structure shows the improvement of the capacity retention by resolving the well-known issue of the volume expansion with the use of electrospun polymeric sulfur or poly(S-r-DIB) copolymer nanofiber. Meanwhile, the significance of the structural stability of the lithium-air battery cathode has not been pointed out elsewhere until now in this study with viable evidence of experiments. The first three parts of this study focus on the evidence of the structural disorder in the lithium-air battery cathode after discharge and charge cycles and methods to enhance the electrochemical performance by controlling the structural parameters of the cathodes. Thermal restacking of swollen cathode structure after cycles, sandwich stacking with two different types of carbon, and thermo-mechanically stabilized freestanding carbon nanofiber that combines what we have learned from the first two parts present facile and novel solution to avoid and alleviate the rapid loss of capacity over cycles and degradation of the cell. Overall, the comprehensive results in this study bring new insights and perspectives and stress the importance of the structural parameters of both lithium-air and lithium-sulfur battery cathodes.

Intensive and comprehensive research on the physical configuration of lithium-air and lithium-sulfur battery cathodes has been conducted and presented in this paper. As initially hypothesized, the structural parameters of cathodes have been found to be significant in terms of determining the electrochemical performance of the corresponding cells and we have witnessed how far it could achieve by controlling the cathode pore structure, and yet, it is still insufficient to call that they are ready to squeeze themselves into the market. On the course of delving deeper for each topic in this study, it has come to our knowledge that chemical modification of the cell components along with physical adjustment has been considered vital and discovered to hold massive potential for further enhancing the cycle performance. Exploring redox mediators or bifunctional catalysts to mitigate the parasitic reactions for lithium-air batteries or to minimize the polysulfide shuttle effect for lithium-sulfur batteries is one way of approaching to meet the industrial requirements. Our study in the future will switch gears from controlling the physical configuration and involve much more in the chemistry of materials including redox mediators, carbon surface functional groups, and noncorrosive electrolyte solution.

REFERENCES

[1]. P.G. Bruce, S. A. Freunberger, L.J. Hardwick, J.M. Tarascon, Li–O_2 and Li–S batteries with high energy storage, Nat. Mater. 11 (2011) 172–172. doi:10.1038/nmat3237.

[2]. G. Girishkumar, B. McCloskey, A. C. Luntz, S. Swanson, W. Wilcke, Lithium-air battery: Promise and challenges, J. Phys. Chem. Lett. 1 (2010) 2193–2203. doi:10.1021/jz1005384.

[3]. J.S. Lee, S.T. Kim, R. Cao, N.S. Choi, M. Liu, K.T. Lee, et al., Metal-air batteries with high energy density: Li-air versus Zn-air, Adv. Energy Mater. 1 (2011) 34–50. doi:10.1002/aenm.201000010.

[4]. K.G. Gallagher, S. Goebel, T. Greszler, M. Mathias, W. Oelerich, D. Eroglu, et al., Quantifying the promise of lithium–air batteries for electric vehicles, Energy Environ. Sci. 7 (2014) 1555. doi:10.1039/c3ee43870h.

[5]. Y.C. Lu, B.M. Gallant, D.G. Kwabi, J.R. Harding, R.R. Mitchell, M.S. Whittingham, et al., Lithium-oxygen batteries: bridging mechanistic understanding and battery performance, Energy Environ. Sci. 6 (2013) 750–768. doi:Doi 10.1039/C3ee23966g.

[6]. Y.C. Lu, Z. Xu, H.A. Gasteiger, S. Chen, K. Hamad-Schifferli, Y. Shao-Horn, Platinum-gold nanoparticles: A highly active bifunctional electrocatalyst for rechargeable lithium-air batteries, J. Am. Chem. Soc. 132 (2010) 12170–12171. doi:10.1021/ja1036572.

[7]. T. Zhang, H. Zhou, A reversible long-life lithium-air battery in ambient air., Nat. Commun. 4 (2013) 1817. doi:10.1038/ncomms2855.

[8]. S.D. Beattie, D.M. Manolescu, S.L. Blair, High-Capacity Lithium–Air Cathodes, J. Electrochem. Soc. 156 (2009) A44–A47. doi:10.1149/1.3005989.

[9]. T. Liu, M. Leskes, W. Yu, A.J. Moore, L. Zhou, P.M. Bayley, et al., Cycling Li-O_2 batteries via LiOH formation and decomposition, Science. 350 (2015) 530–533. doi:10.1126/science.aac7730.

[10]. J. Xiao, D. Wang, W. Xu, D. Wang, R.E. Williford, J. Liu, et al., Optimization of Air Electrode for Li/Air Batteries, J. Electrochem. Soc. 157 (2010) A487. doi:10.1149/1.3314375.

[11]. W. Walker, V. Giordani, J. Uddin, V.S. Bryantsev, G. V Chase, D. Addison, A Rechargeable Li-O-2 Battery Using a Lithium Nitrate/N,N-Dimethylacetamide Electrolyte, J. Am. Chem. Soc. 135 (2013) 2076–2079. doi:10.1021/ja311518s.

[12]. J. Xiao, D. Mei, X. Li, W. Xu, D. Wang, G.L. Graff, et al., Hierarchically porous graphene as a lithium-air battery electrode, Nano Lett. 11 (2011) 5071–5078. doi:10.1021/nl203332e.

[13]. C. Tran, X.Q. Yang, D. Qu, Investigation of the gas-diffusion-electrode used as lithium/air cathode in non-aqueous electrolyte and the importance of carbon material porosity, J. Power Sources. 195 (2010) 2057–2063. doi:10.1016/j.jpowsour.2009.10.012.

[14]. S.S. Sandhu, J.P. Fellner, G.W. Brutchen, Diffusion-limited model for a lithium/air battery with an organic electrolyte, J. Power Sources. 164 (2007) 365–371. doi:10.1016/j.jpowsour.2006.09.099.

[15]. M.J. Lacey, J.T. Frith, J.R. Owen, A redox shuttle to facilitate oxygen reduction in the lithium air battery, Electrochem. Commun. 26 (2013) 74–76. doi:10.1016/j.elecom.2012.10.009.

[16]. T. Zhang, N. Imanishi, Y. Shimonishi, A. Hirano, Y. Takeda, O. Yamamoto, et al., A novel high energy density rechargeable lithium/air battery., Chem. Commun. 46 (2010) 1661–3. doi:10.1039/b920012f.

[17]. R. Padbury, X. Zhang, Lithium–oxygen batteries—Limiting factors that affect performance, J. Power Sources. 196 (2011) 4436–4444. doi:10.1016/j.jpowsour.2011.01.032.

[18]. Y. Shen, D. Sun, L. Yu, W. Zhang, Y. Shang, H. Tang, et al., A high-capacity lithium-air battery with Pd modified carbon nanotube sponge cathode working in regular air, Carbon N. Y. 62 (2013) 288–295. doi:10.1016/j.carbon.2013.05.066.

[19]. J. Nanda, H. Bilheux, S. Voisin, G.M. Veith, R. Archibald, L. Walker, et al., Anomalous discharge product distribution in lithium-air cathodes, J. Phys. Chem. C. 116 (2012) 8401–8408. doi:10.1021/jp3016003.

[20]. N. Garcia-Araez, P. Novák, Critical aspects in the development of lithium-air batteries, J. Solid State Electrochem. 17 (2013) 1793–1807. doi:10.1007/s10008-013-1999-1.

[21]. S.P. Ong, Y. Mo, G. Ceder, Low hole polaron migration barrier in lithium peroxide, Phys. Rev. B - Condens. Matter Mater. Phys. 85 (2012). doi:10.1103/PhysRevB.85.081105.

[22]. Aetukuri, N. B. et al. Solvating additives drive solution-mediated electrochemistry and enhance toroid growth in non-aqueous Li–O2 batteries. Nat. Chem. 7, 50-56 (2015)

[23]. Peng, Z., Freunberger, S. A., Chen, Y., Bruce, P. G. A reversible and higher-rate Li-O_2 battery. Science 337, 563-566 (2012).

[24]. Lu, J. et al. A nanostructured cathode architecture for low charge overpotential in lithium-oxygen batteries. Nat. Commun. 4, 2383 (2013).

[25]. Jung, H. G. et al. An improved high-performance lithium–air battery. Nat. Chem. 4, 579–585 (2012).

[26]. Chen, Y. et al. Charging a Li–O_2 battery using a redox mediator. Nat. Chem. 5, 489–494 (2013).

[27]. B.D. McCloskey, R. Scheffler, A. Speidel, G. Girishkumar, A.C. Luntz, On the mechanism of nonaqueous Li-O_2 electrochemistry on C and its kinetic overpotentials: Some implications for Li-air batteries, J. Phys. Chem. C. 116 (2012) 23897–23905. doi:10.1021/jp306680f.

[28]. D. Kundu, R. Black, E.J. Berg, L.F. Nazar, A highly active nanostructured metallic oxide cathode for aprotic Li–O_2 batteries, Energy Environ. Sci. 8 (2015) 1292–1298. doi:10.1039/C4EE02587C.

[29]. N. Imanishi, S. Hasegawa, T. Zhang, A. Hirano, Y. Takeda, O. Yamamoto, Lithium anode for lithium-air secondary batteries, J. Power Sources. 185 (2008) 1392–1397. doi:10.1016/j.jpowsour.2008.07.080.

[30]. J. Hassoun, H.G. Jung, D.J. Lee, J.B. Park, K. Amine, Y.K. Sun, et al., A metal-free, lithium-ion oxygen battery: A step forward to safety in lithium-air batteries, Nano Lett. 12 (2012) 5775–5779. doi:10.1021/nl303087j.

[31]. W. Xu, J. Wang, F. Ding, X. Chen, E. Nasybulin, Y. Zhang, et al., Lithium metal anodes for rechargeable batteries, Energy Environ. Sci. 7 (2014) 513–537. doi:10.1039/C3EE40795K.

[32]. G. Bieker, M. Winter, P. Bieker, Electrochemical in situ investigations of SEI and dendrite formation on the lithium metal anode., Phys. Chem. Chem. Phys. 17 (2015) 8670–9. doi:10.1039/c4cp05865h.

[33]. F. Ding, W. Xu, G.L. Graff, J. Zhang, M.L. Sushko, X. Chen, et al., Dendrite-free lithium deposition via self-healing electrostatic shield mechanism, J. Am. Chem. Soc. 135 (2013) 4450–4456. doi:10.1021/ja312241y.

[34]. M.S. Park, S.B. Ma, D.J. Lee, D. Im, S.-G. Doo, O. Yamamoto, A highly reversible lithium metal anode., Sci. Rep. 4 (2014) 3815. doi:10.1038/srep03815.

[35]. Shui, J. L., Wang, H. H., Liu, D. J. Degradation and revival of Li–O_2 battery cathode. Electrochem. Commun. 34, 45-47 (2013).

[36]. B.D. McCloskey, D.S. Bethune, R.M. Shelby, G. Girishkumar, A.C. Luntz, Solvents critical role in nonaqueous Lithium-Oxygen battery electrochemistry, J. Phys. Chem. Lett. 2 (2011) 1161–1166. doi:10.1021/jz200352v.

[37]. C.O. Laoire, S. Mukerjee, K.M. Abraham, E.J. Plichta, M.A. Hendrickson, Influence of nonaqueous solvents on the electrochemistry of oxygen in the rechargeable lithium-air battery, J. Phys. Chem. C. 114 (2010) 9178–9186. doi:10.1021/jp102019y.

[38]. Y. Chen, S.A. Freunberger, Z. Peng, F. Bardé, P.G. Bruce, Li-O 2 battery with a dimethylformamide electrolyte, J. Am. Chem. Soc. 134 (2012) 7952–7957. doi:10.1021/ja302178w.

[39]. G.Q. Zhang, J.P. Zheng, R. Liang, C. Zhang, B. Wang, M. Au, et al., α-MnO2/Carbon Nanotube/Carbon Nanofiber Composite Catalytic Air Electrodes for Rechargeable Lithium-air Batteries, J. Electrochem. Soc. 158 (2011) A822. doi:10.1149/1.3590736.

[40]. Y. Li, J. Wang, X. Li, J. Liu, D. Geng, J. Yang, et al., Nitrogen-doped carbon nanotubes as cathode for lithium-air batteries, Electrochem. Commun. 13 (2011) 668–672. doi:10.1016/j.elecom.2011.04.004.

[41]. T.H. Yoon, Y.J. Park, Carbon nanotube/Co3O4 composite for air electrode of lithium-air battery., Nanoscale Res. Lett. 7 (2012) 28. doi:10.1186/1556-276X-7-28.

[42]. L. Wang, X. Zhao, Y. Lu, M. Xu, D. Zhang, R.S. Ruoff, et al., CoMn2O4 Spinel Nanoparticles Grown on Graphene as Bifunctional Catalyst for Lithium-Air Batteries, J. Electrochem. Soc. 158 (2011) A1379. doi:10.1149/2.068112jes.

[43]. B. Sun, B. Wang, D. Su, L. Xiao, H. Ahn, G. Wang, Graphene nanosheets as cathode catalysts for lithium-air batteries with an enhanced electrochemical performance, Carbon N. Y. 50 (2012) 727–733. doi:10.1016/j.carbon.2011.09.040.

[44]. H.G. Jung, Y.S. Jeong, J.B. Park, Y.K. Sun, B. Scrosati, Y.J. Lee, Ruthenium-based electrocatalysts supported on reduced graphene oxide for lithium-air batteries, ACS Nano. 7 (2013) 3532–3539. doi:10.1021/nn400477d.

[45]. J. Yin, J.M. Carlin, J. Kim, Z. Li, J.H. Park, B. Patel, et al., Synergy between metal oxide nanofibers and graphene nanoribbons for rechargeable lithium-oxygen battery cathodes, Adv. Energy Mater. 5 (2015). doi:10.1002/aenm.201401412.

[46]. J. Li, B. Peng, G. Zhou, Z. Zhang, Y. Lai, M. Jia, Partially Cracked Carbon Nanotubes as Cathode Materials for Lithium-Air Batteries, ECS Electrochem. Lett. 2 (2012) A25–A27. doi:10.1149/2.009302eel.

[47]. Y. Gong, H. Fei, X. Zou, W. Zhou, S. Yang, G. Ye, et al., Boron- and nitrogen-substituted graphene nanoribbons as efficient catalysts for oxygen reduction reaction, Chem. Mater. 27 (2015) 1181–1186. doi:10.1021/cm5037502.

[48]. P. Kichambare, J. Kumar, S. Rodrigues, B. Kumar, Electrochemical performance of highly mesoporous nitrogen doped carbon cathode in lithium-oxygen batteries, J. Power Sources. 196 (2011) 3310–3316. doi:10.1016/j.jpowsour.2010.11.112.

[49]. V. Etacheri, D. Sharon, A. Garsuch, M. Afri, A.A. Frimer, D. Aurbach, Hierarchical activated carbon microfiber (ACM) electrodes for rechargeable Li–O2 batteries, J. Mater. Chem. A. 1 (2013) 5021. doi:10.1039/c3ta01659e.

[50]. D. Zhai, K.C. Lau, H.H. Wang, J. Wen, D.J. Miller, F. Kang, et al., The Effect of Potassium Impurities Deliberately Introduced into Activated Carbon Cathodes on the Performance of Lithium-Oxygen Batteries, ChemSusChem. 8 (2015) 4235–4241. doi:10.1002/cssc.201500960.

[51]. M.J. Song, I.T. Kim, Y.B. Kim, M.W. Shin, Self-standing, binder-free electrospun Co_3O_4/carbon nanofiber composites for non-aqueous Li-air batteries, Electrochim. Acta. 182 (2015) 289–296. doi:10.1016/j.electacta.2015.09.100.

[52]. D.S. Kim, Y.J. Park, Buckypaper electrode containing carbon nanofiber/Co3O4 composite for enhanced lithium air batteries, Solid State Ionics. 268 (2014) 216–221. doi:10.1016/j.ssi.2014.03.010.

[53]. B.W. Huang, X.Z. Liao, H. Wang, C.N. Wang, Y.S. He, Z.F. Ma, Nanofibrous MnNi/CNF Composite Catalyst for Rechargeable Li/O2 Cell, J. Electrochem. Soc. 160 (2013) A1112–A1117. doi:10.1149/2.049308jes.

[54]. B.W. Huang, L. Li, Y.J. He, X.Z. Liao, Y.S. He, W. Zhang, et al., Enhanced electrochemical performance of nanofibrous CoO/CNF cathode catalyst for Li-O2 batteries, Electrochim. Acta. 137 (2014) 183–189. doi:10.1016/j.electacta.2014.05.114.

[55]. M. Chen, X. Jiang, H. Yang, P.K. Shen, Performance improvement of air electrode for Li/air batteries by hydrophobicity adjustment, J. Mater. Chem. A. 3 (2015) 11874–11879. doi:10.1039/C5TA01601K.

[56]. J. Xiao, D. Wang, W. Xu, D. Wang, R.E. Williford, J. Liu, et al., Optimization of Air Electrode for Li/Air Batteries, J. Electrochem. Soc. 157 (2010) A487. doi:10.1149/1.3314375.

[57]. S. Meini, S. Solchenbach, M. Piana, H. a Gasteiger, The Role of Electrolyte Solvent Stability and Electrolyte Impurities in the Electrooxidation of Li_2O_2 in Li-O_2 Batteries, J. Electrochem. Soc. 161 (2014) A1306–A1314. doi:10.1149/2.0621409jes.

[58]. Y. Zhang, H. Zhang, J. Li, M. Wang, H. Nie, F. Zhang, The use of mixed carbon materials with improved oxygen transport in a lithium-air battery, J. Power Sources. 240 (2013) 390–396. doi:10.1016/j.jpowsour.2013.04.018.

[59]. A. Manthiram, Y. Fu, Y.S. Su, Challenges and Prospects of Lithium–Sulfur Batteries, Acc. Chem. Res. 46 (2013) 1125–1134. doi:10.1021/ar300179v.

[60]. S. Evers, L.F. Nazar, New approaches for high energy density lithium-sulfur battery cathodes, Acc. Chem. Res. 46 (2013) 1135–1143. doi:10.1021/ar3001348.

[61]. A. Manthiram, Y. Fu, S.H. Chung, C. Zu, Y.S. Su, Rechargeable lithium-sulfur batteries, Chem. Rev. 114 (2014) 11751–11787. doi:10.1021/cr500062v.

[62]. Y.X. Yin, S. Xin, Y.G. Guo, L.J. Wan, Lithium-sulfur batteries: Electrochemistry, materials, and prospects, Angew. Chemie - Int. Ed. 52 (2013) 13186–13200. doi:10.1002/anie.201304762.

[63]. C. Barchasz, F. Molton, C. Duboc, J.C. Leprêtre, S. Patoux, F. Alloin, Lithium/sulfur cell discharge mechanism: An original approach for intermediate species identification, Anal. Chem. 84 (2012) 3973–3980. doi:10.1021/ac2032244.

[64]. J. Gao, M.A. Lowe, Y. Kiya, H.D. Abruña, Effects of liquid electrolytes on the charge-discharge performance of rechargeable lithium/sulfur batteries: Electrochemical and in-situ X-ray absorption spectroscopic studies, J. Phys. Chem. C. 115 (2011) 25132–25137. doi:10.1021/jp207714c.

[65]. S.E. Cheon, K.S. Ko, J.H. Cho, S.W. Kim, E.Y. Chin, H.T. Kim, Rechargeable Lithium Sulfur Battery, J. Electrochem. Soc. 150 (2003) A800. doi:10.1149/1.1571533.

[66]. N. Jayaprakash, J. Shen, S.S. Moganty, A. Corona, L.A. Archer, Porous hollow carbon@sulfur composites for high-power lithium-sulfur batteries, Angew. Chemie - Int. Ed. 50 (2011) 5904–5908. doi:10.1002/anie.201100637.

[67]. G.C. Li, G.R. Li, S.H. Ye, X.P. Gao, A Polyaniline-coated sulfur/carbon composite with an enhanced high-rate capability as a cathode material for lithium/sulfur batteries, Adv. Energy Mater. 2 (2012) 1238–1245. doi:10.1002/aenm.201200017.

[68]. S. Dörfler, M. Hagen, H. Althues, J. Tübke, S. Kaskel, M.J. Hoffmann, High capacity vertical aligned carbon nanotube/sulfur composite cathodes for lithium–sulfur batteries, Chem. Commun. 48 (2012) 4097. doi:10.1039/c2cc17925c.

[69]. L. Ji, M. Rao, H. Zheng, L. Zhang, Y. Li, W. Duan, et al., Graphene oxide as a sulfur immobilizer in high performance lithium/sulfur cells, J. Am. Chem. Soc. 133 (2011) 18522–18525. doi:10.1021/ja206955k.

[70]. Y. Yang, G. Yu, J.J. Cha, H. Wu, M. Vosgueritchian, Y. Yao, et al., Improving the performance of lithium-sulfur batteries by conductive polymer coating, ACS Nano. 5 (2011) 9187–9193. doi:10.1021/nn203436j.

[71]. J.Q. Huang, Q. Zhang, H.J. Peng, X.Y. Liu, W.Z. Qian, F. Wei, Ionic shield for polysulfides towards highly-stable lithium–sulfur batteries, Energy Environ. Sci. 7 (2014) 347. doi:10.1039/c3ee42223b.

[72]. G. Zheng, Q. Zhang, J.J. Cha, Y. Yang, W. Li, Z.W. Seh, et al., Amphiphilic surface modification of hollow carbon nanofibers for improved cycle life of lithium sulfur batteries, Nano Lett. 13 (2013) 1265–1270. doi:10.1021/nl304795g.

[73]. X. Liang, C. Hart, Q. Pang, A. Garsuch, T. Weiss, L.F. Nazar, A highly efficient polysulfide mediator for lithium–sulfur batteries, Nat. Commun. 6 (2015) 5682. doi:10.1038/ncomms6682.

[74]. J. Song, M.L. Gordin, T. Xu, S. Chen, Z. Yu, H. Sohn, et al., Strong lithium polysulfide chemisorption on electroactive sites of nitrogen-doped carbon composites for high-performance lithium-sulfur battery cathodes, Angew. Chemie - Int. Ed. 54 (2015) 4325–4329. doi:10.1002/anie.201411109.

[75]. E.S. Shin, K. Kim, S.H. Oh, W. Il Cho, Polysulfide dissolution control: the common ion effect., Chem. Commun. (Camb). 49 (2013) 2004–6. doi:10.1039/c2cc36986a.

[76]. X. Wang, Z. Wang, L. Chen, Reduced graphene oxide film as a shuttle-inhibiting interlayer in a lithium-sulfur battery, J. Power Sources. 242 (2013) 65–69. doi:10.1016/j.jpowsour.2013.05.063 Short communication.

[77]. I. Bauer, S. Thieme, J. Brückner, H. Althues, S. Kaskel, Reduced polysulfide shuttle in lithium-sulfur batteries using Nafion-based separators, J. Power Sources. 251 (2014) 417–422. doi:10.1016/j.jpowsour.2013.11.090.

[78]. S. Xiong, K. Xie, Y. Diao, X. Hong, Characterization of the solid electrolyte interphase on lithium anode for preventing the shuttle mechanism in lithium-sulfur batteries, J. Power Sources. 246 (2014) 840–845. doi:10.1016/j.jpowsour.2013.08.041.

[79]. X.B. Cheng, J.Q. Huang, H.J. Peng, J.Q. Nie, X.Y. Liu, Q. Zhang, et al., Polysulfide shuttle control: Towards a lithium-sulfur battery with superior capacity performance up to 1000 cycles by matching the sulfur/electrolyte loading, J. Power Sources. 253 (2014) 263–268. doi:10.1016/j.jpowsour.2013.12.031.

[80]. H. Wang, Y. Yang, Y. Liang, J.T. Robinson, Y. Li, A. Jackson, et al., Graphene-wrapped sulfur particles as a rechargeable lithium-sulfur battery cathode material with

high capacity and cycling stability, Nano Lett. 11 (2011) 2644–2647. doi:10.1021/nl200658a.

[81]. X. Ji, K.T. Lee, L.F. Nazar, A highly ordered nanostructured carbon-sulphur cathode for lithium-sulphur batteries., Nat. Mater. 8 (2009) 500–506. doi:10.1038/nmat2460.

[82]. Z. Wei Seh, W. Li, J.J. Cha, G. Zheng, Y. Yang, M.T. McDowell, et al., Sulphur-TiO2 yolk-shell nanoarchitecture with internal void space for long-cycle lithium-sulphur batteries., Nat. Commun. 4 (2013) 1331. doi:10.1038/ncomms2327.

[83]. F. Li, G. Zhou, S. Pei, L. Li, D.W. Wang, S. Wang, et al., A graphene-pure-sulfur sandwich structure for ultrafast, long-life lithium-sulfur batteries, Adv. Mater. 26 (2014) 625–631. doi:10.1002/adma.201302877.

[84]. C. Zhang, H. Bin Wu, C. Yuan, Z. Guo, X.W. Lou, Confining sulfur in double-shelled hollow carbon spheres for lithium-sulfur batteries, Angew. Chemie - Int. Ed. 51 (2012) 9592–9595. doi:10.1002/anie.201205292.

[85]. W. Zhou, Y. Yu, H. Chen, F.J. Disalvo, H.D. Abruña, Yolk-shell structure of polyaniline-coated sulfur for lithium-sulfur batteries, J. Am. Chem. Soc. 135 (2013) 16736–16743. doi:10.1021/ja409508q.

[86]. D. Li, F. Han, S. Wang, F. Cheng, Q. Sun, W.C. Li, High sulfur loading cathodes fabricated using peapodlike, large pore volume mesoporous carbon for lithium-sulfur battery, ACS Appl. Mater. Interfaces. 5 (2013) 2208–2213. doi:10.1021/am4000535.

[87]. S. Chen, X. Huang, H. Liu, B. Sun, W. Yeoh, K. Li, et al., 3D hyperbranched hollow carbon nanorod architectures for high-performance lithium-sulfur batteries, Adv. Energy Mater. 4 (2014). doi:10.1002/aenm.201301761.

[88]. C. Wang, K. Su, W. Wan, H. Guo, H. Zhou, J. Chen, et al., High sulfur loading composite wrapped by 3D nitrogen-doped graphene as a cathode material for lithium-sulfur batteries, J. Mater. Chem. A. 2 (2014) 5018–5023. doi:10.1039/C3TA14921H.

[89]. G. Ma, Z. Wen, M. Wu, C. Shen, Q. Wang, J. Jin, et al., A lithium anode protection guided highly-stable lithium–sulfur battery, Chem. Commun. 50 (2014) 14209–14212. doi:10.1039/C4CC05535G.

[90]. F. Wu, J.T. Lee, N. Nitta, H. Kim, O. Borodin, G. Yushin, Lithium iodide as a promising electrolyte additive for lithium-sulfur batteries: Mechanisms of performance enhancement, Adv. Mater. 27 (2015) 101–108. doi:10.1002/adma.201404194.

[91]. W. Li, H. Yao, K. Yan, G. Zheng, Z. Liang, Y.-M. Chiang, et al., The synergetic effect of lithium polysulfide and lithium nitrate to prevent lithium dendrite growth., Nat. Commun. 6 (2015) 7436. doi:10.1038/ncomms8436.

[92]. Z. Lin, Z. Liu, W. Fu, N.J. Dudney, C. Liang, Phosphorous pentasulfide as a novel additive for high-performance lithium-sulfur batteries, Adv. Funct. Mater. 23 (2013) 1064–1069. doi:10.1002/adfm.201200696.

[93]. J. Hassoun, B. Scrosati, Moving to a solid-state configuration: A valid approach to making lithium-sulfur batteries viable for practical applications, Adv. Mater. 22 (2010) 5198–5201. doi:10.1002/adma.201002584.

[94]. S. Xin, L. Gu, N.H. Zhao, Y.X. Yin, L.J. Zhou, Y.G. Guo, et al., Smaller sulfur molecules promise better lithium'sulfur batteries, J. Am. Chem. Soc. 134 (2012) 18510–18513. doi:10.1021/ja308170k.

[95]. W.J. Chung, J.J. Griebel, E.T. Kim, H. Yoon, A.G. Simmonds, H.J. Ji, et al., The use of elemental sulfur as an alternative feedstock for polymeric materials, Nat. Chem. 5 (2013) 518–524. doi:10.1038/nchem.1624.

[96]. D.M. Itkis, D.A. Semenenko, E.Y. Kataev, A.I. Belova, V.S. Neudachina, A.P. Sirotina, et al., Reactivity of carbon in lithium-oxygen battery positive electrodes, Nano Lett. 13 (2013) 4697–4701. doi:10.1021/nl4021649.

[97]. R. Wen, H.R. Byon, In situ monitoring of the Li-O2 electrochemical reaction on nanoporous gold using electrochemical AFM., Chem. Commun. 50 (2014) 2628–31. doi:10.1039/c3cc49625b.

[98]. B.D. McCloskey, D.S. Bethune, R.M. Shelby, G. Girishkumar, A.C. Luntz, Solvents critical role in nonaqueous Lithium-Oxygen battery electrochemistry, J. Phys. Chem. Lett. 2 (2011) 1161–1166. doi:10.1021/jz200352v.

[99]. B.D. McCloskey, A. Speidel, R. Scheffler, D.C. Miller, V. Viswanathan, J.S. Hummelshøj, et al., Twin Problems of Interfacial Carbonate Formation in Nonaqueous Li-O2 Batteries., J. Phys. Chem. Lett. 3 (2012) 997–1001. doi:10.1021/jz300243r.

[100]. Y.C. Lu, H.A. Gasteiger, Y. Shao-Horn, Catalytic activity trends of oxygen reduction reaction for nonaqueous Li-air batteries, J. Am. Chem. Soc. 133 (2011) 19048–19051. doi:10.1021/ja208608s.

[101]. Sing, K. S. W. Reporting physisorption data for gas/solid systems with special reference to the determination of surface area and porosity. Pure Appl. Chem. 57 (4), 603–619 (2009).

[102]. C. Xia, C.L. Bender, B. Bergner, K. Peppler, J. Janek, An electrolyte partially-wetted cathode improving oxygen diffusion in cathodes of non-aqueous Li-air batteries, Electrochem. Commun. 26 (2013) 93–96. doi:10.1016/j.elecom.2012.10.020.

[103]. G.Q. Zhang, J.P. Zheng, R. Liang, C. Zhang, B. Wang, M. Hendrickson, et al., Lithium–Air Batteries Using SWNT/CNF Buckypapers as Air Electrodes, J. Electrochem. Soc. 157 (2010) A953. doi:10.1149/1.3446852.

[104]. B. Kumar, J. Kumar, R. Leese, J.P. Fellner, S.J. Rodrigues, K.M. Abraham, A Solid-State, Rechargeable, Long Cycle Life Lithium–Air Battery, J. Electrochem. Soc. 157 (2010) A50. doi:10.1149/1.3256129.

[105]. D. V Kosynkin, A.L. Higginbotham, A. Sinitskii, J.R. Lomeda, A. Dimiev, B.K. Price, et al., Longitudinal unzipping of carbon nanotubes to form graphene nanoribbons., Nature. 458 (2009) 872–876. doi:10.1038/nature07872.

[106]. E. Yoo, H. Zhou, Li-air rechargeable battery based on metal-free graphene nanosheet catalysts, ACS Nano. 5 (2011) 3020–3026. doi:10.1021/nn200084u.

[107]. W. Xu, J. Xiao, D. Wang, J. Zhang, J.G. Zhang, Effects of Nonaqueous Electrolytes on the Performance of Lithium/Air Batteries, J. Electrochem. Soc. 157 (2010) A219. doi:10.1149/1.3269928.

[108]. W. Xu, J. Xiao, J. Zhang, D. Wang, J.G. Zhang, Optimization of Nonaqueous Electrolytes for Primary Lithium/Air Batteries Operated in Ambient Environment, J. Electrochem. Soc. 156 (2009) A773. doi:10.1149/1.3168564.

[109]. Y. Cui, Z. Wen, X. Liang, Y. Lu, J. Jin, M. Wu, et al., A tubular polypyrrole based air electrode with improved O_2 diffusivity for Li–O_2 batteries, Energy Environ. Sci. 5 (2012) 7893. doi:10.1039/c2ee21638h.

[110]. J.J. Xu, Z.L. Wang, D. Xu, L.L. Zhang, X.B. Zhang, Tailoring deposition and morphology of discharge products towards high-rate and long-life lithium-oxygen batteries., Nat. Commun. 4 (2013) 2438. doi:10.1038/ncomms3438.

[111]. S. Chen, H. Hou, F. Harnisch, S. A. Patil, A. a. Carmona-Martinez, S. Agarwal, et al., Electrospun and solution blown three-dimensional carbon fiber nonwovens for application as electrodes in microbial fuel cells, Energy Environ. Sci. 4 (2011) 1417. doi:10.1039/c0ee00446d.

[112]. K. Garg, G.L. Bowlin, Electrospinning jets and nanofibrous structures, Biomicrofluidics. 5 (2011). doi:10.1063/1.3567097.

[113]. M. Pakravan, M.C. Heuzey, A. Ajji, A fundamental study of chitosan/PEO electrospinning, Polymer. 52 (2011) 4813–4824. doi:10.1016/j.polymer.2011.08.034.

[114]. F. Liu, H. Wang, L. Xue, L. Fan, Z. Zhu, Effect of microstructure on the mechanical properties of PAN-based carbon fibers during high-temperature graphitization, J. Mater. Sci. 43 (2008) 4316–4322. doi:10.1007/s10853-008-2633-y..

[115]. D. Li, H. Wang, X. Wang, Effect of microstructure on the modulus of PAN-based carbon fibers during high temperature treatment and hot stretching graphitization, J. Mater. Sci. 42 (2007) 4642–4649. doi:10.1007/s10853-006-0519-4.

[116]. H. Oda, A. Yamashita, S. Minoura, M. Okamoto, T. Morimoto, Modification of the oxygen-containing functional group on activated carbon fiber in electrodes of an electric double-layer capacitor, J. Power Sources. 158 (2006) 1510–1516. doi:10.1016/j.jpowsour.2005.10.061.

[117]. S. Kundu, Y. Wang, W. Xia, M. Muhler, Thermal stability and reducibility of oxygen-containing functional groups on multi-walled carbon nanotube surfaces: A quantitative high-

resolution XPS and TPD/TPR study, J. Phys. Chem. C. 112 (2008) 16869–16878. doi:10.1021/jp804413a.

[118]. K. Gong, F. Du, Z. Xia, M. Durstock, L. Dai, Nitrogen-Doped Carbon Nanotube Arrays with High Electrocatalytic Activity for Oxygen Reduction, Science. 323 (2009) 760–764. doi:10.1126/science.1168049.

[119]. Y. Shao, J. Sui, G. Yin, Y. Gao, Nitrogen-doped carbon nanostructures and their composites as catalytic materials for proton exchange membrane fuel cell, Appl. Catal. B Environ. 79 (2008) 89–99. doi:10.1016/j.apcatb.2007.09.047.

[120]. Y. Tang, B.L. Allen, D.R. Kauffman, A. Star, Electrocatalytic activity of nitrogen-doped carbon nanotube cups, J. Am. Chem. Soc. 131 (2009) 13200–13201. doi:10.1021/ja904595t.

[121]. S. Chen, J. Bi, Y. Zhao, L. Yang, C. Zhang, Y. Ma, et al., Nitrogen-doped carbon nanocages as efficient metal-free electrocatalysts for oxygen reduction reaction, Adv. Mater. 24 (2012) 5593–5597. doi:10.1002/adma.201202424.

[122]. S.S. Jeong, Y.T. Lim, Y.J. Choi, G.B. Cho, K.W. Kim, H.J. Ahn, et al., Electrochemical properties of lithium sulfur cells using PEO polymer electrolytes prepared under three different mixing conditions, J. Power Sources. 174 (2007) 745–750. doi:10.1016/j.jpowsour.2007.06.108.

[123]. B. Jin, J.U. Kim, H.B. Gu, Electrochemical properties of lithium-sulfur batteries, J. Power Sources. 117 (2003) 148–152. doi:10.1016/S0378-7753(03)00113-7.

[124]. B.H. Jeon, J.H. Yeon, K.M. Kim, I.J. Chung, Preparation and electrochemical properties of lithium-sulfur polymer batteries, J. Power Sources. 109 (2002) 89–97. doi:10.1016/S0378-7753(02)00050-2.

[125]. Y.J. Choi, Y.D. Chung, C.Y. Baek, K.W. Kim, H.J. Ahn, J.H. Ahn, Effects of carbon coating on the electrochemical properties of sulfur cathode for lithium/sulfur cell, in: J. Power Sources, 2008: pp. 548–552. doi:10.1016/j.jpowsour.2008.02.053.